Durham E-Theses

Optimizing a Rydberg Atom-based Terahertz Imaging System

JAMIESON, MATTHEW,JAMES

Optimizing a Rydberg Atom-based Terahertz Imaging System

Matt Jamieson

A thesis presented for the degree of

Doctor of Philosophy
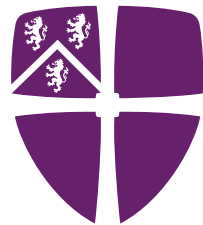
Quantum Light & Matter

The University of Durham

United Kingdom

30 April 2023

Optimizing a Rydberg Atom-based Terahertz Imaging System

Matt Jamieson

Abstract

We build upon previous work by characterising and optimizing the signal from a Rydberg atom-based terahertz (THz) imaging system, where atoms are excited to a Rydberg state by a three step ladder scheme. These Rydberg atoms provide a THz imaging mechanism via a fluorescence signal, F_{sig}. We implement a Pound-Drever-Hall lock and a digital scanning transfer cavity lock on the Rydberg laser. Both schemes see an improvement in the stability of fluorescence signal over time, to within 3%. We characterise the effect of laser parameters on F_{sig}. A pumping scheme consisting of alternating circular polarisations for each step are found to maximise F_{sig}, providing a $\sim 38\%$ increase compared to the all-linear configuration. The dependence of F_{sig} on Rydberg laser detuning and THz detuning is also characterised, and splitting due to the AC Stark shift is observed at higher THz powers. Simultaneous resonant excitation of the Rydberg and THz transition is found to maximize F_{sig}. A repump laser is implemented on both the D1 and D2 lines, and found to increase F_{sig} most on the D1 line, by a factor of seven. The effect on F_{sig} of the repump lasers power and detuning is characterised, and a two-photon transition is observed in the D2 line spectrum. A change in spatial intensity distribution of the THz beam is observed under the effect of rotation of a linear polariser, which is theorised to be due to a vector diffraction pattern.

Supervisors: Kevin J. Weatherill and Charles S. Adams

Acknowledgements

Firstly, I would like to immensely thank my supervisors, Kevin Weatherill and Stuart Adams, for their humour, patience and goodwill in providing the support I needed to complete my studies. I must also thank in particular, Lucy (without whom, our team would likely cease to function), for all the help in writing this thesis, as well as Dani and Liam for sharing many of their invaluable pearls of wisdom. Thanks go to all members of Team Terahertz, past and present, and my labmates Gianluca and Andrew for making the experiment a joy to work on. I have to thank all the members of QLM, for making the department such a friendly and inclusive space, and such an easy place to work. I also thank the football regulars, for enabling me to injure myself in new ways every week, to distract me when the work was hard. For further distraction, thanks too go to all the Friday seminar-goers, to Alex for all the check-ins, and to Tom and Liam for inevitably being the last ones standing (or not standing). Fraser, Luke and Puya, I'm glad you all converted and showed up to support the greatest team there ever was, Sunderland AFC. I have made friends and memories for life, for which I am forever grateful. To my family and my parents, I say thank you for all you've ever done for me and for believing in me but

keeping me humble. To Becca, thank you for all your patience and love over the years.

Contents

Declaration

The work in this thesis is based on research carried out at the Quantum Light & Matter research group, Department of Physics, University of Durham, England. No part of this thesis has been submitted elsewhere for any other degree or qualification, and it is the sole work of the author unless referenced to the contrary in the text.

Publications related to this work

The following publications have been published and are related to the work in this thesis:

- S. Chen, D. J. Reed, A. R. MacKellar, L. A. Downes, N. F. Almuhawish, M. J. Jamieson, C. S. Adams, and K. J. Weatherill, "Terahertz electrometry via infrared spectroscopy of atomic vapor," *Optica* vol. 9, p. 485–491 (2022)

- S. Chen, D. J. Reed, A. R. MacKellar, L. A. Downes, N. F. Almuhawish, M. J. Jamieson, C. S. Adams, and K. J. Weatherill "THz electrometry with Rydberg atoms and all IR lasers," *2021 46th International Conference on Infrared, Millimeter and Terahertz Waves (IRMMW-THz)*, Chengdu, China, 2021, p. 1–2

- N. F. Almuhawish, S. Chen, L. A. Downes, M. J. Jamieson, A. R. MacKellar, and K. J. Weatherill, "Polarization spectroscopy of an excited state transition in Rubidium," *OSA Continuum* vol. 4, p. 2598–2605 (2021)

- Matt Jamieson *et. al*, "Implementation of a repump laser in a Rydberg atom-based THz imager" *In progress*.

- Matt Jamieson *et. al*, "Full field observation of THz vector diffraction patterns with a Rydberg atom-based imager" *In progress*.

List of Figures

List of Tables

Nomenclature

AO adaptive optics

IR infra-red

THz terahertz

MW micro-wave

DFB distributed-feedback

PID proportional-integral-differential

DSB dual sideband

ESB electronic sideband

FWHM full width half maximum

PCB printed circuit board

DAC digital to analog converter

ADC analog to digital converter

PDH Pound-Drever-Hall

DLC diode laser controller

DPD differencing photo-diode

TEC thermo-electric cooler

ECDL external cavity diode laser

TA tapered amplifier

STCL scanning transfer cavity lock

PBS polarising beam-splitter

QWP quarter wave-plate

FFT fast Fourier transform

AT Autler-Townes

EOM electro-optic modulator

MDP minimum detectable power

Introduction

Quantum technologies have become a huge area of research in the past 20 years [1], worth billions of dollars globally [2]. Atomic systems are some of the leading platforms for these emerging technologies, due to a number of their beneficial properties. They are sensitive to applied fields, possess well known internal properties, and can provide unequalled precision measurements. Additionally, any atom is identical to another atom of the same isotope, so atomic technologies can be implemented reproducibly, in a way that is self calibrating and directly traceable to SI units. An atomic sample is also identical regardless of its implementation, in contrast to, for example, solid state material platforms that require sample preparation. Applications have been found in a diverse range of fields, such as atomic clocks [3; 4], which have already revolutionised GPS systems, and sensors [5] such as gyroscopes [6; 7], magnetometers [8; 9], gravimeters [10; 11] and gradiometers [12]. Potential applications also exist in important fields such as quantum computing [13; 14], and only become more promising as associated control and laser technologies develop.

This thesis concerns the application of an atomic medium towards the field of terahertz (THz) radiation imaging, that exploits the properties of Rydberg

atoms in a thermal vapour. The work done builds upon previous work [15; 16] by characterising and optimizing the experimental parameters involved. The system demonstrates unprecedented speed, and good sensitivity compared to current technologies, and so this characterisation and optimisation is done with means towards deployment of the system into real world applications, and further improvement of the system capabilities. To this end, progress has already been made [17] towards miniaturisation of the involved components for field deployment.

This introduction will introduce the field of THz imaging, and the field of Rydberg atomic physics. The structure of the thesis will then be summarized.

1.1 Terahertz Radiation

Terahertz radiation is electromagnetic radiation that falls into a band of frequencies known as the "terahertz gap". This is a range of frequencies typically considered to be between 0.1 THz and 10 THz, in the region between microwaves and infra-red. This region is known as the "terahertz gap" because it falls between well developed electronic, microwave technologies and semiconductor based infrared technologies, meaning current generation and detection methods fall behind those in other frequency bands. Despite this, there is huge interest in developing these technologies, and much progress has been made in the past 20 years [18; 19]. This is because there are many potential use cases, both fundamental and applied, due to a range of useful properties.

For example, it is the right range to probe for many electronic and quantum properties in condensed matter [20], examining massive molecules [21], and for interpreting astronomical and cosmological signals [22]. It is well atten-

uated by water, meaning it can be used to analyse water content of biological samples in industries ranging from agriculture [23] to biomedicine [24; 25; 26]. The high frequency character compared to RF makes it a future candidate for data transmission [27; 28], as higher frequencies allow for larger network bandwidths. As THz radiation can penetrate many materials such as plastic, cardboard and cloth, but is non-ionising and can provide higher imaging resolution than longer wavelengths, other potential applications in industry vary from security systems [29] to medical diagnostic tools [30] and non-destructive testing [31].

The main areas of current research can be categorized into; detectors [32; 33], sources [34; 35; 36] and components [37], as well as in applications such as imaging and sensing. Some techniques for the generation of terahertz photons can be found in gyrotrons, quantum cascade and quantum dot lasers, photomixers and amplified multipliers. Detectors generally use either thermal methods or photoconductive methods – those that measure a temperature related change due to incoming energy, such as bolometers or Golay cells, and those that measure a change in electric current/resistance due to incoming photons [38, p. 204], respectively. A successful implementation of a terahertz imaging system would have benefits over say, X-ray imaging, in that it is non-ionising and non-hazardous to humans, as well as the fact that many materials have a spectral 'fingerprint' in the terahertz region that could help in classifying the object being imaged. Some systems use short pulsed terahertz light, as used in terahertz time domain spectroscopy (THz-TDS), while others use continuous wave light. Most systems currently are limited by the bandwidth they can image/detect and the intensities they receive. Many systems can only image a select number of pixels at a time [39], and so have to scan objects through the imager and reconstruct the object digitally — this process is generally slow.

In contrast, our imaging system is limited only by the lifetime of the Rydberg state (0.80μs), enabling the potential of real time, full field imaging at up to 1 MHz frame rates. The detection dynamic range can span over 10 orders of magnitude of power per pixel, as the upper limit on the power is determined only by the complete splitting of the transition. By appropriate choice of Rydberg states and atomic species, a relatively broadband range of THz frequencies could also be imaged with very good sensitivity.

1.2 Rydberg Atoms

Rydberg atoms are atoms with one or more valence electrons that are excited to a high principal quantum number n. This gives them large spatial wavefunctions that can be well represented by elliptical Bohr orbits. They possess a number of interesting and unique properties, such as an unusually long lifetime, and a high sensitivity to electric fields and to each other through their large electric dipole moments [40]. Figure 1.1 shows some example wavefunctions of Rydberg s-states, along with the scaling of some of these properties with n. These scaling rules lead to these properties being exaggerated at high n.

In recent decades, the development of reliable high power diode lasers with narrow linewidths has enabled the optical excitation of many alkali and alkaline earth atoms to Rydberg levels, and the field has subsequently bloomed. The ability to excite and manipulate these atoms has opened them up to a wide range of applications, from quantum optics experiments [41] to quantum computing [42; 14] and electric field sensing [43; 44; 45] and imaging [46; 47].

The python package `ARC` [48] (Alkali Rydberg Calculator) also allows for the
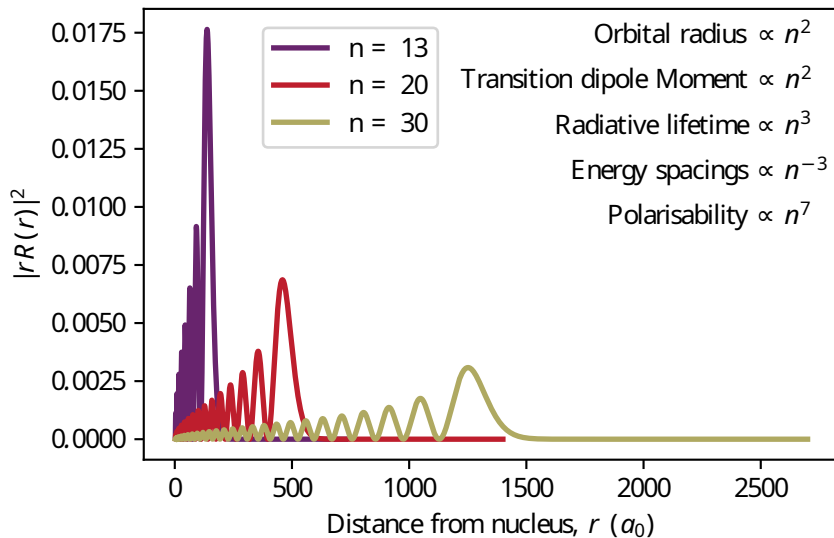
Figure 1.1: Example wavefunctions for principal quantum numer, $n = 13, 20, 30$, as a function of radial distance from nucleus. The larger the principal quantum number, the larger the size of the atom. Some other example properties' scaling with principal quantum number are shown in the top right.

easy calculation of many Rydberg atomic properties, and, where calculations are not possible, the retrieval of literature values. In the work described in this thesis, we create Rydberg atoms in a thermal ensemble by a three step laser excitation process. We exploit the strong coupling to nearby Rydberg states in the THz frequency range, to provide a method for THz-to-optical conversion, which will be described in Chapter 3. The use of Rydberg atoms, in this instance, presents a large step forward in speed and sensitivity as a detection method, compared to other methods.

1.3 Thesis Structure

In this chapter we have introduced the aim of the thesis, and provided an overview of the fields of both THz physics and Rydberg physics, where we have motivated the development of a Rydberg atom-based THz imaging system by the

rich depth of applications in the THz domain, and the sensitivity of Rydberg atoms.

In chapter 2, we will develop a theoretical framework to provide an introduction and explain the atom-light interactions which underpin the work and modelling throughout this thesis.

In chapter 3, we will introduce the details of the experimental system, across two separate experiments, including the equipment used, the control systems involved, and the data acquisition methods.

In chapter 4, we will discuss the implementation of two different frequency stabilisation methods for the Rydberg laser, based on cavity references for either experiment. A brief overview of the theory of PID controllers and Fabry Perot resonators will be given, and the theory behind the error signal generation for a Pound-Drever-Hall lock, and a scanning transfer cavity lock will be given. Stability measurements will be performed, and find both are stable to $\approx 3\%$ over time.

Chapter 5 will investigate and characterise the effect of various experimental parameters on the fluorescence signal that we image, including the laser powers, polarisations and the Rydberg and THz source detunings. Through optimisation of these parameters, an increase in signal of around 30% will be achieved. Attempts will be made to model the effects in order to confirm the validity of the findings, with reasonable agreement.

In chapter 6 we will discuss the implementation of a repump laser on the alternate hyperfine ground state. We will investigate the effect of detuning and power on the fluorescence spectra and signal, and find a potential almost seven fold increase in signal.

Finally, in chapter 7, we will provide an outlook, where some interesting but open-ended results will be described, related to the use of THz polarisers, and to dynamic temperature effects on the fluorescence signal. This chapter will also conclude the thesis.

Atom Light Theory

2.1 Introduction

This work of this thesis concerns a thermal vapour of alkali atoms that are excited to a Rydberg state by laser fields. We therefore develop here a framework for the understanding of the relevant atom-light interactions. We will provide an introduction to angular momentum theory, of which an understading is indispensable for our calculations, and detail the energy level structure of the alkali atom. We will briefly discuss the polarisation of light, in order to introduce the Stokes parameters that are used in section 5.2. We will also introduce the atom-light Hamiltonian, and derive the selection rules and decay rates from the dipole matrix element. Finally, we will introduce the density matrix formalism, in order to state the Lindblad master equation, which is used for modelling atomic populations in Chapter 5.

2.1.1 Schrödinger Equation

The behaviour of a quantum system can be described non relativistically by the action of the time dependent Schrödinger equation,

$$i\hbar\frac{\partial}{\partial t}|\psi(\vec{r},t)\rangle = \hat{H}|\psi(\vec{r},t)\rangle, \qquad (2.1)$$

where $\hat{H}$ is the Hamiltonian of the system, $\hbar$ is the reduced Plancks constant, and $|\psi(\vec{r},t)\rangle$ is an eigenstate of the system. In the position representation, these eigenstates represent wavefunctions of the system. Eigenstates that are a solution of Eqn. 2.1 can be expressed as a stationary state, $|\psi\rangle = |\psi(\vec{r},0)\rangle$, multiplied by some time dependent phase factor, like $|\psi(\vec{r},t)\rangle = \exp\left(\frac{-iEt}{\hbar}\right)|\psi(\vec{r},0)\rangle$. These stationary states are independently solutions to the time independent Schrödinger equation,

$$\hat{H}|\psi\rangle = E|\psi\rangle, \qquad (2.2)$$

where E in an eigen-energy of the system. In this way, the information about the energies of a system is encoded in the Hamiltonian, which can be decomposed by an eigenvalue problem. Many problems can be solved by solution of 2.1, including the generation of the energy level spectrum of caesium, which will be discussed in section 2.2.

2.1.2 Angular Momenta

The theory of angular momentum is crucial in quantum mechanics and is used throughout this thesis, appearing in the derivation of, e.g selection rules and dipole matrix elements. As such, in this section, we will introduce the topic to develop a framework, culminating in the Wigner-Eckart theorem, which is indispensable in the calculation of atom-light interactions. Useful references for this section can be found at [49; 50; 51; 52].

To generate the angular dependent solutions for the atomic Hamiltonian, we introduce an angular momentum operator, $\hat{J}$, that generates rotations. $\hat{J}$, being a rank 1 spherical tensor operator [53], is by definition a Hermitian operator that obeys the standard commutation relations,

$$[\hat{J}_i, \hat{J}_j] = i\hbar\epsilon_{ijk}\hat{J}_k, \tag{2.3}$$

where ϵ_{ijk} represents the Levi-Cevita symbol, and i,j and k may run over Cartesian spatial co-ordinates. We also define ladder operators, consisting of a raising and a lowering operator composed of linear combinations of $\hat{J}_i$:

$$\hat{J}^{\pm} = \hat{J}_x \pm i\hat{J}_y \tag{2.4}$$

$\hat{J}^+$ and $\hat{J}^-$, along with $\hat{J}_z$, together form an irreducible representation of the so(3) Lie algebra, with common eigenvectors v_j that span a vector space, V, of dimension $2j+1$, where j is the largest eigenvalue of the basis set, and can take a value $j = 0, 1/2, 1, 3/2, 2, \ldots$. [52]. By this we mean, given that $\hat{J}_z\, v_j = \lambda_j v_j$, we can use $\hat{J}^{\pm}$ to construct the remaining basis vectors, which form the state vectors of the atomic system, with general quantised angular momentum, j. We can also introduce a Casimir operator acting on this representation, $\hat{J}^2 = \hat{J}_x^2 + \hat{J}_y^2 + \hat{J}_z^2$ that is simulatenously observable with another component, i.e $\hat{J}_z$. That is to say, $[\hat{J}^2, \hat{J}_z] = 0$, and as such we may choose as a basis for our representation, the set of simultaneous normalised eigenstates, $|jm\rangle$, whose eigenvalues corresponds to:

$$\hat{J}^2 |jm\rangle = j(j+1)\hbar^2 |jm\rangle$$
$$\hat{J}_z|jm\rangle = m\hbar |jm\rangle. \tag{2.5}$$

For a given representation, j is fixed to a specific value, and m varies like,

$$j = 0, 1/2, 1, 3/2, 2, \ldots$$
$$m = -j, -j + 1, \ldots, j - 1, j. \tag{2.6}$$

For example, in the case of the orbital angular momentum operator, $\hat{L}$, the eigenfunctions on a 3D sphere,

$$\begin{aligned}
\Psi_{l,m}(\theta, \phi) &= \langle \theta, \phi | l, m \rangle \\
&= (-1)^m \left[\frac{(2l+1)(l-m)!}{4\pi(l+m)!} \right]^{1/2} P_l^m(\cos\theta) e^{im\phi}, \quad m \geq 0
\end{aligned} \quad (2.7)$$

form spherical harmonics, where P_l^m are the associated Legendre functions and l takes integer values, where the values of l and m represent the azimuthal quantum number and the magnetic quantum number respectively.

The use of representation theory is advantageous when it comes to the addition of angular momenta. In order to accurately describe atomic systems, we need to find eigenstates for compound systems of angular momenta, i.e eigenstates for the total angular momentum operator,

$$\hat{j} = \hat{j}_1 + \hat{j}_2, \quad (2.8)$$

where $\hat{j}_{1,2}$ may be any general angular momentum operator, e.g the orbital or spin angular momentum operator. If V_l and V_m are the irreducible representations spanned by the set of eigenstates of $\hat{j}_1$, and $\hat{j}_2$, then the representation spanned by the eigenstates of $\hat{j}$ is $V_l \otimes V_m$, and is in general, not irreducible. It can, however, be decomposed into a direct sum of irreducible representations like [52][page=386],

$$V_l \otimes V_m \cong V_{l-m} \oplus V_{l-m+1} \oplus \cdots \oplus V_{l+m-1} \oplus V_{l+m}, \quad (2.9)$$

providing $l \geq m$, where $\cong$ represents an isomorphism. It is common to form direct product states like this, where V_l is a representation of the SO(3) Lie group of rotations and V_m is a representation of the SU(2) Lie group, which encapsulates internal degrees of freedom, such as the spin or isospin of a particle. In this sense, for an electron, with spin eigenvalue 1/2, the product states are

formed in the representation,

$$V_l \otimes V_{1/2} \cong V_{l+1/2} \oplus V_{l-1/2}.$$

This decomposition can more easily give us physical insight into the system. For example, in order to perform calculations, we may want to diagonalise the operators acting in a vector space with a suitable basis, which is more easily done with this decomposition. We can create new basis states in the $V_{j_1} \otimes V_{j_2}$ space, in what is known as the uncoupled representation, by taking direct product eigenstates,

$$|j_1 m_1 j_2 m_2\rangle = |j_1 m_1\rangle |j_2 m_2\rangle. \qquad (2.10)$$

In this basis, $\hat{j}_1^{\,2}, \hat{j}_2^{\,2}, \hat{j}_{1_z}$, and $\hat{j}_{1_z}$ are simultaneously diagonal [50]. We may, however, want $\hat{j}^2, \hat{j}_z, \hat{j}_1^{\,2}$, and $\hat{j}_2^{\,2}$ to be diagonal - in which case we can also generate the coupled representation by taking a linear combination of the product eigenstates, akin to equation 2.9,

$$|j_1 j_2 j m\rangle = \sum_{m_1, m_2} C(j_1 j_2 j : m_1 m_2 m)|j_1 m_1\rangle |j_2 m_2\rangle, \qquad (2.11)$$

where the coefficients $C(j_1 j_2 j : m_1 m_2 m)$ are the *Clebsch-Gordan* coefficients. The general total angular momentum operator, $\hat{j}$, follows the same commutation relations from Equation 2.3, and as such, acting in the coupled representation, produces eigenvalues of the same form as (2.5), where j and m fulfill the triangular conditions,

$$j = |j_1 - j_2|, |j_1 - j_2 + 1|, \ldots, j_1 + j_2 - 1, j_1 + j_2$$

$$m = m_1 + m_2. \qquad (2.12)$$

The Clebsch-Gordan coefficients become incredibly useful, for example, when calculating the matrix elements of a spherical tensor operator, with the Wigner-Eckart theorem,

$$\langle j' m' | \hat{T} | j m\rangle = C(j_1 j_2 j : m_1 m_2 m)\langle j' || \hat{T} || j\rangle, \qquad (2.13)$$

where $\langle j'||\hat{T}||j\rangle$ represents a reduced matrix element, that depends only on j, and not on m. The CG coefficients therefore provide the weightings on the decomposition from (2.9) (see [51]), and allows us to generate all the matrix elements, from knowledge of one. (2.13) essentially represents the rotational symmetry of the system - we can express the CG coefficients as,

$$C(j_1 j_2 j : m_1 m_2 m) = (-1)^{j_1-j_2+m}\sqrt{2j+1}\begin{pmatrix} j_1 & j_2 & j \\ m_1 & m_2 & -m \end{pmatrix} \qquad (2.14)$$

where $\begin{pmatrix} \dots \end{pmatrix}$ represents the Wigner-3j symbol. The 3j symbol encodes the information in a more symmetrical way, and is zero when the conditions of (2.12) and (2.6) are not upheld [54; 55]. This will be useful for determining selection rules when we come to calculate the matrix elements of the dipole operator.

2.2 Atomic Structure

Alkali atoms such as caesium may be considered hydrogen-like, if they are treated as a valence electron orbiting a core consisting of the nucleus plus the closed shells of electrons. In the central field approximation, we can simplify the interactions of the inner shell electrons down to a spherically symmmetric potential, $V_{\mathrm{CF}}(\vec{r})$ [56]. To describe the energy levels of an alkali atom such as caesium, we therefore can adapt a model for the hydrogen atom - an electron in a spherically symmetric Coulomb potential - with some modification to account for the inner core electrons. To this end, we will summarise the derivation of the hydrogenic energy levels.

2.2.1 Gross Structure

The Hamiltonian for a spinless, non relativistic two body (nucleus & electron) system, interacting with a potential $V(|\vec{r_1} - \vec{r_2}|)$, is given by

$$\hat{H} = \frac{\hat{p_1}^2}{2m_1} + \frac{\hat{p_2}^2}{2m_2} + V(|\vec{r_1} - \vec{r_2}|), \qquad (2.15)$$

where $p_{1,2}$ and $m_{1,2}$ represent the momentum and mass of each particle. When applying this Hamiltonian to the time independent Schrödinger equation (TISE, eqn. 2.2) and transforming to a centre of mass reference frame, where $\vec{r} = \vec{r_1} - \vec{r_2}$, we acquire two separable equations - a centre of mass equation, and an interaction equation. The centre of mass equation describes the translational symmetries of the system, and can be solved by a linear combination of plane wave solutions. As such, the energy spectrum is continuous and this equation represents the equation for a free particle. The interaction equation is of more interest, represented by the Hamiltonian,

$$\hat{H} = -\frac{\hbar^2}{2\mu}\nabla_{\vec{r}}^2 + V(r), \qquad (2.16)$$

where $\mu = \frac{m_1 m_2}{m_1 + m_2}$ is the reduced mass of the two bodies and r is the radial component of the position vector $\vec{r}$. In solving for energies of this system, the wavefunction can again be separated, into a radial part, and an angular part, described by

$$\phi(\vec{r}) = R(r)Y(\theta, \phi). \qquad (2.17)$$

Solutions to the angular part are eigenstates of $\hat{L}^2$, and are described by spherical harmonics (equation 2.7). The radial part can be solved by functions involving generalised Laguerre polynomials, and, taking $V(r) = \frac{-e^2}{4\pi\epsilon_0 r}$, generates an energy spectrum of the form,

$$E_n = \frac{\hbar^2}{2m_e a_0^2} = -hc\frac{R_\infty}{n^2}, \qquad (2.18)$$

where $m_1 = m_e$ is the mass of the electron, $a_0 = \frac{4\pi\epsilon_0\hbar^2}{\mu e^2}$ is the Bohr radius, $R_\infty = m_e e^4 / 8\epsilon_0^2 h^3 c$ is the Rydberg constant and n represents the principal quantum number.

For a hydrogen-like alkali atom, these energy levels can be modified by an experimentally obtained *quantum defect*, δ_l, by [56]

$$E_{nl} = -hc \frac{R_\infty}{(n - \delta_l)^2}.$$
(2.19)

δ_l is angular momentum-dependent, and becomes smaller as the orbital angular momentum number, l, becomes larger, as the electron becomes further away from the core potential.

2.2.2 Fine Structure

In reality, the electron in this system has a spin, with an associated intrinsic magnetic moment $\hat{\mu} = -g_s \mu_B \hat{s}$, where g_s is the electron spin g-factor, μ_B is the Bohr magneton and $\hat{s}$ is the spin operator. This interacts with the magnetic field generated due to the orbital motion of the electron to produce a perturbation on the gross structure Hamiltonian, of the form $\hat{H}'_{\text{s-o}} = -\hat{\mu} \cdot \hat{B}$. The magnetic field can be non-rigorously derived from the Biot-Savart law [56; 53] as

$$\hat{B} = \frac{\hbar}{m_e c^2} \left(\frac{1}{er} \frac{\delta V}{\delta r} \right) \hat{l},$$
(2.20)

where $\hbar\hat{l} = \hat{r} \times m_e \hat{v}$ is the orbital angular momentum operator. Substituting in, and accounting for a *Thomas precession* factor that arises from the full relativistic derivation, which can be encapsulated by replacing g_s with $g_s - 1$, the interaction Hamiltonian becomes,

$$\hat{H}'_{\text{s-o}} = (g_s - 1) \frac{\hbar^2}{2m_e^2 c^2} \left\langle \frac{1}{er} \frac{\delta V}{\delta r} \right\rangle \hat{l} \cdot \hat{s}.$$
(2.21)

This is known as the spin-orbit coupling, and leads to the fine structure splitting of energy levels, through the $\hat{l} \cdot \hat{s}$ term. Other perturbations required to fully describe the fine structure Hamiltonian include the Darwin term, and a term to account for the relativistic speeds of the electron, but for a heavy alkali atom such as caesium, the spin-orbit term dominates [56]. To calculate the energy splittings, we move to a coupled basis (eqn. 2.10) in order to evaluate $\hat{l} \cdot \hat{s}$. We take the total electronic angular momentum to be the sum of the orbital and spin angular momentum, and define the operator, $\hat{j} = \hat{l} + \hat{s}$. The dot product of $\hat{l}$ and $\hat{s}$ can be expressed in terms of $\hat{j}^2$, and thereby, the energy splitting can be found from the expectation value of eqn. 2.21 as,

$$E_{\text{s-o}} = \frac{\beta}{2}[j(j+1) - l(l+1) - s(s+1)], \tag{2.22}$$

where β collects the terms and expectation values of the factor in front of $\hat{l} \cdot \hat{s}$ from 2.21, and j, l and s are the quantum numbers for their respective Casimir operators. A particular energy level in the fine structure basis may be described by its configuration, $n^{2s+1}l_j$, where n is the principal quantum number, l is the angular momentum quantum number, $2s + 1$ is the multiplicity of the level (with spin quantum number, s) and j is the total angular momentum number. l is usually given in spectroscopic notation, where $0 = \text{S}, 1 = \text{P}, 2 = \text{D}$, etc. For alkali atoms with a single valence electron, the spin is always $1/2$, so the multiplicity term is neglected. For example, the ground state of caesium can be expressed as $6\text{S}_{1/2}$.

2.2.3 Hyperfine Structure

Further correction to the energy level structure can be made, that leads to hyperfine structure. This predominantly arises from the interaction of the nuclear magnetic moment with the magnetic flux density generated by the elec-

trons, in the form of $-\hat{\mu}_I \cdot \hat{B}$. The nuclear magnetic moment can be described by $\hat{\mu}_I = g_I \frac{m_e}{m_p} \mu_B \hat{I}$, where $m_{e,p}$ are the masses of the electron and proton, and $_I$ is the nuclear spin g-factor. Ultimately, the hyperfine perturbation Hamiltonian can be written in the form,

$$\hat{H}'_{\text{HFS}} = A\hat{I} \cdot \hat{J}, \tag{2.23}$$

where A is the experimentally obtained hyperfine constant, specific to the level and atomic species. A recent survey of measurements of these values can be found at [57]. By the same method as for the l-s coupling regime, we can introduce a total atomic angular momentum operator, $\hat{F} = \hat{I} + \hat{J}$, to calculate the expectation value of this Hamiltonian, and determine the energy splittings. This takes the form of,

$$E_{\text{HFS}} = A\langle \hat{I} \cdot \hat{J} \rangle = \frac{A}{2}[F(F+1) - I(I+1) - J(J+1)], \tag{2.24}$$

where F, I and J are the quantum numbers for their respective Casimir operators. This hyperfine splitting is largest for $l = 0$, and decreases with increasing n, meaning that for Rydberg states, the splitting is negligible, as can be seen by the scaling laws in Figure 1.1. Caesium has a nuclear spin, $I = 7/2$.

2.3 Polarisation of light

In the theory required in this thesis, it is generally sufficient to treat light in a classical sense, and the atoms it interacts with in a quantum sense, by the so-called semiclassical approach. We make this approximation motivated by the predominant use of strong coherent laser light, that consists of many photons, to drive optical transitions, meaning that effects relating to the population of the quantised field do not, in general, need to be considered. In this sense, we

can treat light as a travelling electromagnetic plane wave, with an electric field component, $\vec{E}$, and a magnetic field component, $\vec{H}$, oscillating perpendicular to each other, along the Poynting vector. The main element of light that will be discussed here is the polarisation, in order to introduce section 5.2. Useful references for this can be found at [58; 59; 60].

The polarisation of the wave provides a description of the sense with which the electric field vector oscillates. In general, the electric field can be described, in complex notation, at a point in space and time by

$$\vec{E}(\vec{r}, t) = \vec{E_0} e^{i(\vec{k} \cdot \vec{r} - \omega t)}, \tag{2.25}$$

where $\vec{k} = \frac{2\pi}{\lambda}$ represents the wavevector, and ω the angular frequency. Taking the real part, coherent light can be decomposed into cartesian components for a transverse wave travelling in the z- direction as,

$$\vec{E}(z, t) = \mathbf{i} E_{0x} \cos(kz - \omega t) + \mathbf{j} E_{0y} \cos(kz - \omega t + \epsilon), \tag{2.26}$$

where ϵ is a relative phase difference between the two components. This phase difference determines the state of polarisation. When $\epsilon = \pm m\pi, m \in \mathbb{N}$, then the two components oscillate in phase with each other, and the light is considered linearly polarised, because the E-vector oscillates along a line in space. When $\epsilon = \frac{\pi}{2} \pm 2m\pi, m \in \mathbb{N}$, then the components are out of phase with each other, resulting in circular polarisation, because as the E-vector rotates, it traces out a circle. These are two special cases of the more general, elliptical polarisation. The equation that describes this ellipse can be given by [58],

$$\tan 2\psi = \frac{2E_{x0}E_{y0} \cos \epsilon}{E_{x0}^2 - E_{y0}^2}, \tag{2.27}$$

where ψ is the angle with respect to the (E_x, E_y)–coordinate system. A useful notation to describe the polarisation state of light is the *Stokes parameters* [61],

described by,

$$S_0 = \langle E_x \rangle_T^2 + \langle E_y \rangle^2 = 2I_0 \tag{2.28a}$$

$$S_1 = \langle E_x \rangle^2 - \langle E_y \rangle^2 = 2I_1 - 2I_0 \tag{2.28b}$$

$$S_2 = \langle 2E_{x0} E_{y0} \cos \epsilon \rangle = 2I_2 - 2I_0 \tag{2.28c}$$

$$S_3 = \langle 2E_{x0} E_{y0} \sin \epsilon \rangle = 2I_3 - 2I_0, \tag{2.28d}$$

where $\langle \ldots \rangle$ denotes a time average which can be dropped in the case of perfectly monochromatic light where there is no time dependence. These Stokes parameters can be found by effectively inserting four different filters into the light path, and measuring the resultant intensity with each, represented by I_i for each Stokes parameter.

They describe, in their respective order, the total intensity of the light, the degree of horizontally polarised light compared to vertically polarised, the degree of linear polarisation along the an axis $45°$ to the x-axis, compared to that at $90°$, and the degree of right-handed circular light compared to left-handed circular [62]. A measurement of all four Stokes parameters fully characterises the polarisation state of the light.

They each form components of a Stokes vector, $\vec{S} = (S_0, S_1, S_2, S_3)$, which can be manipulated using Mueller calculus [58], in order to describe the effect of different polarisation components on the light. The span of this vector describes the *Poincaré sphere*, by conversion of the parameters to,

$$S_0 = I \tag{2.29a}$$

$$S_1 = Ip \cos(2\psi) \sin(2\chi) \tag{2.29b}$$

$$S_2 = Ip \sin(2\psi) \cos(2\chi) \tag{2.29c}$$

$$S_3 = Ip \sin(2\chi), \tag{2.29d}$$

where I is the intensity of the light, p is the degree of polarisation defined by $p = \frac{(S_1^2 + S_2^2 + S_3^2)^{1/2}}{S_0}$, where $(0 \leq p \leq 1)$ and 2ψ and 2χ are spherical co-ordinates, defined by $2\psi = \tan^{-1} \frac{S_2}{S_1}$ and $2\chi = \tan^{-1} \frac{S_3}{\sqrt{S_1^2 + S_2^2}}$ respectively [62]. By this formalism, an arbitrary polarisation state may be described by a vector on the Poincaré sphere, described by the Stokes parameters.

We can also realise an arbitrary polarisation state in a chosen basis as a coherent superposition of basis states. Linear polarisation, for example, may be described by an equal superposition of left and right handed circular polarised light, like $|\psi\rangle = \frac{1}{\sqrt{2}}(|R\rangle + |L\rangle)$. This principle allows for the classical theory to tend towards a quantum one, that can describe the polarisation state of a single photon [63]. The quantum analog of the polarisation is the angular momentum, which, when interacting with matter, is transferred in quanta of magnitude $\pm\hbar$. The angular momentum transferred by each photon is described by a probability amplitude associated with each basis state. In the special cases of right and left circular light, the angular momentum transferred is precisely $+\hbar$ and $-\hbar$ respectively. In order to preserve angular momentum, the matter undergoes a transition to another state, known as either a σ^+, σ^- or π transition. These correspond to transitions in which $\Delta m = 1, -1, 0$ respectively, where m is the projection of the angular momentum operator onto the z-axis (see section 2.4). Which transitions are allowed depends on the orientation of the polarisation state / E-field vector with respect to a quantisation axis, which is essentially the z-axis of the co-ordinate system in which the atomic wave functions are defined. For example, $\sigma^\pm$ may be induced when the E field vector is perpendicular to the quantisation axis, and $\pm\hbar$ is added to the z-component of the angular momentum, and π transitions may be induced when the E field vector is parallel with the quantisation axis, and $\pm\hbar$ is added to the other components.

2.4 Atom-Light Interaction

The atoms in this experiment were subject to coherent light fields in the form of lasers. This interaction occurs most strongly between the electric dipole moment of the atom, $\hat{\mathbf{d}} = -e\hat{\mathbf{r}}$ and the electric field of the light field. As in the previous section, we apply the semiclassical approach, where the light field is treated classically (as eqn. 2.25). We also apply the dipole approximation, given that the given the spatial variation of the electric field is negligible over the effective diameter of the atom, i.e that $\lambda \gg a_0$, and that the magnetic field, $\hat{B} \propto \hat{E}/c^2$, is much weaker than the electric field, and so magnetic and higher order quadrapoles do not need to be considered. In this thesis, only modest principal quantum numbers are reached in the Rydberg states so the size of the atoms never approaches the wavelength and the dipole approximation continues to be valid. We also assume that the amplitude of the electric field varies slowly compared to its frequency, ω. This means the interaction Hamiltonian can be given by,

$$\hat{H}_I = -\hat{\mathbf{d}} \cdot \hat{\mathbf{E}}$$

$$= e\hat{\mathbf{r}} \cdot \tilde{\mathbf{e}}\hat{\mathbf{E}}_{\mathbf{0}}\cos(\omega t), \tag{2.30}$$

where $\tilde{\mathbf{e}}$ represents a unit polarisation vector, to account for the orientation between the atomic dipole moment and the field. The action of $\hat{H}_I$ is to couple two states together [64], from an initial state, g, to an excited state e. Given that the light fields are close to an atomic resonance, we can assume a two level atom for simplicity [65], and adopting a matrix approach in the $(|g\rangle, |e\rangle)$ basis, we can define an atomic Hamiltonian as,

$$\hat{H}_{\text{atom}} = \begin{pmatrix} E_e & 0 \\ 0 & E_g \end{pmatrix} = \begin{pmatrix} E_g + \hbar\omega_0 & 0 \\ 0 & E_g \end{pmatrix}, \tag{2.31}$$

where $\omega_0 = (E_e - E_g)/\hbar$ is the resonance frequency. The full atomic plus interaction Hamiltonian is then,

$$\hat{H} = \hat{H}_{\text{atom}} + \hat{H}_I = \begin{pmatrix} E_g + \hbar\omega_0 & \hbar\Omega(t)\cos(\omega t) \\ \hbar\Omega^*(t)\cos(\omega t) & E_g \end{pmatrix}, \qquad (2.32)$$

where we have defined the Rabi frequency,

$$\Omega = -\frac{eE_0\langle e|\hat{r}|g\rangle}{\hbar}. \qquad (2.33)$$

The Rabi frequency indicates the strength of the atom-light interaction through the electric field amplitude, and the term, $D = \langle e|\hat{r}|g\rangle$ which is known as the dipole matrix element. The dipole matrix element characterises many of the properties of a transition. It is often expressed in atomic units (in terms of ea_0) by making the conversion $\bar{r} = \hat{r}/a_0$ [66]. The transition specific line strength $\bar{S}_{\psi\rightarrow\psi'}$, for example, is defined as the square of the dipole matrix element,

$$\bar{S}_{\psi\rightarrow\psi'} = |\langle e|\bar{r}|g\rangle|^2. \qquad (2.34)$$

Related quantities that depend on the dipole matrix element include the Einstein A and B coefficients, the transition oscillator strength, and the absorption cross section [66].

The Hamiltonian in 2.32 can be expressed in a more mathematically convenient form, by making the rotating wave approximation, where we transform to a rotating frame and neglect quickly oscillating terms, to acquire,

$$\hat{H} = \frac{\hbar}{2} \begin{pmatrix} 0 & \Omega \\ \Omega^* & -2\Delta \end{pmatrix}, \qquad (2.35)$$

where $\Delta = \omega - \omega_0$ is the detuning of the driving field. Throughout this thesis, the detuning referred to will be the linear detuning, given by $\Delta/2\pi$. For this

two-level system, effective eigen-energies of this Hamiltonian can be found as

$$E_{\pm} = \frac{\hbar\Delta}{2} \pm \frac{\hbar\Omega_{\text{eff}}}{2},$$ (2.36)

where $\Omega_{\text{eff}} = \sqrt{\Delta^2 + \Omega^2}$ is the effective Rabi frequency, and the subscripts ($\pm$) are to represent the corresponding states in the "dressed atom" basis [67]. The interaction effectively shifts the energy levels of the unperturbed Hamiltonian, in what is known as the AC stark effect [68].

2.4.1 Selection Rules

From the dipole matrix element, we can derive the selection rules for dipole allowed transitions. An energy level in the LS-coupling basis can be described by $|\psi(n, S, L, J, m_J)\rangle$. We can express this in terms of Clebsch-Gordan coefficients by,

$$\psi(n, S, L, J, m_J) = \sum_{m_L} \sum_{m_S} C(L, m_L, : S, m_S | J m_J) \psi_L(n, L, m_L) \psi_S(S, m_S).$$ (2.37)

Now, the dipole matrix element can be written in terms of separated ψ_L and ψ_S,

$$D = \langle \psi'_S(S', m'_S) | \langle \psi'_L(n', L', m'_L) | \bar{\mathbf{r}} | \psi_L(n, L, m_L) \rangle | \psi_S(S, m_S) \rangle.$$ (2.38)

As the electric dipole moment operator does not couple with the spin degree of freedom, it commutes through it, and, assuming an orthonormal basis of ψ, eqn. 2.38 becomes,

$$D = \langle \psi'_L(n', L', m'_L) | \bar{\mathbf{r}} | \psi_L(n, L, m_L) \rangle \delta_{SS'} \delta_{m_s m'_s},$$ (2.39)

where δ_{ab} is the Kronecker delta, which takes unity value for $a = b$ and zero otherwise. This gives us our first selection rule: for dipole allowed transitions, $\Delta S = 0$.

By writing the Clebsch-Gordan coefficients in terms of the Wigner-3j symbols according to eqn. 2.14, and substituting into 2.34, we acquire a line strength,

$$\bar{S}_{\psi \to \psi'} = (2J+1)(2J'+1) \left| \begin{pmatrix} J & 1 & J' \\ m_J & q & -m'_J \end{pmatrix} \right|^2 \left| \begin{Bmatrix} J & 1 & J' \\ L' & S & L \end{Bmatrix} \right|^2 |\langle nL||\bar{\mathbf{r}}||n'L'\rangle|^2,$$
(2.40)

where q is a parameter to represent the polarisation of the light, with values of -1, 0 and 1 for σ^-, π and σ^+ transitions respectively, $\{\dots\}$ is the Wigner-6j symbol, which represents a coupling of 3-j symbols, and $\langle \dots ||\bar{\mathbf{r}}|| \dots \rangle$ is the reduced matrix element, as in eqn 2.13. The remaining selection rules can then be derived from the symmetries of the Wigner symbols - the Wigner-3j symbol is non-zero only when $m_J + q = m'_J$ so that $\Delta m_J = \pm 1, 0$, whilst $m_J = 0 \to m_j = 0$ is forbidden. The Wigner-6j symbol is non-zero only when

$$\delta(J, 1, J'), \quad \delta(J, S, L), \quad \delta(L', 1, L), \quad \delta(L', S, J'), \quad (2.41)$$

are non-zero, where $\delta(j_1, j_2, j_3)$ represents the triangular delta, that takes unity value when j_1, j_2, and j_3 obey the triangular relations of equation 2.12, and when they have an integral sum [54]. This culminates in the selection rules $\Delta L = \pm 1, 0$ and $\Delta J = \pm 1, 0$, whilst preserving the conservation of spin, so that $J = 0 \to J = 0$ is forbidden. The above derivation applies identically in the hyperfine basis, by replacing L, S and J with J, I and F, respectively. By doing so, we additionally find $m_F + q = m'_F$, and $\Delta F = \pm 1, 0$ whilst preserving nuclear spin, so that $F = 0 \to F = 0$ and $m_F = 0 \to m_F = 0$ are forbidden. The dipole matrix element in the hyperfine basis may be expanded multiple times with Wigner symbols to perform calculations in this basis - an example of this can found in [69]. The reduced dipole matrix elements can be experimentally calculated from, for example, measurements of decay rates, or approximated by numerical integration of radial overlap integrals. The python

package `ARC` [48] contains a repository for reduced dipole matrix element values from literature, and a built in overlap integral calculator, and as such in invaluable in calculating dipole matrix elements used throughout this thesis, such as to calculate line strengths in section 5.2.

2.4.2 Decay Rates

The Einstein A factor, representing the decay rate, is calculated for a degenerate level by the summation of all the lower lying states in the transition, and the average over all the upper states. It can be calculated from the dipole matrix element as [70],

$$A_{21} = \frac{1}{\tau_R} = \frac{e^2 \omega_0^3}{3\pi\epsilon_0 \hbar c^3} \frac{g_1}{g_2} D_{12}, \tag{2.42}$$

where τ_R is the radiative lifetime for the transition, and g_1 and g_2 are the degeneracies of the lower and upper states. The cubed dependence on ω_0 means decays to the lowest possible lying states, with the largest frequency difference are preferentially weighted. The dependence on the dipole matrix element incorporates the selection rules for allowed decays. In general, the full lifetime of the state can be modified by absorption of black body radiation, and by non radiative processes such as collisional transfer. Equation 2.42 was used in the Monte Carlo decay model used to determine the fluorescence spectra in section 5.3 [71].

2.4.3 Density Matrix Formalism

Whilst the Schrödinger equation is an incredibly useful tool for modelling isolated coherent systems, it is not well equipped to deal with incoherent processes such as decay. To enable calculations for multi-level systems coupled

to the environment, we introduce a density matrix operator [72], defined by the inner product $\hat{\rho} = |\psi\rangle\langle\psi|$, which on an orthonormal basis, $\{|c_i\rangle\}$, ($|\psi\rangle = \sum_i^2 c_i|\psi_i\rangle = |c_i\rangle$) can be represented

$$\hat{\rho} = |\psi\rangle\langle\psi| = (c_1, c_2)\begin{pmatrix} c_1 \\ c_2 \end{pmatrix} = \begin{pmatrix} |c_1|^2 & c_1 c_2^* \\ c_1^* c_2 & |c_2|^2 \end{pmatrix}. \tag{2.43}$$

In matrix form, the diagonal elements, ρ_{ii}, represent state populations, and the off-diagonals, ρ_{ij}, represent coherence terms. The trace of the matrix is unity, so that the sum of the populations is normalised. The equivalent of the Schrödinger equation in this formalism is given by the Louiville, or von-Neumann equation,

$$i\hbar\frac{d\hat{\rho}}{dt} = \left[\hat{H}, \hat{\rho}\right]. \tag{2.44}$$

We can introduce a decay operator, $\hat{\mathbb{L}}$, to arrive at the full Lindblad master equation,

$$i\hbar\frac{d\hat{\rho}}{dt} = \left[\hat{H}, \hat{\rho}\right] + \hat{\mathbb{L}}(\hat{\rho}). \tag{2.45}$$

$\hat{\mathbb{L}}$ can be related to jump / collapse operators through a quantum optical treatment. Here, in an extension from our two level system to a multi level system, we assume a ladder configuration, where each state decays to the one directly below it. We can then describe it as $\hat{\mathbb{L}}(\hat{\rho}) = \hat{\mathbb{L}}_{\text{atom}} + \hat{\mathbb{L}}_{\text{dephasing}}$, where $\hat{\mathbb{L}}_{\text{atom}}$ describes atomic decays, and $\hat{\mathbb{L}}_{\text{dephasing}}$ describes dephasing due to a finite laser linewidth. The elements of $\hat{\mathbb{L}}_{\text{atom}}$ are related to the atomic decay rates, $\Gamma_n = A_{n,n-1}$, where the diagonal elements are given by $L_{ii} = \Gamma_{i+1}\rho_{i+1,i+1} - \Gamma_i\rho_{ii}$ and the off-diagonal elements are described by $L_{i,j,i\neq j} = -\frac{\Gamma_i+\Gamma_j}{2}\rho_{ij}$ [67], where i and j represent the indices of the square matrix. $\hat{\mathbb{L}}_{\text{dephasing}}$ is represented by a hollow matrix, whose off-diagonal elements are given by $L_{i,j,i\neq j} = (\sum_{i=\min(i,j)}^{\max(i,j)} \gamma_{i,i+1})\rho_{ij}$ [73], where $\gamma_{n,n+1}$ is the linewidth of the laser coupling the n and $n+1$-th level.

Solution of eqn. 2.45, with the atomic Hamiltonian given in eqn. 2.32 describes the dynamics of the system, but is difficult to solve analytically. Nevertheless it can be solved numerically and, taking the time derivative to zero, can provide the steady state solutions for the system. This powerful modelling technique is used in sections 6.1.1 and 5.4, for example, to numerically model populations in a five-level ladder system.

CHAPTER 3

Experimental Setup

In this chapter, the experimental setups used in this thesis are described, along with an outline of the specific atomic system used. Firstly, a general overview of the imaging technique and atomic level system will be provided in Section 3.1. Section 3.2 will then go into further detail about the optical setups used to implement and investigate the imaging system, including a description of each laser system, and the frequency stabilisation schemes used to lock them. Section 3.3 will describe the THz sources used to generate the THz fields used throughout this thesis. Specifications will be provided as well as details of how the THz field was manipulated. Section 3.4 will describe the methods and equipment used to acquire data, and process it via Python. Finally, section 3.5 will describe the methods and equipment used to adjust parameters in the experimental setup in a controllable and repeatable way, generally through computer control via Python.
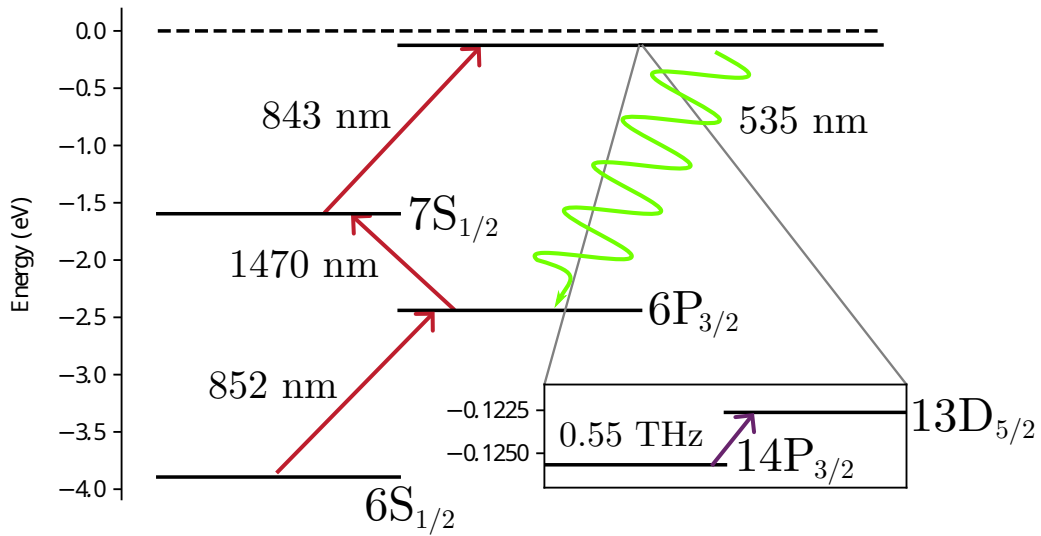
Figure 3.1: Energy level diagram showing the excitation and fluorescence transitions in caesium for this experiment. The red arrows represent laser excitations, whilst the purple represents the THz field coupling, and the green represents fluorescence along the main pathway. The dotted line shows the ionization limit. The energy levels in the order they move through are: $6S_{1/2}$, $6P_{3/2}$, $7S_{1/2}$, $14P_{3/2}$ and $13D_{5/2}$. The last two states are very close in energy to each other, so are shown in the zoomed inset. Energy level values are taken from [74].

3.1 Overview

The main operating principle of the THz imaging system is the use of caesium Rydberg atoms as a medium for up-conversion of difficult-to-detect THz photons to easy-to-detect optical photons. The atomic level scheme chosen for these experiments is shown in Figure 3.1.

Atoms in a 10 mm x 10 mm cubic quartz glass cell are excited with CW lasers via a ladder scheme to a Rydberg state, $|14P_{3/2}\rangle$. From there, in the absence of any THz field, they decay back to the ground state via a variety of pathways, producing optical fluorescence across a range of wavelengths, including the visible. When in the presence of a resonant THz field, however, the atoms are coupled to the $|13D_{5/2}\rangle$ state, where a dominant decay pathway is opened up

to the $|6\mathrm{P}_{3/2}\rangle$ state, producing a strong peak in the fluorescence spectrum, at 535 nm. This green fluorescence essentially acts as an indicator for the presence of a THz field at the position of the Rydberg atoms. By forming a laser 'light sheet' inside the vapour cell, we can create a 2D plane of Rydberg atoms. The premise of the technique is then that the spatial distribution of the THz field can be detected by the emission of this green fluorescence from the Rydberg atoms. In order to take images of the THz field, this fluorescence can be isolated by an optical notch filter and simply imaged by an optical CMOS/CCD camera.

In our experiment, we couple the two Rydberg states ($|14\mathrm{P}_{3/2}\rangle$ and $|13\mathrm{D}_{5/2}\rangle$) by generating a THz field from a commercial THz source (see sec 3.3). When coupling with the THz field, some atoms still decay from the lower Rydberg state, via a variety of pathways back to a lower state, producing unwanted background fluorescence. In order to remove this background and isolate the effect of the THz field, for every image, we take an effective background image. We do this by taking an image with the THz source off (or maximally attenuated) and subsequently taking an image with the THz source on. We say that one measurement consists of these two images. We give these images the labels "THz Off", and "THz On" respectively. To describe these images quantitatively, we can define a fluorescence value, F. When analysing full images, F will take the form of an array of pixel values or, when making measurements, F will take the form of a single averaged pixel value, where a subset of the image, labelled a 'region of interest', will be averaged over. We can then define a fluorescence signal from a signal measurement as,

$$F_{\mathrm{sig}} = F_{\mathrm{On}} - F_{\mathrm{Off}},\tag{3.1}$$

where F_{On} is the F value for the "THz On" image in the measurement, and F_{Off}
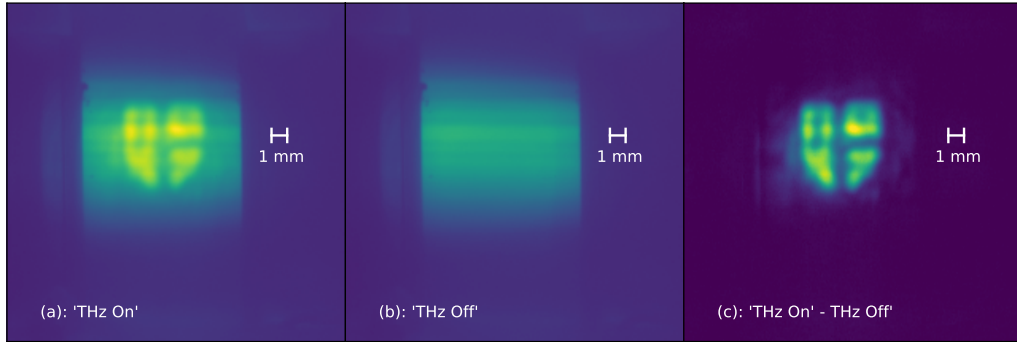
Figure 3.2: Examples of an image collected by the system in experiment 'B'. A metal mask with the Durham University logo cut out was imaged in the THz beam path. (a) An initial image taken with the THz source on, and so shows decay from the $|13D_{5/2}\rangle$ level, labelled the "THz On fluorescence". (b) An image taken with the THz source off, and so shows decay from the $|14P_{3/2}\rangle$ state, labelled "THz Off Fluoresence". (c) A resultant image from the subtraction of (b) from (a). This represents our signal, F_{sig}.

is the F value for the "Thz Off" image in the measurement.

In order to image objects in the THz regime, the THz field can be manipulated using Teflon lenses and gold-coated parabolic mirrors. In a transmission mode setup, an object that we wish to image can be placed in the imaging plane of the beam. The transmitted field can then be focused onto the position of the light sheet. Figure 3.2 shows an example of an image set from a single measurement. For this image, a metal mask with a logo cut out was placed in the imaging plane of the THz beam path, in order to demonstrate the detection of the spatial distribution of the field. The first image, (a), shows the "THz On" image, whilst the second image, (b), shows the "THz Off image", where the green fluorescence resulting from the coupling of the THz field can no longer be seen. In image (c), F_{sig} is shown - the effect of the THz is isolated most effectively in this image.

Three infra-red (IR) continuous-wave excitation lasers are used in a ladder configuration to populate the Rydberg state: $|6\mathrm{S}_{1/2}\rangle \rightarrow |6\mathrm{P}_{3/2}\rangle \rightarrow |7\mathrm{S}_{1/2}\rangle \rightarrow$

$|14\mathrm{P}_{3/2}\rangle$, at wavelengths 852 nm, 1470 nm and 843 nm respectively. This is in contrast to a more conventional two-step Rydberg excitation scheme, like those found in [75; 43], typically consisting of an IR D-line laser and a shorter wavelength Rydberg laser. The three step process provides several benefits: it requires only IR lasers, that are typically cheaper, more readily available and require less maintenance than a frequency doubled laser; the transitions have larger transition dipole moments, and thus less power is required per laser; and when imaging visible fluorescence, the IR lasers can be filtered out and do not obscure the image signal. This is because in a two step scheme, the Rydberg excitation laser would typically be of similar optical wavelength to the decay that we image. We also gain access to different upper levels in the three step scheme by selection rules, meaning we can couple a P and a D state with the THz field, rather than a laser field. A repump laser was also later implemented on the ground state D1 & D2 lines, in order to increase the number on atoms involved in the excitations.

We note that, whilst for this experiment, caesium atoms are the chosen atomic medium, any alkali metal could in principle be used with this technique. Due to the close spacing between Rydberg energy levels, different pairs of Rydberg states could in theory be chosen to image different THz frequencies. For different atoms, each species could provide a different manifold of states and transitions to choose from - each with the capability to image different THz frequencies. There are, however, caveats and trade-offs to consider, which will not be discussed here, though more detail can be found at [76]. In our case, caesium is used for the large imaging contrast of the chosen states, its relatively high number density at modest temperatures (shown in Figure 3.3), and for its general familiarity in atomic physics.
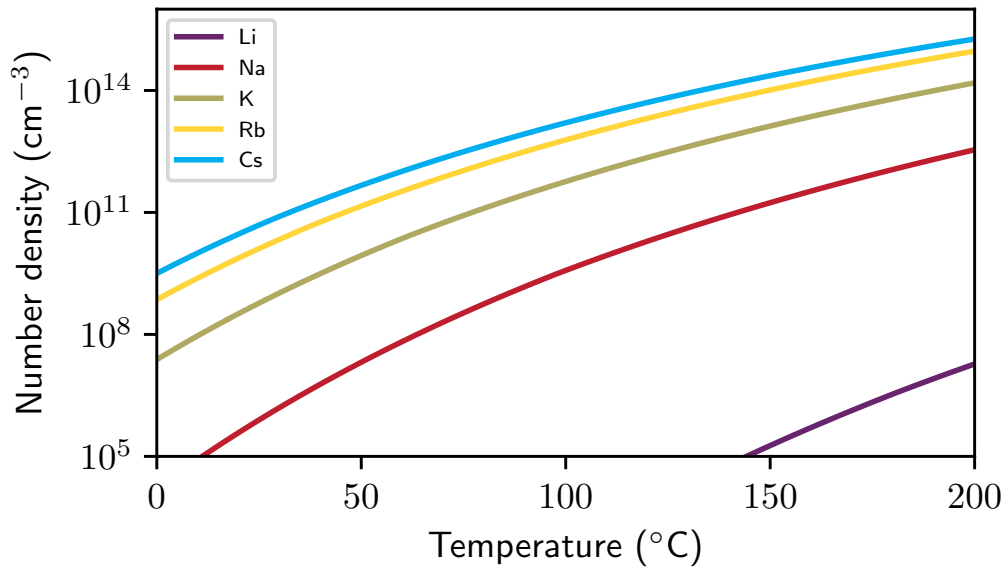
Figure 3.3: A graph showing the number density of alkali metal vapours across a typical experimental temperature range. For the majority of the experiments used in this thesis, the temperature of the cell ranged from room temperature $(20°)$ to $100°$.

3.2 Optical System

Two main setups were used to collect the data in this thesis - a "main" imaging setup and an alternate, largely similar setup used to perform non-imaging experiments and investigations. The latter will be labelled Experiment 'A', and the prior, Experiment 'B'. Experiment 'B' has been described in previous works such as [71] and [15] and so will not be discussed in as much detail, but provides the actual THz images, and is used in chapter 6. Experiment 'A' was a newer setup that provided the majority of the fluorescence results in this thesis, and so will be the main topic for discussion in this chapter. Experiment 'A' was designed such that many experimental parameters could be changed by the implementation of different optics, with minimal adjustment/realignment required, so was a more flexible setup for investigation. To simplify analysis,
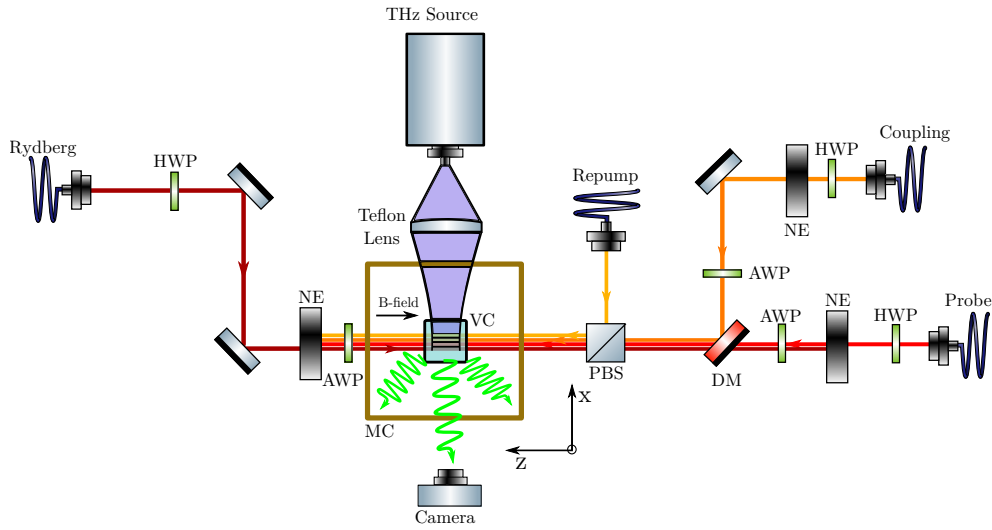
Figure 3.4: A beam path diagram for the optical bench setup of the "science area" of Experiment "A". The beams are shown separately for clarity but in reality all overlap in the same region. The probe, coupling and Rydberg lasers drive these respective transitions: $|6S_{1/2}\rangle \rightarrow |6P_{3/2}\rangle \rightarrow |7S_{1/2}\rangle \rightarrow |14P_{3/2}\rangle$, at wavelengths 852 nm, 1470 nm and 843 nm. The repump laser drives the $|6S_{1/2}, F = 3\rangle \rightarrow |6P_{3/2}\rangle$ transition at 852 nm. The probe, coupling and repump lasers are co-propagating whilst the Rydberg laser is counter-propagating for practical purposes. Components are shown not to scale. HWP: half waveplate, NE: noise eater (see section 3.5), MC: magnetic coils, PBS: polarizing beam splitter, DM: dichroic mirror, AWP: automatic waveplate (see section 3.5)

the beams in experiment 'A' were collimated through the cell, with $1/e^2$ beam widths of 1.28 mm, 1.02 mm, and 0.64 mm respectively for each excitation laser and with a repump laser beam waist of 1.04 mm. All measurements in experiment 'A' were thereby taken over the region of interest consisting of the area of the beam.

3.2.1 Lasers

3.2.1.1 Experiment 'A'

Figure 3.5 shows the overall optical bench setup of Experiment 'A'. Laser 1 (probe) consisted of a *Toptica* distributed-feedback (DFB) (#LD-0852-0150-DFB-1), powered
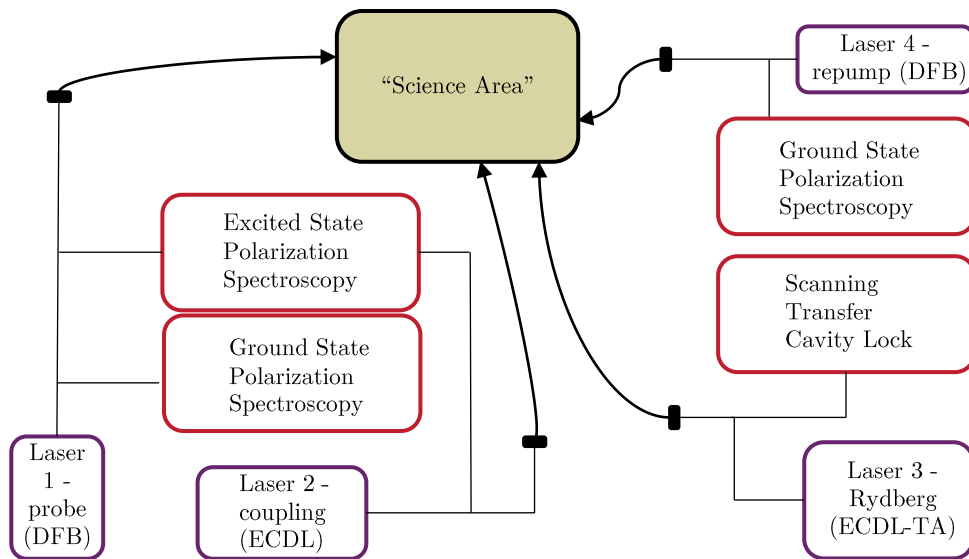
Figure 3.5: A schematic diagram of the whole optical bench for experiment 'A'. Actual optical components are not shown, but Lasers are outlined in purple, and locking systems in red, whilst the schematic beam path is outlined in black. The beam paths terminate in fibre collimators, where the beams were each coupled to the "science region" by SM-PM fibres. The "science region" is detailed further in Figure 3.4.

by a *Vescent* D2-105 Laser Controller, tuned to Cs D2 transition (852 nm), with a narrow linewidth ($\approx$ 100 kHz). This produced $\approx$ 60 mW with a mode hop free thermal tuning range of many 100s GHz. The D2-105 controller allowed for low-noise control of the laser current and temperature via the lasers integrated thermo-electric cooler (TEC) and thermistor - an external voltage from a *TTi* TG320 function generator could be input in order to scan the current and thus the frequency whilst remaining single mode. The beam divergence from the diode was 6° and 18° in the vertical and horizontal axes respectively, so a lens on an attached cage mount collimated the beam sufficiently into an elliptical beam. This could then be made into an approximately gaussian beam by focussing the beam past an aperture to clip the edges, at the expense of some power being lost. This was done in the polarization spectroscopy arm of the setup. A *Linos* FI-850-5SV 38 dB optical isolator was also used on the output

in order to prevent back-reflections into the diode that could cause optical instabilities.

Laser 2 (coupling) was a commercial *Toptica* DL100, operating at 1470 nm, controlled by the matching commercial *Toptica* DLC110 Laser Controller, with a linewidth of the order of ≈ 100 kHz. This was an external cavity diode laser (ECDL) in a Littrow design that could produce ≈ 30 mW of power. The SC110 module for the DLC110 allowed for the frequency to be scanned by applying a voltage to the piezoelectric actuator attached to the diffraction grating, providing a tilt that could finely adjust the frequency. By appropriately setting a 'feed-forward' coefficient on the front panel to coincidentally scan the current, a mode hop free tuning range of many GHz could be achieved. Internal anamorphic prisms to shape the beam and an optical isolator meant the free space output could be efficiently used without additional optics.

Laser 3 (Rydberg) was a commercial *Toptica* TA100 system, consisting of an internal DL100 (#LD-0850-0050-AR-4) ECDL seed laser, fed into a tapered amplifier (TA) to amplify the optical power output. This was re-tuned from the design wavelength of 852 nm, down to 843 nm, at the expense of some efficiency, but could still produce of order ≈ 250 mW. This was also controlled by a *Toptica* DLC110, and scanned in the same way as Laser 2, with a similar mode hop free tuning range. An internal optical isolator sufficiently prevented back-reflections, and an aperture on the free space output clipped the outer elliptical portion of the TA output beam.

Laser 4 (repump) was another *Toptica* DFB laser (#LD-0852-0150-DFB-1) at 852 nm, set up in a similar manner to laser 1, with a 35 dB *Thorlabs* optical isolator (IO-5-850-VLP) on the output, and a pair of anamorphic prisms (*Thorlabs* PS871-B) to circularize the beam. The current supply for this diode was

provided by a *Thorlabs* LDC202C laser diode current controller, and the temperature was stabilised using a *Wavelength Electronics* MPT5000 5A temperature controller. A bespoke cable was designed and built, in order to more easily interface with these equipment and allow the laser to be portable. The 8 pins for the laser circuit were connected to a 15 Pin D-sub connector. This 15 Pin connector split into two cables, designed to match up with the current controller, and that specific temperature controller. There was also a breakout box with BNC connectors, to monitor the temperature, temperature setpoint, and input a modulation to the temperature.

3.2.1.2 Experiment 'B'

In experiment 'B', the atomic level scheme was identical to 'A', but different lasers were used.. Lasers 1 and 2 were commercial *Toptica* DL100, and DLPro ECDLs respectively. Laser 3 was a Moglabs ECDL, in a different configuration, controlled by a Mogbox diode laser controlled. The Mogbox laser controller contained its own proportional-integral-differential (PID) feedback electronics, with the ability to turn a 'fast' and 'slow' lock on independently.

Laser 4 was an *MSquared* Titanium:Sapphire laser, seeded by an Equinox pump laser. This was controlled via an ethernet connection to an Icebloc, from a laptop. In combination with a *High Finesse* WS-7 wavemeter, the wavelength could be tuned with the SolsTis control panel accurately within 0.0001 nm. The SolsTis also had an internal etalon lock that would keep the frequency stable once tuned - this made it easy to change between the D1 line and D2 caesium lines for the repump laser using the automatic software driven wavelength selector. Because it was capable of very high output powers ($\simeq 10$ W), this laser was kept on a separate interlocked optical bench, and fibre coupled into the

main experiment, via a fibre combiner (*Thorlabs* PFC850A) with laser 1.

3.2.2 Frequency Stabilisation

The bulk of the optical setup in both experiments was largely designed for frequency stabilising each excitation laser to its respective atomic transition. Lasers 1 and 2 used the same locking signal generation method in both setups, and Laser 3 used a different approach in each setup, which is discussed in greater detail in Chapter 4. The first, second and third step in the ladder scheme will be referred to as the probe, coupling and Rydberg lasers/transitions respectively from hereon.

The probe frequency stabilization scheme utilized ground state polarization spectroscopy [77; 78] to generate a dispersive locking signal. This involves using a pump-probe setup, with a circularly polarized pump beam to transfer population across the m_F states, in order to induce a birefringence in the vapour, which translates into a dispersive signal when orthogonal polarizations are incident on a pair of differencing photo-diode (DPD)s. The oscilloscope trace for this signal is shown in Figure 3.6(a), aswell as the corresponding pump-probe signal obtained by blocking one of the ports on the DPD. This signal was fed into a home built PID circuit, which feeds back to the current on the D2-105 Laser Controller to frequency stabilise to the $|6\mathrm{S}_{1/2}, \mathrm{F} = 4\rangle \rightarrow$ $|6\mathrm{P}_{3/2}, \mathrm{F'} = 5\rangle$ transition. This closed transition should excite population most efficiently, as it has the largest Clebsch-Gordon coefficient.

The coupling step laser was frequency stabilised using an excited state polarization spectroscopy scheme [79]. This utilizes similar physics to the ground state technique, but uses an overlapping circularly polarized ground state beam in order to pump population into an m_F state that can excite in only one sense

of circular polarization, thus inducing a birefringence in the vapour. The probe in this case is a linearly polarised counter-propagating coupling beam, which is absorbed stepwise on the second transition. Given that the linear light can be decomposed into left and right circular components which drive different sublevel transitions, one of the components will be absorbed preferentially to the other. Therefore, when the orthogonal components are separated on a polarising beam-splitter (PBS) and differenced on a DPD, a dispersive signal is generated - the resulting oscilloscope trace from the DPD is show in Figure 3.6b. This signal was fed back into the PID110 module of the DLC110 laser controller, which internally generates a control signal that communciates via the backplane of the laser controller, to the SC110 module, which outputs to the piezo actuator of the ECDL. The nature of this locking scheme means that the setpoint of the second laser is dependent on the lockpoint of the first laser, outside of the acquisition range of the lock.

For the Rydberg laser, two different stabilization schemes based on a Fabry-Perot etalon were used in either experiment. An extended discussion and comparison of these schemes is given in Chapter 4, so it is suffice to say here that experiment 'A' used a *Thorlabs* SA200-8B cavity with a scanning transfer cavity locking scheme [80], and experiment 'B' used a traditional Pound-Drever-Hall (PDH) [81] lock with additional tunable sidebands [82], using a *Stable Lasers Sytems* ultra low expansion, high finesse cavity.

3.3 Terahertz Sources

To generate our THz field, two different commercial THz sources were used. Both were made by *Virginia Diodes*, each consisting of an amplifier multiplier
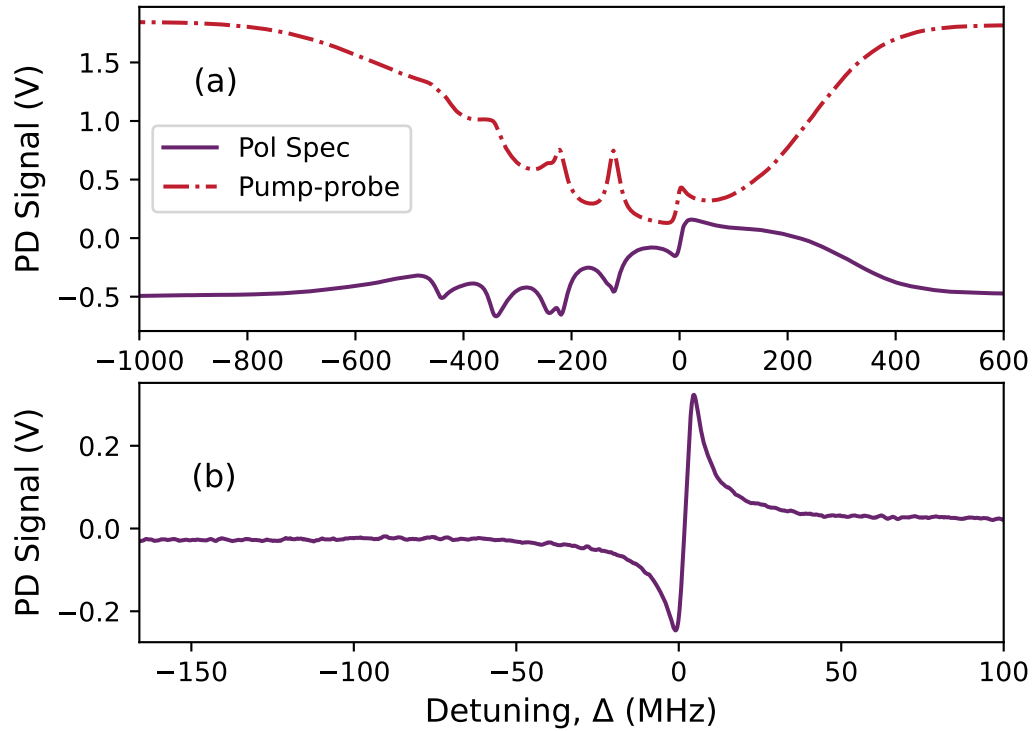
Figure 3.6: (a) The oscilloscope trace for the ground state polarization spectroscopy locking signal. The purple trace shows the actual signal used for locking, and the red dotted trace shows the associated pump-probe spectroscopy obtained by blocking one port of the DPD. The frequency axis is determined from the hyperfine features, and centred on the $|6S_{1/2}, F = 4\rangle \rightarrow |6P_{3/2}, F' = 5\rangle$ closed transition. (b) The oscilloscope trace for the excited state polarization spectroscopy locking signal. The frequency axis here is determined using a Fabry-Perot etalon for a frequency reference, and is centred on the lockpoint, at the centre of the dispersive signal, corresponding to the $|6P_{3/2}, F = 5\rangle \rightarrow |7S_{1/2}, F' = 4\rangle$ transition.

chain, seeded by a microwave source, that multiplies a input RF seed frequency up to a THz frequency. Both sources were centred on the 550 GHz transition: an AMC-331 (source "A"), that had a tuning range of 500-750 GHz, and an AMC 701 (source "B") with a narrower tuning range of 540-560 GHz, but a higher output power. The output power varies across the frequency range, but at 550 GHz, the AMC-331 output ≈ 20 μW at max power, and the newer AMC 701 output ≈ 4 mW. For measurements performed after it was acquired, the AMC 701 was used, which enabled access to a higher power regime of behaviour.
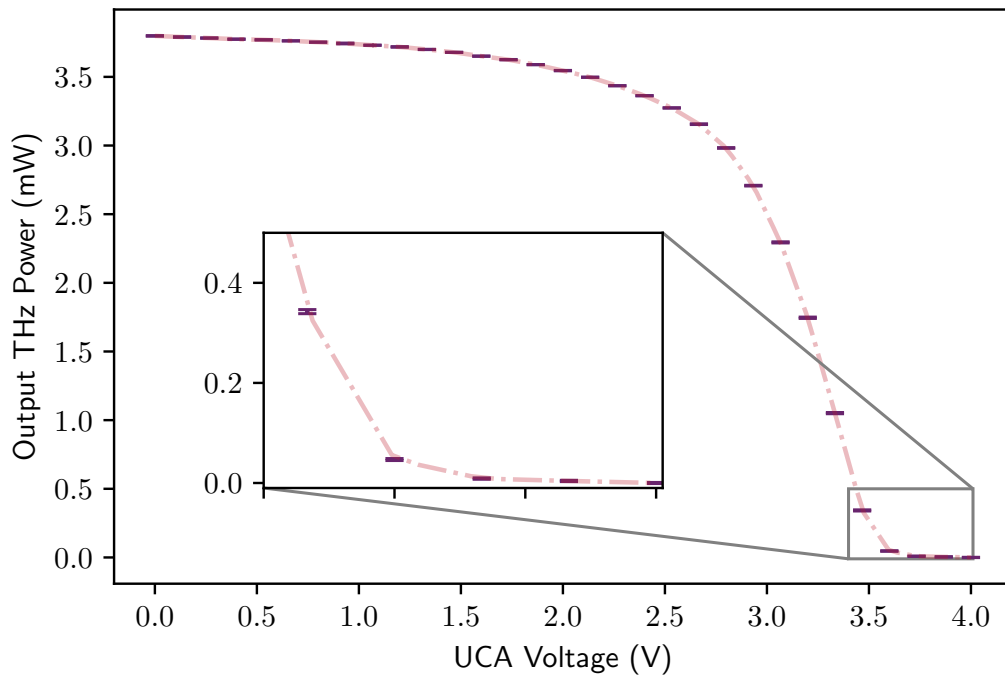
Figure 3.7: The user controlled attenuation power profile for the AMC 701 source. This data was acquired by coupling the source directly to the PM5B powermeter to measure the power with the maximum efficiency, and varying the voltage input to the source UCA port with an *NI* USB-6008. The dotted line is a guide for the eye. The errorbars represent the standard error on the mean of 5 repeat measurements.

Both could be seeded with either a *Windfreak Technologies* SynthHD Pro, or an analogue *Hewlett Packard* 8672A Synthesized Signal Generator. The THz frequency could be varied by varying the micro-wave (MW) seed frequency, accounting for a multiplication factor unique to the source; for source "A", being 54, and for source "B", being 36. Both output beams were free-space coupled with diagonal horns, with full 3 dB beamwidths of 10° each, and a Gaussian beam content of 84% [83]. The power could be varied with an external voltage via a user controlled attenuation port. The input voltage range was 0-5 V, across which the output power had a non-linear response, shown for source 'B' in figure 3.7. Across all measurements, in order to acquire a "THz Off" image, a voltage of 5 V was applied to the source to fully attenuate the output power.

A *VDI* Erickson PM5B Power Meter could be used to measure the THz beam power. This was a calorimeter-style measurement device, that was used to provide a reference calibration for the power at varying UCA voltages, by directly coupling the power meter head to the THz source.

Due to the divergent nature of the beam from the source, a Teflon lens was always used after the horn in order to collimate the beam to a $1/e^2$ beam waist of ≈ 11 mm. For imaging, we could also make use of two commercial lenses from *i2s*, that functioned as objective lenses with a focal point on the imaging plane, with either 1x or 4x magnification.

3.4   Data Acquisition

The primary data collected for this thesis was fluorescence data, F_{sig}, as defined in eqn. 3.1. This was collected by two main methods: via a CMOS camera, and via a spectrometer to collect spectral information. In the case of spectral data, the fluorescence value, F, takes the form of counts from the spectrometer.

In Experiment 'A', an *Imaging Source* DMK 72AUC02 USB 2.0 monochrome CMOS sensor was used. This camera has a resolution of 2592x1944, with a 2.2 μm pixel size, and a minimum exposure time of 100 μs. A Steinheil triplet lens (TRS254-040-A-ML) attached to the camera formed an image of the position of the overlap region in the cell, at the position of the sensor. A narrow notch filter at 535 nm $\pm$ 30 nm (*Newport* HPM535-30) with average transmission $> 90\%$, was also placed inside the lens tube to filter out the laser light, and unwanted fluorescence. The native 'IC Capture' programme was used to view the output images in first order for aligning the camera, and for a visible reference, to adjust exposure times etc. When taking data, a Python wrapper was

used in combination with the `ctypes` package in order to call C# to save image data directly into Python `NumPy` [84] arrays. Processing could then be done at the same time as data collection - this is where the 'region of interest' covering the overlap region of the cell was clipped from the entire image, and this was averaged to provide a single pixel value of the fluorescence for each image.

In Experiment 'B', the camera used was an *Andor* iXon 888 EMCCD. This could be used with the software *MicroManager* in order to get a live feed from the camera, and take snapshots when needed. Otherwise, to automate data collection, the `pyAndor` package was used to save images directly into Python.

The spectrometer could be used in addition to or instead of the camera. An *Ocean Insight* FLAME-T-VIS-NIR-ES spectrometer was used, with a grating consisting of 600 lines blazed at 500 nm. This could provide a spectral resolution of up to 0.1 nm, with a minimum integration time of 3.8 ms. Fluorescence could be gathered via an SMA fibre at the edge of the cell to be read via USB from the *Ocean Insight* Spectrometry Software. Figure 3.8 shows an example of a measurement using the spectrometer.

Other data was important to monitor during an experimental run, in order to isolate the effects of the independent variable being investigated from other variables. These included the temperature of the cell, the frequency setpoints of the 3 excitation lasers and laser powers. As such, where possible, data on these variable parameters was collected simultaneously in data runs, which allowed for post-run troubleshooting or analysis. For example, a thermocouple probe monitored the temperature at the top of the cell, which was fed back to the computer using an *NI* USB-TC01. This could be directly tracked and saved in Python using the `NI-daqmx` package.

Traces such as locking signals and cavity peaks were monitored in real time,
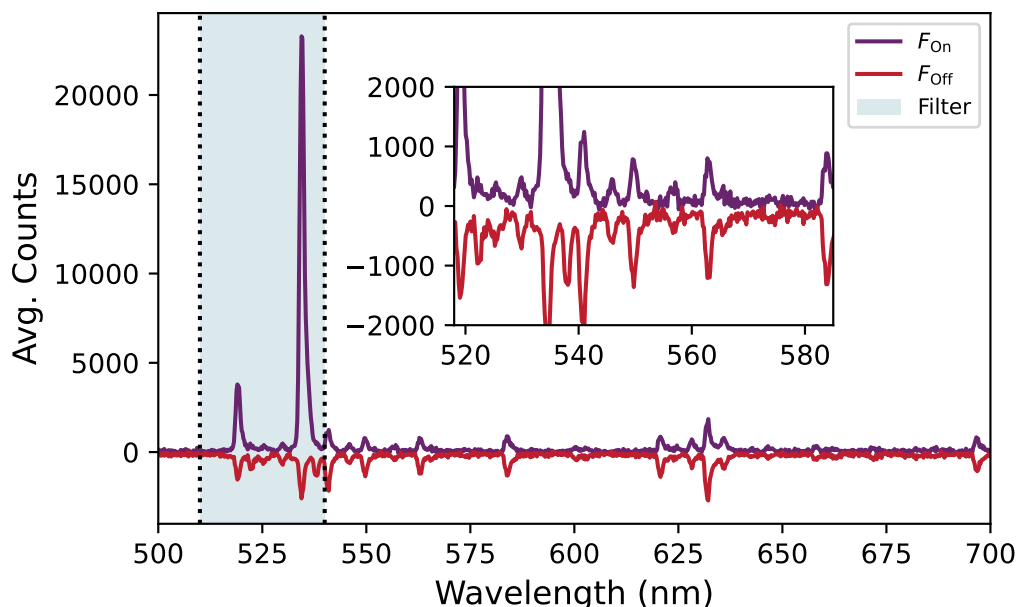
Figure 3.8: An example of spectral data from the spectrometer, where each peak corresponds to a decay line from the atoms. The purple trace shows the fluorescence for a "THz On" measurement, with a strong peak at 535 nm. The red trace is inverted, and shows the "THz Off" fluorescence for comparison - the main decay line is much weaker. The secondary peak at 520 nm is a result of collisional transfer to the other j state from the upper Rydberg level. The remaining decay peaks can largely be traced to decay lines by a Monte-Carlo model. The shaded region represents the transmission region of the bandpass filter used, with > 90% transmission inside of this region and < 1% transmission outside. The inset shows a zoomed in section of the spectrum. A background spectrum with no atomic fluorescence is subtracted from both spectra. This data was acquired with a 500 ms integration time.

and could be tracked during a data run on the computer by USB or ethernet connection. The two main scopes used were a *Tektronix* MDO4054C and a *Rhode & Schwarz* RTO1014. The RTO1014 was connected to the local network and, using the `RsIntrument` [85] package, it could be controlled, and data acquired directly from the scope into Python. The MDO40454C was connected via USB to the computer, and simply used `PyVISA` to connect with Python and read traces directly from the scope.

Laser beam powers were generally measured with optical power meters (*Thor-*
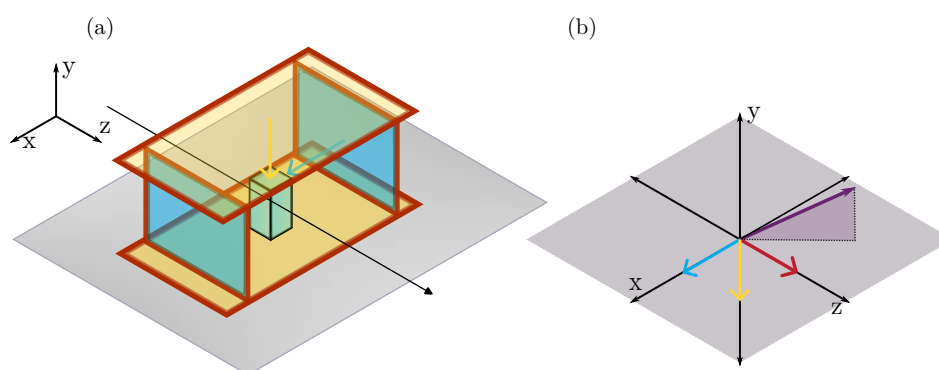
Figure 3.9: (a) Diagram to show the setup of the magnetic coils around the vapour cell. The laser direction along the z axis is indicated by the black arrow, whilst the blue and yellow indicate the direction of the fields generated by each pair of coils. (b) Vector diagram to illustrate the cancellation of the Earth's magnetic field in the x and y axes. The original field is shown in purple, whilst the resultant vector from the addition of all 3 fields is shown in red, along the z axis. This allows for the definition of a quantization axis.

labs PM100D or PM101R with S121C and S122C heads), which could be connected via USB to the computer for automatic read out. The custom package ThorlabsPM100 could then be used to read out powers directly, or the native Optical Power Monitor software could be used for a GUI interface. Beam powers could alternatively be read out by a photodiode (e.g. PDA10A2) whose signal would be fed into either a scope for readout there, or into an NI USB-6008 input port for a direct voltage measurement.

3.5 Experimental Control

In order to investigate the optimum conditions for imaging, careful control was required over the various parameters of the experiment. This section will describe the equipment and processes used for this.

Around the cell, 4 magnetic shimcoils were set up, in order to cancel the Earth's magnetic field and create a region of approximate zero field in the x and y axes,

at the position of the centre of the cell. This is shown in figure 3.9. These were homemade shimcoils consisting of a $\approx$ 20 cm x 20 cm Tufnol loop housing, with .5 mm copper wire wound around it, with $\approx$ 40 windings and sealed with strong tape. They formed two pairs of Helmholtz coils, with each pair connected in series, in order to create an approximately uniform field at the position of the cell, that opposed the vector of the Earth's magnetic field on that axis. The resulting magnetic field pointed in the positive z-direction, with a magnitude of around 100 mG. The field was characterized in each axis using a gaussmeter and eventually its overall direction confirmed with a compass. This allowed us to define a quantization axis with respect to a polarization angle along the z-axis in order to control the transitions that were allowed from each excitation laser. This will be important later in Section 5.2.

In general, wherever a voltage was required to control an element of the experiment, a *National Instruments* USB-6008 or USB-6001 multifunction I/O DAQ device was used to generate it. These lightweight cards could be connected to a computer via USB, and controlled with the native *NI* Device Manager, or through Python using the official `NI-daqmx` [86] package, in combination with `PyVisa` [87]. The devices feature several analog input and output ports, that could be connected to BNC/SMA cables with screw terminals in order to interface with other equipment.

For each beam, prior to the coils, commercial noise eaters (*Thorlabs* NEL03A/M / NEL04A/M) were used to stabilize the power in each beam into the cell. These devices accepted linearly polarized light, and applied a servo loop to stabilize the power output to a level below the input power. They consist of a liquid crystal retarding device, a polarizer and a beamsplitter. The liquid crystal retarder rotates the polarization of the light to an angle dependent on the voltage

applied to the liquid crystals - this in combination with a fixed polarizer translates the polarization change into a change of transmitted power. A beamsplitter then picks off a portion of the light onto a photodiode to convert it into a voltage, which is compared to a desired level set by a potentiometer, and the resulting control signal is fed back as a voltage to the liquid crystal retarder as a closed loop system to stabilize the output power. One benefit of this equipment was the ability to set the desired power level remotely via an external applied voltage. This was used extensively in Section 6.1.1 to change the power into the cell from each beam with computer control via an NI USB-6008 DAQ box. Another incidental benefit is that the output light had a well defined polarization.

An additional level of control was gained through use of automatic rotation mounts (*Thorlabs* PRM1/MZ8), in combination with the *Thorlabs* K-Cube DC servo motor controllers (KDC101). By mounting quarter waveplates inside these rotations mounts, and placing them as the last optic before the cell (where possible) the polarization of the light could be carefully controlled. These are labelled in figure 3.4 as automatic waveplates (AWP). The motor controllers could be interfaced via USB to the computer, and controlled with the native programme *Kinesis*, or with a custom Python package, such as `thorlabs-apt` [88] or `thorlabs-apt-device` [89]. This allowed for the remote setting of a waveplate angle in order to control the polarization of the beam.

The 10 mm x 10 mm cubic cell was housed in a homemade mount machined from Teflon, which was attached to a metal mount for bolting to the optical table. The mount was designed to fit two 24 W, 20 mm x 20 mm resistive ceramic heaters (*Thorlabs* HT24S) near the top of the cell reservoir, which were powered in parallel by an adjustable power supply to allow for temperature control of

the cell, to change the number density of the vapour.

A temperature stabilization system was also implemented using an Arduino Mega, along with a repurposed 3D printing board. By reading the temperature with a thermocouple, the feedback loop could correct for long term drifts in the temperature by adjusting the output voltage on the power supply. The adapted software, *Repetier*, is designed to control parameters for a 3D printer, including the temperature of the printing heads via a PID loop. By programming an Arduino Mega with the Repetier software, and isolating the temperature control element, we could interface with the software in order to adjust PID gain settings, read out temperature, change the setpoint and engage the lock. Custom Python code also enabled performing these tasks through Python, using the package `PySerial`, so that the temperature could be changed automatically during a data run, by changing the setpoint, for example.

3.6   Conclusion

This chapter has provided a description of the atomic system and the working principle that is at the core of the THz imaging technique used in this thesis. The experimental implementation of this optical setup has been set out, including the geometry of the beams, which will be of use later. The main methods for data collection have been outlined, mainly through collection of fluorescence. The elements required for control of the experimental parameters that will be investigated have been introduced. An important feature is the ability for almost all parameters to be controlled remotely via the computer, so that measurements can be repeated easily to build up better statistics and to avoid introducing noise through manual adjustments.

Rydberg Laser Frequency Stabilisation

4.1 Introduction

As discussed in the previous section, the probe and coupling lasers in the ladder system were frequency stabilised to error signals generated from atomic references, based on polarisation spectroscopy and excited state polarisation spectroscopy, respectively. The choice of reference for the Rydberg laser was not as obvious - an EIT lock [90] could be used, but we ideally wanted to use as little power as possible, due to the power requirements of the transition. Instead, cavity references were used to generate error signals that could be tuned to arbitrary frequencies - a Pound-Drever-Hall [81] lock, that was implemented in Experiment 'B', and a scanning transfer cavity lock [80] that was implemented in Experiment 'A'. The different pros and cons of both of these methods will be discussed in this chapter, as well as basic introductions to the theory of each, and an account of how they were implemented into our setups. An attempt to characterise the effectiveness of each lock in stabilising our meas-

urement parameter, F_{sig}, will be made, but detailed analysis of frequency stability, with methods such as beat frequency measurements, will not be made. To preface the discussion of the implementation of these locking methods, we will first briefly recap the basics of control theory needed to understand the PID controllers used to implement the frequency stabilisation, and the theory of Fabry-Perot cavities, that will help in understanding both systems.

4.1.1 Proportional-Integral-Differential Controllers

Proportional-integral-Differential (PID) controllers provide feedback mechanisms to minimise the difference between an input signal and a chosen setpoint. They are ubiquitous in modern control systems due to their simplicity, and they are the primary controllers used in implementing feedback for laser frequency stabilisation. Whilst they differ in implementation and complexity, in the most basic sense, their output control signal can be described as,

$$u(t) = K_p e(t) + K_i \int_0^t e(\tau)d\tau + K_d \frac{de(t)}{dt}, \qquad (4.1)$$

where the error signal, $e = r - y$, where r is the input signal and y is the setpoint. The controller parameters, K_p, K_i, and K_d are the proportional gain, the integral gain and the derivative gain respectively, and are tuned to values that fit a particular system. Typically, each term in 4.1 can be thought of in basic terms as having a different role - in the first term, the proportional action provides instantaneous feedback to a change in the input. The integral term, proportional to the accumulated error, provides a slow feedback response to changes in the input, whilst the derivative term, proportional to the rate of change of the error, provides a fast response, or even a 'predictive' response to changes in the input.

When applying these systems to laser frequency stabilisation, an error signal derived from a frequency reference such as an atomic or cavity resonance is normally fed into a PID controller, whose output feeds back to the laser piezo or current, in order to adjust the frequency. The process of achieving good frequency stabilisation therefore consists of firstly generating a reliable error signal, and then optimising the controller parameters until the error signal is minimised. Useful references on this topic can be found at [91] and [92].

4.1.2 Fabry Perot Cavities

A Fabry Perot cavity is an optical resonator consisting of two or more mirrors that create a build up of light by reflecting it back and forth. Light that enters the cavity can travel many round trips back and forth, and the build up of many waves interferes with each other. Constructive interference leads to the formation of effective standing waves, when the optical path length is equal to an integer multiple of a half-wavelength, $q\lambda/2, q \in \mathbb{N}$, and destructive interference eliminates light of any other wavelength. By this mechanism, a cavity may act as a frequency discriminator - due to the fact light is only supported, and thus transmitted at certain frequencies, when the light is resonant with the cavity modes.

For a linear resonator consisting of two spherical mirrors, the supported frequencies for a Guassian input beam can be described by a solution to the paraxial wave equation [93], with suitable boundary conditions like,

$$\nu_{qml} = \frac{c}{2nL}\Big[q + \frac{1}{\pi}(m + l + 1)\cos^{-1}\sqrt{g_1 g_2}\Big], \qquad (4.2)$$

where q is the longitudinal mode number, m and l are transverse mode numbers, L is the length of the cavity, n is the refractive index of the medium inside

the cavity and $g_{1,2}$ are stability parameters, defined by

$$g_{1,2} \equiv 1 - \frac{L}{R_{1,2}}, \tag{4.3}$$

where $R_{1,2}$ are the radii of curvature of the mirrors. These g-parameters fulfill the condition $0 \leq g_1 g_2 \leq 1$ for a stable cavity [94]. The modes supported at these frequencies are transverse Guassian, or Hermite-Guassian modes, labelled by TEM_{ml}. The fundamental mode (TEM_{00}, with $m = l = 0$), is a Guassian beam, and under perfect alignment and mode matching conditions, is the only mode supported by the cavity. The frequency spacing between two adjacent longitudinal modes is known as the free spectral range, defined by,

$$\nu_{\text{fsr}} = \nu_{100} - \nu_{000} = \frac{c}{2nL}. \tag{4.4}$$

The width (full width half maximum (FWHM)) of the transmission peaks, $\delta\nu$ is characterised by the *finesse* of the cavity, $\mathscr{F} = \frac{\nu_{\text{fsr}}}{\delta\nu}$, which is determined by the geometry of the cavity. For a cavity with two mirrors of equal reflectivity ($r = r_1 = r_2$),

$$\mathscr{F} = \frac{\pi\sqrt{r}}{1 - r^2}. \tag{4.5}$$

Figure 4.1 shows an example of some calculated cavity transmission peaks, with the free spectral range, and width of the peaks labelled. For a fixed free spectral range, cavities with larger finesse have more narrow transmission peaks.

A special case of cavity, where $R_1 = R_2 = L$, is known as a confocal cavity. For a confocal cavity, consisting of two identical mirrors, separated by the radius of curvature of the mirrors, eqn. 4.2 is reduced, and the resonance frequencies become,

$$\nu_{qmn} = \frac{c}{2nL}\Big[q + \frac{1}{2}(m + n + 1)\Big]. \tag{4.6}$$

In a confocal cavity, without perfect alignment and mode matching, eqn 4.6 means that the modal spectrum consists of either degenerate modes (e.g TEM_{0-11}
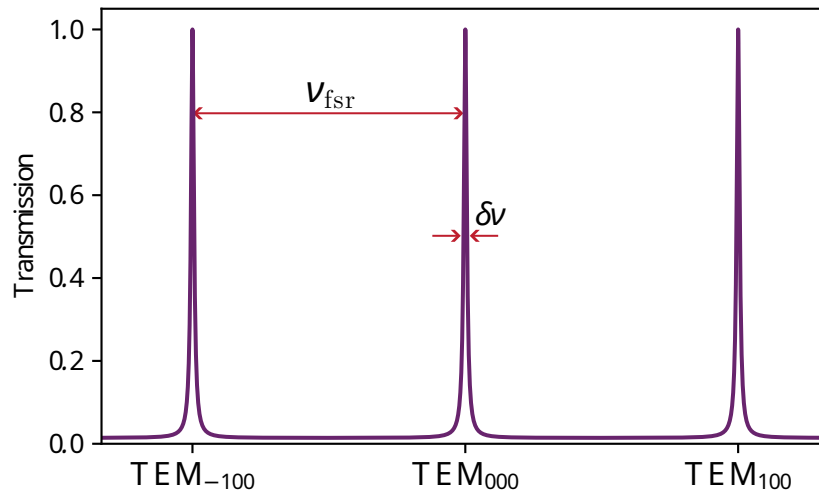
Figure 4.1: Example Fabry-Perot etalon transmission spectrum, with mirror reflectivites $r_1 = r_2 = 0.95$. Each peak represents a fundamental mode, and the frequency between them is known as the free spectral range. The finesse is defined by the ratio of the free spectral range to the width of the peaks.

& TEM_{01-1}) or modes separated by $\frac{c}{4nL}$. For this reason,

$$\nu_{\text{fsr,conf}} = \frac{c}{4nL}. \tag{4.7}$$

The *Thorlabs* SA200-8B cavity used in section 4.3 was an example of a confocal cavity.

4.2 Pound-Drever-Hall Technique

A leading method for frequency stabilising a laser to a cavity is the PDH technique. Developed in [81], this technique uses the reflected light from a cavity, with a "lock-in style" measurement to generate an error signal that locks to the top of a peak. Before this technique was introduced, typically side-of-peak locking methods were used. These techniques chose a setpoint in the middle of the side of a peak, and used the fact that a change in frequency from this point corresponded to a change in transmitted intensity of opposite sign depending on the sign of the frequency change, to generate an error signal. A

main drawback of this technique is that a frequency change could not be distinguished from a change in the laser intensity, so incorrect feedback may be applied to the frequency.

The PDH technique circumvents this by introducing a modulation on the phase of the input beam, that manifests in frequency sidebands (see section 4.2.1.1). The cavity then acts as a frequency discriminator, that around resonance, converts a frequency-dependent phase difference into an amplitude difference that can be detected on a photodiode. This method allows for high bandwidth frequency stabilisation, to the point of linewidth narrowing (with a sufficiently stable cavity). As such, it has become the standard for frequency stabilisation using cavities. It can also be modified slightly, to allow for a tunable setpoint, anywhere within the free spectral range of the cavity. This is achieved by doubly modulating the input light [82], with a much higher frequency, that determines the centre point of the locking discriminant. As our Rydberg laser required locking to an arbitrary frequency relative to a given cavity mode, we sought to implement this stabilisation scheme in experiment 'B', the main imaging system.

The following section will discuss the conceptual / theoretical basis for the technique, largely following the explanation of the paramount reference on the topic, *Black, 2001* [95]. Then, we will discuss the implementation of the setup in Experiment 'A', followed by some brief results to demonstrate the improved stability of the experiment as a result. Other useful references throughout include [60; 96; 97; 98; 99].

4.2.1 Theory

4.2.1.1 Standard PDH Technique

The standard PDH technique involves phase modulating the initial beam incident on the cavity. The electric field of the modulated incident light can be described with the form

$$E = E_0 \exp(i(\omega_\mathrm{c} t + \beta \sin \Omega t)), \tag{4.8}$$

where ω_c is the angular frequency of the incoming light, β is the modulation amplitude (or depth), and Ω is the angular frequency of the modulation. This can be expanded to first order using a Jacobi-Anger expansion and a property of Bessel functions of the first kind ($J_{-n}(x) = (-1)^n J_n(x)$):

$$e^{i(\omega_\mathrm{c} t + \beta \sin \Omega t)} = e^{i\omega_\mathrm{c} t}[J_0(\beta) + J_{-1}(\beta)e^{-i\Omega t} + J_1(\beta)e^{i\Omega t}] \tag{4.9}$$

$$\implies E/E_0 = J_0(\beta)e^{i\omega_\mathrm{c} t} - J_1(\beta)e^{i(\omega_\mathrm{c}-\Omega)t} + J_1(\beta)e^{i(\omega_\mathrm{c}+\Omega)t} \tag{4.10}$$

This modulation therefore, in effect, splits the beam into 3 distinct frequencies: a carrier at frequency $\omega = \omega_\mathrm{c}$ and two sidebands at frequency $\omega = \omega_\mathrm{c} \pm \Omega$. Without a cavity reference, a photodetector would not pick up an intensity modulation from this light, as the sidebands, of opposite phase, cancel each other out. The cavity reference acts to introduce a phase difference, that is different either side of resonance, that disables this destructive interference. With a large enough modulation frequency, Ω, when the carrier is near a cavity mode resonance, the sidebands will be totally reflected. Assuming a perfectly impedence matched cavity, if the carrier is perfectly on resonance, then the immediately reflected beam and the leakage beam from the cavity will be 180 degrees out of phase, and will cancel each other out. If the carrier is only near resonance, a proportion of the carrier signal will be reflected, due to the phase

mismatch between the leakage and initially reflected fields. The phase of this reflected beam gives us a measure for what side of resonance we are on. Each sideband also has a definite phase relation to incident and reflected carrier, meaning that when the light is reflected from the cavity, interference occurs between the reflected carrier interferes with the reflected sidebands, giving a beating intensity modulation at frequency Ω, which we will see in equation 4.16.

This intensity modulation can be picked up by a photodiode, and demodulated through a mixer to generate a frequency discriminant, centred on the cavity resonance. This frequency discriminant signal differs in sign either side of the cavity resonance, which can be exploited by the PID controller, to adjust the signal to zero, and thus keep the laser frequency stable at that zero crossing.

We can model this using the *reflection coefficient*, which (calculated for a symmetric cavity with mirrors each with reflection coefficient r, and a FSR as defined in equation 4.4) is defined as:

$$F(\omega) = \frac{r(\exp(i\omega') - 1)}{1 - r^2 \exp(i\omega')}, \tag{4.11}$$

where $\omega' = \frac{\omega}{\Delta\nu_{\text{fsr}}}$ (the angular frequency in units of free spectral ranges). We can linearly multiply each component of the beam by the reflection coefficient at its specific frequency to acquire the reflected field:

$$E_{\text{ref}} = E_0 [F(\omega_{\text{c}}) J_0(\beta) e^{i\omega_{\text{c}} t}$$
$$- F(\omega_{\text{c}} - \Omega) J_1(\beta) e^{i(\omega_{\text{c}} - \Omega)t} \tag{4.12}$$
$$+ F(\omega_{\text{c}} + \Omega) J_1(\beta) e^{i(\omega_{\text{c}} + \Omega)t}]$$

We cannot directly measure the electric field, but we can detect the power output on a photodiode; $P_{\text{ref}} \propto |E_{\text{ref}}|^2$. If we take $P_0 = |E_0|^2$ to be the total power

of the beam, and assume that the power in the carrier is

$$P_{\mathrm{c}} = J_0^2(\beta) P_0 \qquad (4.13)$$

and the power in each first order sideband is

$$P_{\mathrm{s}} = J_1^2(\beta) P_0, \qquad (4.14)$$

then we can calculate the reflected beam power, P_{ref}. It can be useful for convenience to define a function,

$$\alpha(\omega) = F(\omega) F^*(\omega + \Omega) - F^*(\omega) F(\omega - \Omega), \qquad (4.15)$$

and take α to mean $\alpha(\omega_{\mathrm{c}})$ for clarity. With this notation, we can calculate the reflected power:

$$\begin{aligned} P_{\mathrm{ref}} = {}& P_{\mathrm{c}} |F(\omega_{\mathrm{c}})|^2 + P_{\mathrm{s}} [|F(\omega_{\mathrm{c}} + \Omega)|^2 + |F(\omega_{\mathrm{c}} - \Omega)|^2] \\ & + 2\sqrt{P_c P_s} [\mathrm{Re}(\alpha) \cos \Omega t + \mathrm{Im}(\alpha) \sin \Omega t] \\ & + (2\Omega \text{ terms}). \qquad (4.16) \end{aligned}$$

The sine and cosine terms are due to the interference between the carrier and its sidebands and give rise to the beating frequency. The higher order 2Ω terms are due to the interference between the two sidebands, but this effect is minimal with a small modulation depth. At a typical modulation frequency, $\Omega/2\pi \approx$ 20 MHz, which is large compared to the cavity linewidth, α is almost purely imaginary, and so the sine term dominates, and the cosine term disappears. The remaining sine term contains the phase information we require for locking. We can use a mixer to demodulate this signal; a mixers operation is to output the product of its two inputs. We can input a voltage from the photodiode that is proportional to this power, and the initial modulation into a double balanced mixer, and we get the product of the terms, $\beta \sin \Omega t$ and $2\sqrt{P_c P_s} \mathrm{Im}(\alpha) \sin \Omega t$.

This, by the product of two sines, gives us a signal like,

$$V \propto \beta\sqrt{P_{\mathrm{c}}P_{\mathrm{s}}}\mathrm{Im}(\alpha)[1 - \cos{(2\Omega t)}], \tag{4.17}$$

meaning we can pass this through a low pass filter to extract the constant term to use as an error signal:

$$\epsilon = \beta\sqrt{P_{\mathrm{c}}P_{\mathrm{s}}}\mathrm{Im}[F(\omega_{\mathrm{c}})F^*(\omega_{\mathrm{c}} + \Omega) - F^*(\omega_{\mathrm{c}})F(\omega_{\mathrm{c}} - \Omega)]. \tag{4.18}$$

There is a caveat to this in practice however, as the modulation from the signal generator will gain a phase offset, ϕ as it travels through the wires, meaning that the dc term will gain a factor of $\cos\phi$. Near, for example, $\phi = \frac{\pi}{2}$, this will cause the signal to disappear – so it is important to adjust the phase using the signal generator to maximise the dc term's amplitude. Figure 4.4(b) shows the simulated signal as a function of detuning. The linear section near resonance is ideal for a feedback system, and can be approximated if we consider that, when near resonance, the sidebands are reflected, i.e $F(\omega_{\mathrm{c}} \pm \Omega) \approx -1$, and most of the power of the carrier is transmitted, i.e $|F(\omega_{\mathrm{c}})|^2 \approx 0$. This means that α becomes ($z - z^* = 2i\mathrm{Im}[z]$):

$$F(\omega_{\mathrm{c}})F^*(\omega_{\mathrm{c}} + \Omega) - F^*(\omega_{\mathrm{c}})F(\omega_{\mathrm{c}} - \Omega) = 2i\mathrm{Im}[F(\omega_{\mathrm{c}})] \tag{4.19}$$

If we also consider that the reflection coefficient periodically vanishes on resonance, then a small deviation from resonance, $\delta\omega'$, such that,

$$\omega' = 2\pi n + \delta\omega', n \in \mathbb{N} \tag{4.20}$$

will produce a reflection coefficient $F(\omega_{\mathrm{res}} + \delta\omega) = F(\delta\omega)$, which can be approximated, with a large enough cavity finesse, as

$$F(\delta\omega) \approx \frac{i}{\pi}\frac{\delta\omega}{\delta\nu}. \tag{4.21}$$

In the linear region near resonance, i.e. where $\delta\omega \ll \delta\nu$, these approximations can be substituted into the error signal, equation (4.18) to give,

$$\epsilon = \frac{2\beta}{\pi}\sqrt{P_\mathrm{c}P_\mathrm{s}}\frac{\delta\omega}{\delta\nu}. \tag{4.22}$$

This equation provides the linear relationship between the error and the frequency offset near resonance that a PID controller can use in a servo system. The gradient is known as the frequency discriminant, and can be used as a quantifier to the quality of an error signal.

4.2.1.2 Sideband Locking

Sideband locking [82; 100] follows much the same principles as the standard PDH method, however, instead of locking to the carrier signal, we place a sideband on resonance, and can adjust the modulation frequency that results in this sideband in order to tune the laser frequency about this point. There are two different methods to generating the extra sidebands - one through the dual sideband (DSB) locking method, and another through the electronic sideband (ESB) method. In dual sideband locking, the initial beam is modulated at two different frequencies, Ω_1 and Ω_2, which generates a carrier, ω_c, sidebands at $\omega_\mathrm{c} \pm \Omega_1$, sidebands at $\omega_\mathrm{c} \pm \Omega_2$ and sub-sidebands of those sidebands at $\omega_\mathrm{c} \pm \Omega_1 \pm \Omega_2$. Equation (4.23) shows the electric field of the initial beam in this method.

$$E_\mathrm{DSB} = \sqrt{P_0}\exp(i[\omega_\mathrm{c}t + \beta_1\sin\Omega_1 t + \beta_2\sin\Omega_2 t]) \tag{4.23}$$

Ω_1 can be changed to tune the locking point. The disadvantage of this method is that it results in a complex optical spectrum, and the dependence on various parameters can make it difficult to lock, and can introduce excess noise.

In the electronic sideband method, the signal driving the electro-optic modulator (EOM) is itself phase modulated, in the form of,

$$E_{\mathrm{ESB}} = \sqrt{P_0} \exp\{(i[\omega_{\mathrm{c}}t + \beta_1 \sin(\Omega_1 t + \beta_2 \sin \Omega_2 t)])\}, \qquad (4.24)$$

so that in the intial beam, we have a carrier of frequency ω_{c}, sidebands at $\omega_{\mathrm{c}} \pm \Omega_1$, and sub-sidebands of $\omega_{\mathrm{c}} \pm \Omega_1 \pm \Omega_2$; we no longer generate the sidebands at $\omega_{\mathrm{c}} \pm \Omega_2$ (Note that the modulation at frequency Ω_2 appears as a phase modulating term inside the modulation at frequency Ω_1). This makes the optical spectrum much simpler, but is harder to implement with standard equipment. As with the DSB method, Ω_1 can be changed to tune the locking point. Using a sideband locking method generates a modified proportionality constant for the linear region of the error signal near resonance but otherwise produces the same signal. In this implementation, we use the DSB method.

4.2.2 Implementation & Results

When implementing this locking method, the majority of the time was spent aligning light into a high finesse cavity. A useful and important reference, providing guidance on this was Fox *et. al.* [65]. Fig 4.2 shows the optical setup that was used. A 99/1% splitter took 1% of the power directly from the laser output to the locking setup, where it passed through a polarizing beam splitter (PBS), a $\lambda/4$ waveplate, and a telescoping set of 2 lenses (a 100 mm focal length and a 50 mm focal length in that order) to mode-match into the cavity. The cavity used was a *Stable Lasers Systems* ultra low expansion (ULE) planar-convex cavity, with radii of curvature, $R_1 = \infty, R_2 = 50$ cm, length L=10 cm, and ν_{fsr}=1.5 GHz. This was contained in a vacuum chamber with an ion pump maintaining the internal pressure of $\approx 6.4 \times 10^{-8}$ Pa to ensure its stability.
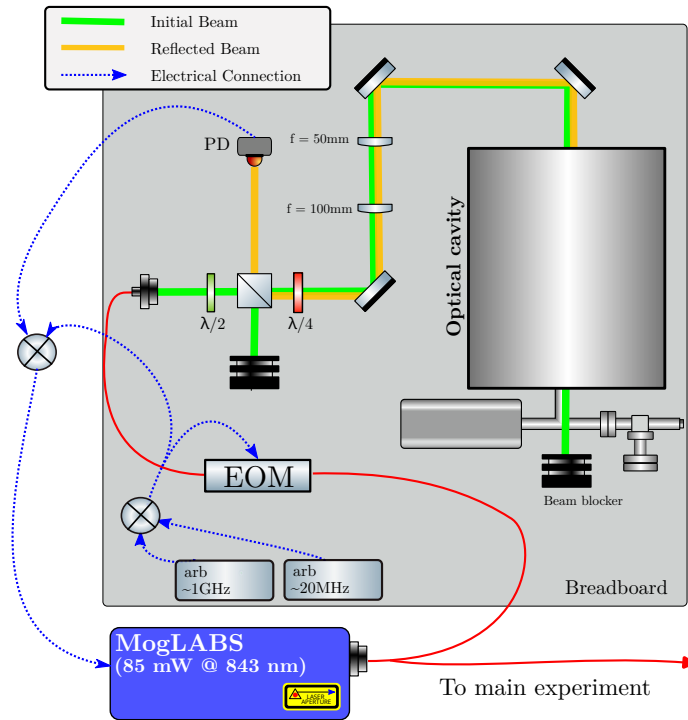
Figure 4.2: Beam path diagram for the PDH locking setup. The laser light is fibre coupled through an EOM, before coupling to the cavity in free space, shown by the green beam. The orange beam represents the reflected / leakage light from the cavity, that is picked off onto a photodiode. The blue dotted lines represent electrical connections, where the "arbs" are arbitrary function generators that provide the driving voltage for the EOM, and demodulation.

Initially, a photodiode and camera could be used to monitor the transmission when mode-matching the light to the cavity. Mode-matching involved firstly aligning the input beam so that the fundamental (TEM_{00}) mode was coupled most prominently - this was important to ensure the simplest locking signal and to reduce noise in the feedback system. Secondly, in order to mode match effectively, the beam waist at the initial planar mirror of the cavity must be such that the wave front of the Gaussian beam matches the radius of curvature of the curved second mirror inside the cavity. This fundamental beam waist can be calculated for a Guassian input [59, p. 182] as,

$$\omega_0 = \left(\frac{\lambda}{\pi}\right)^{1/2} (L)^{1/4} (R_2 - L)^{1/4}, \tag{4.25}$$

where a wavelength, $\lambda = 843$ nm, the length of the cavity, $L = 10$ cm, and the radius of curvature of the second mirror, $R_m = 50$ cm lead to an ω_0 of 0.232 mm. The focal length of a lens required to focus to this beam waist from an initial beam waist, w_1 is given by [101],

$$f = \frac{\omega_0 \omega_1 \pi}{\lambda}.$$ (4.26)

With an initial beam waist, $\omega_1 = 0.548$ mm, we required a lens of focal length, $f = 471$ mm; therefore a telescoping system of 2 lenses was more practical. In practice, getting the right beam waist was achieved by attaching the $l = 50$ mm lens onto a translation stage, which allowed for the position of the focus of the beam, and the beam waist to be shifted.

After approximately matching the wave front curvature, two turning mirrors were used to align the beam most strongly into the TEM$_{00}$ mode, along with an aperture to assist with the alignment and reduce power into higher modes that are spatially the furthest away from the centre of the beam [65]. Alignment could be performed by monitoring the transmission through a photodiode on an oscilloscope and adjusting the position of the mirrors until the spectrum showed highest coupling to the fundamental mode. This could be difficult as planar-convex cavity possesses a rich modal spectrum. A camera on the output, however, could be used to visualise the transmitted modes, and determine the fundamental mode. Ensuring the reflected beam was well overlapped with the input beam could also provide another alignment reference.

Figure 4.3 shows two cavity transmission spectra as the Rydberg laser was scanned, for demonstration, where (a) shows a case with poor alignment, and (b) shows the usage case with much better alignment. The varying heights of the peaks in (b) are due to the long build up time for a high finesse cavity, as the laser is scanned over several GHz. A camera on a pickoff for the transmitted beam
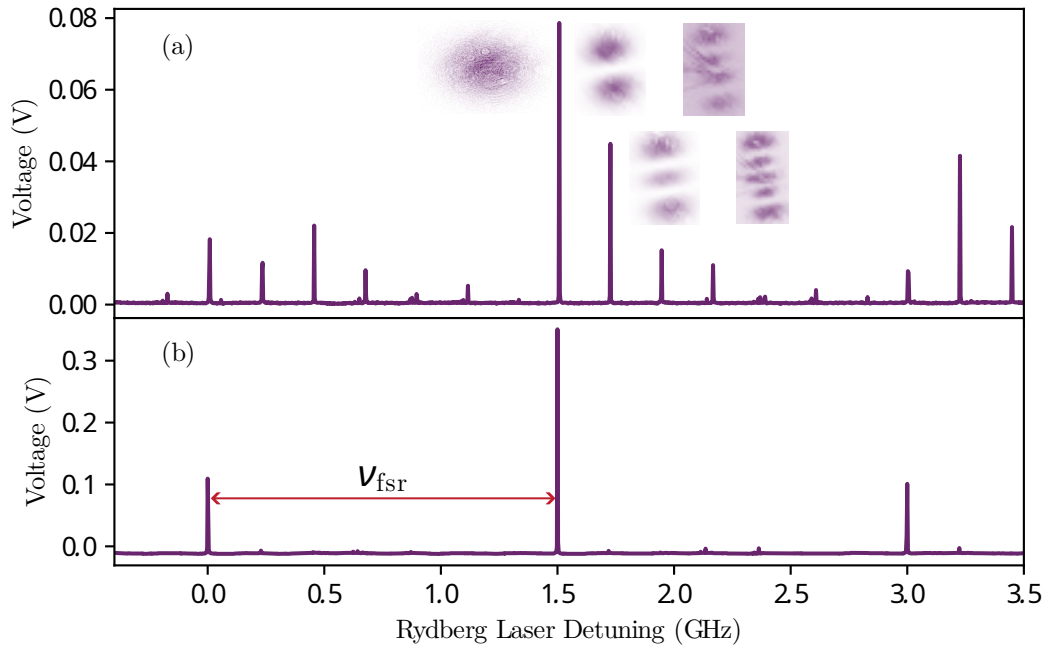
Figure 4.3: Oscilloscope traces of the transmission of the Rydberg laser through the cavity as the detuning is scanned. (a) Transmission with misalignment. Images taken with a CCD camera of the profile of the transmitted light are shown that correspond with different modes, from the central peak to the right in descending size order. (b) Transmission with good beam alignment. The higher order modes appear as much smaller peaks and the majority of the power is coupled into the fundamental mode. The distance between the fundamental mode peaks represents a free spectral range.

monitored the spatial modes, some examples of which are shown next to the relevant peaks in the spectrum in (a). In (b), any higher order modes visible are much smaller in magnitude than the fundamental. When the beam was well matched into the cavity, the reflected light could be picked off using a quarter waveplate and a PBS, onto a photodiode (*Thorlabs* PDA10A2). A modulation was then applied to the light. This was performed using a fibre coupled electro-optic phase modulator (Jenoptik PM830). The voltage to drive this was generated by a dual channel *TTi* TGF4042 and a *TTi* TGR1040. The TGF4042 generated an 80 mV signal at 20 MHz, which was combined on a *MiniCircuits* ZAD-6+ double balanced mixer with a -7 dBm signal at 625 MHz from the

TGR1040. This choice of modulation frequency placed a sideband on resonance with the atomic transition. The output from the mixer was amplified by a *Minicircuits* ZFL-500LN+ amplifier, and sent to the EOM. Then the signal from the photodiode collecting the reflected beam was demodulated by combining it with the second channel output of the TGF4042 (200 mV at 20 MHz) on a ZAD-6+. This was set at +30° phase difference from the first channel to compensate for accumulated phase in the demodulation circuit. Finally, the signal was passed through a 10 kHz low pass filter, in order to isolate the DC component. The resultant error signal after demodulation is shown in Figure 4.4a, in red.

The corresponding transmission peaks in panel (a) are shown in purple. The sidebands that generate the resonant error signal can be seen at $\Omega_2 = \pm 20\,\text{MHz}$, as well as the doubly modulated sidebands at $\Omega_1 = \pm 98\,\text{MHz}$. These sidebands also have smaller sidebands at ± 20 MHz. This second modulation frequency, Ω_2, was chosen to in order to easily display both sets of sidebands on a single trace.

With an error signal generated, the Rydberg laser could be locked to one of the sideband features using the MOGbox DLC202 laser controller. This had an internal PID controller, that enabled a fast and a slow lock to be engaged via the laser controller. Once locked, the Rydberg laser frequency could be tuned by changing Ω_1. The optimum modulation frequency could be determined by eye, by scanning the sideband over the atomic transition and seeing where the fluorescence was brightest. To test the improved stability of the fluoresence, it was measured over 8 mins whilst locked, and this compared to an unlocked fluorescence measurement. The results are shown in Figure 4.5. The normalised fluorescence signal when the laser was locked is shown in purple. This
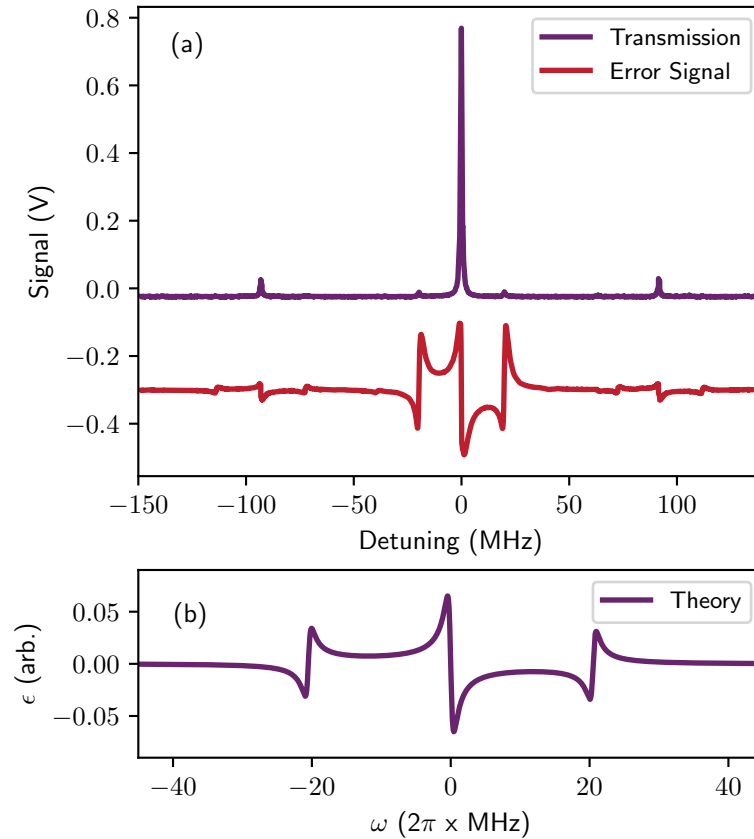
Figure 4.4: (a) The cavity transmission peaks in purple and corresponding error signal in red, taken from an oscilloscope, and frequency calibrated by the positions of the sidebands. The error signal has be offset by -0.3 V for clarity. (b) A theoretically calculated standard error signal, calculated from the eqn. 4.18, with modulation frequency and cavity mirror reflectivities, Ω=20 MHz and $r_1 = r_2 = 0.99$.

shows a decrease of $\approx 3\%$ across the 8 minutes, compared to the unlocked case (shown in red), which reduces in signal by almost 40% over the same time frame. By this basic metric, the lock was deemed to be sufficiently stable, as a 3% fluctuation is acceptable for quantitative imaging. Indeed, it is likely that a fluctuation on that order could have been caused by a temperature drift of the vapour, as opposed to laser frequency drift, as this would otherwise correspond to many MHz drift from the first and second step lasers, which would not be expected given they were both frequency stabilised.
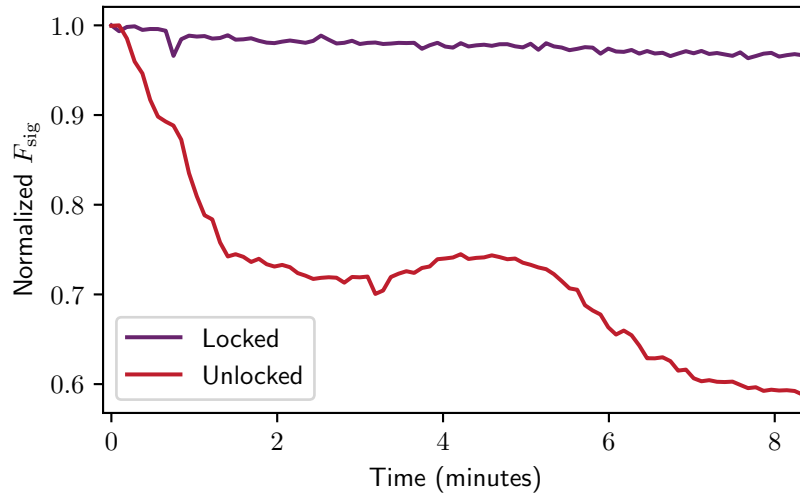
Figure 4.5: Fluorescence signal, averaged over the cell and normalised to the initial value, recorded in 100 datapoints over the course of ≈ 8 minutes. The purple trace shows the signal when the Rydberg laser was locked to the PDH error signal, whereas the trace in red shows the signal when it was free running.

4.3 Digital Scanning Transfer Cavity Technique

4.3.1 Introduction

In experiment 'B', an alternative locking technique, using a digital scanning transfer cavity technique, based on Subhankar *et al.* [80], was implemented. The main reason for using this system was to save costs, and avoid purchasing additional equipment. The PDH sideband lock required a phase modulation device, such as an EOM, a high finesse ULE cavity kept under vacuum conditions, the electronic components to modulate and demodulate the signal, and an appropriate high frequency signal generator to provide the modulations. This equipment can be both costly and difficult to work with, especially as, for example, the maintenance associated with vacuum equipment is introduced.

The chosen alternative on the other hand, requires only a cavity with the ability to scan, a waveform generator to drive the piezo, a microcontroller and a

custom PCB. The equipment used was chosen based on the equipment used in Subhankar *et. al* - a *Thorlabs* SA200-8B confocal Fabry-Perot cavity with length, $L =$50 mm was used, along with the matching SA201 control box, that could be used with to both scan the cavity, and amplify the transmitted photodiode signal. An Arduino Due microcontroller was used, and a custom PCB was printed and populated according to the specifications and parts list from the paper. The summed cost of this equipment was $\sim$ £3.5k, which compared to the $\sim$ £10k+ cost of the PDH equipment, was very cost effective.

In this section, we will briefly overview how the setup works, generally following the description in [80]. This will be followed by a discussion as to how it was implemented, and finally we will show some results to verify its stability. The working principle of a transfer cavity lock [102; 103; 104; 105] is to use a cavity to 'transfer' the stability of one stabilised laser, labelled a leader laser, to another, labelled a follower laser. When both lasers are input into the same scanning cavity, the cavity length will scan over each lasers resonance at different times, according to their different wavelengths, resulting in a spectrum that consists of peaks corresponding to each laser. In the all digital implementation, a microcontroller is used to perform the peak detection, generate an error signal and output a feedback control signal to both the laser and cavity. These control signals work to stabilise the laser frequency, and to stabilise the average cavity length, in order to prevent the cavity peaks from drifting off the end of a scan. For this lock, we require the cavity to scan a length slightly larger than one free spectral range of the leader laser, so that our transmission spectrum consists of a leader peak, l, then a follower, f, and then another leader peak, l', in that order. The microcontrollers algorithm detects the peaks in this order, and stabilises the follower laser frequency, and the average cavity length, based on

the peak arrival times. These times can be referenced to one another by,

$$t_i = (L_i - L_0)/\alpha, \tag{4.27}$$

where $i = $ l,f or l' are indices to represent each peak, L_0 is the arbitrary cavity length at $t = 0$, and α is the cavity scan speed. As a free spectral range is a constant in frequency space, the timing between the two leader peaks can be used to eliminate the dependence on α, by forming the ratio,

$$r = \frac{t_l - t_f}{t_{l'} - t_l} = \frac{L_l - L_f}{L_{l'} - L_l}. \tag{4.28}$$

We can use eqn. 4.6 to relate this cavity length ratio to a frequency, by taking the frequency to be an integer multiple of confocal free spectral ranges, $\nu = q\frac{c}{4nL}$, and by taking $q_{l'} = q_l + 1$, then substituting and rearranging to get,

$$r = q_l - q_f \frac{n_l \nu_l}{n_f \nu_f}, \tag{4.29}$$

where the $n_{f,l}$ are the refractive indices of the air for light at the frequencies $\nu_{l,f}$. The positions of the peaks ensures that $0 < r < 1$, and constrains q_f. By choice of a reference frequency, $\nu_{f0} = (\nu_l n_l q_f)/(n_f q_l)$, the follower laser frequency relative to this can be defined,

$$\delta\nu_f = \nu_l \frac{q_f n_l}{q_l n_f} \left(\frac{r/q_l}{1 - r/q_l} \right) \approx \frac{q_f}{q_l} \nu_{\text{fsr}} r, \tag{4.30}$$

where the last step assumes $r/q_l \ll 1$ and $n_l, n_f \approx 1$. by this relation, we can choose a setpoint r_0, and deviations of r from this ratio setpoint due to laser frequency fluctuations generate our error signal.

4.3.2 Optical Implementation

In our implementaton, we wanted to use the cavity to lock the free running Rydberg laser (843 nm) to the probe laser (852 nm) that was stabilised to the
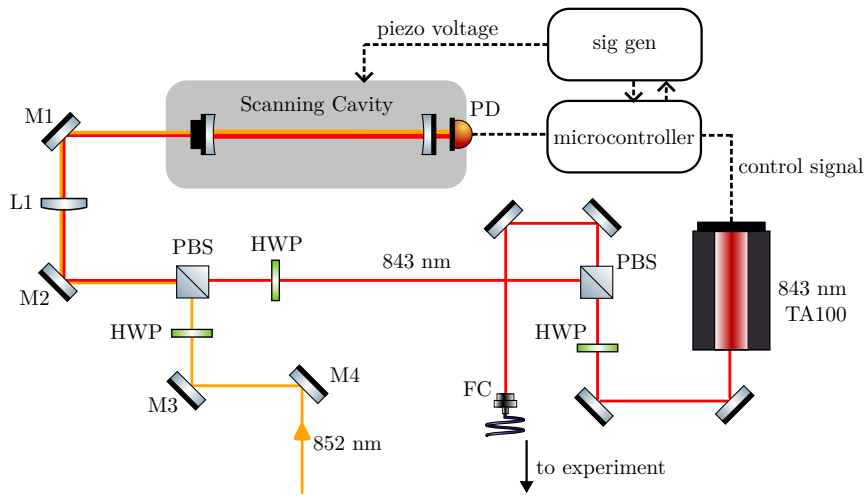
Figure 4.6: Beam path diagram for the STCL locking setup. PD: photodiode, HWP: half waveplate, PBS: polarising beam splitter, M1-4: mirrors, L1: lens, FC: fibre collimator

$|6S_{1/2}, F = 4\rangle \rightarrow |6P_{3/2}, F' = 5\rangle$ transition. The optical beam path designed to couple both lasers into a single cavity is shown in Figure 4.6. The Rydberg laser beam (843 nm) is split into a branch for locking, and a main beam, that gets fibre coupled and taken to the main experiment. The locking beam is coupled into the cavity using two turning mirrors, M1 and M2. The probe laser beam (852 nm) is combined in this path on a PBS. The alignment process consisted of adjusting M1 and M2 to optimise the Rydberg laser peaks, and then adjusting M3 and M4 to optimise the probe laser peaks. L1 was a 200 mm aspheric lens, to focus the beam at the centre point of the cavity, in order to mode match the light to the cavity. The cavity was then scanned using the *Thorlabs* SA201, and the photodiode signal was fed back into the SA201, where it was amplified and displayed on an oscilloscope. The resulting oscilloscope signal is shown in Figure 4.7. The red trace shows the scan voltages applied to the cavity, with the transmission peaks from both lasers shown in purple. The first and last peaks appearing in the forward scan range are corresponding to the two leader peaks, whilst the one in between corresponds to the follower peak. The relative peak
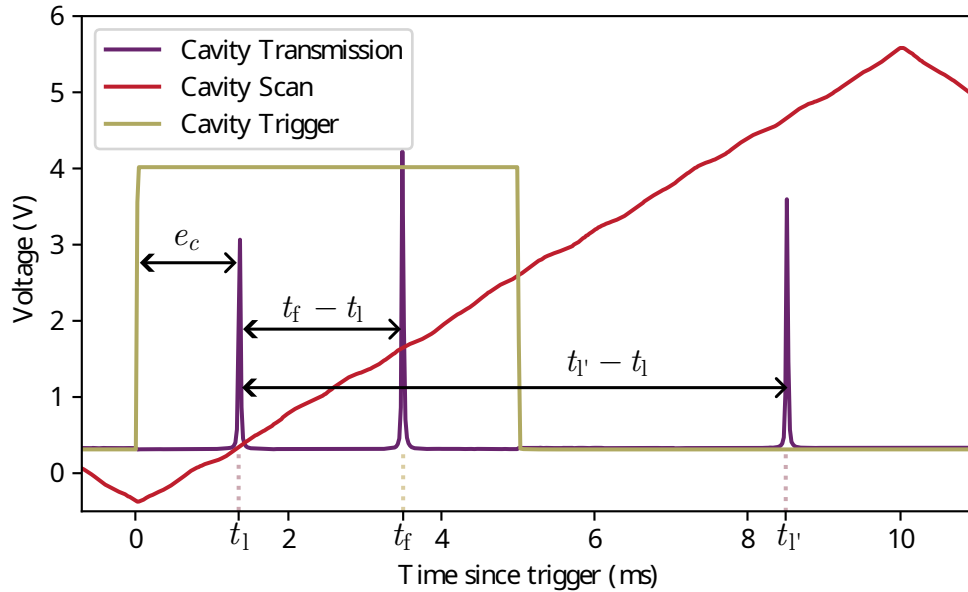
Figure 4.7: Oscilloscope trace for the STCL lock, as the cavity is scanned. The purple trace shows the cavity transmission voltage, the red trace shows the ramp voltage, and the gold trace shows the TTL trigger. The arrival times of each peak are labelled on the x axis. The relevant quantities to locking are also labelled by arrows: the cavity error signal, e_c, the follower-leader peak timing diffrence and the follower-follower peak timing difference. The laser error signal is defined from the ratio of these quantities. Each of these 3 signals are input onto the PCB.

heights can be controlled by the half waveplates before the beam splitter.

4.3.3 Electronic Implementation

With the optical setup implemented, and readable on a scope, we could then set up the electronic side of the lock. In accordance with [80], (`https://github.com/JQIamo/Scanning-Transfer-Cavity-Lock`), a few modifications were required to the existing hardware, in order for the Arduino to work in tandem with a custom shield board. The analog reference jumper was moved to the position to allow for an external reference to be provided by the shield board, and, as the shield board was designed to power the arduino, the polyfuse attached

to the USB port could be removed, in order to prevent current from flowing to the computer from the board. To allow for an external feedback from the board to the cavity scan offset, the voltage offset potentiometer on the SA201 was disconnected. In its place, we directly connected to the offset pins of the driver with a wire, whose other end was soldered with a BNC connector, to allow for easy connection / disconnection.

A printed circuit board (PCB) was acquired and populated with similar parts to the paper. The choice of R1 (for board schematics, see the above link), the resistor on the laser control output from the board, is dependent on the system being used. This is because it forms a voltage divider with the input impedence of the laser controller, where,

$$R_1 = R_2\Big(\frac{V_{\text{in}}}{V_{\text{out}}} - 1\Big), \tag{4.31}$$

where R_2 is the input impedence, and V_{in} and V_{out} are in the input and output voltages. In our case, we wanted to feed back to the piezo of a *Toptica* TA100, controlled by a DLC100. These laser controllers allow for an external voltage to be input, by using the analog reference board in the rack. By choosing the jumper placement appropriately, this board can transfer a voltage via the backplane to the SC110 module, where an input voltage is amplified by a factor of 15 (in high voltage mode). The board accepts ± 5 V, with an input impedence of 10 kΩ. As the laser control output voltage from the amplifier chip (*Texas Instruments* INA2128) was 12 V, we required the voltage divider to bring the voltage down to 5 V. Much more than this would be likely to burn out the amplifier chip, and much less than this would lead to sub-optimal performance from the lock, as the frequency could not be changed sufficiently. Therefore, with the parameters in this system ($R_2 = 10$ kΩ, $V_{\text{in}} = 12$ V, $V_{\text{out}} = 5$ V), we calculate according to eqn. 4.31 a required resistance, $R_1 = 14$ kΩ.

With the board fully populated, it could be attached to the Arduino, and powered with an external ± 12 V power supply. The relevant voltages were interfaced by BNC, with inputs being: the scan trigger, the cavity transmission signal and the scan voltage. The outputs consisted of connections for the cavity control signal and the laser control signal.

4.3.4 Digital Implementation

The Arduino board is programmed by an application called the *Arduino IDE*. This acts as a cross compiler and code editor, using a language largely based on `C++`. The Arduino is equipped with a 32-bit *Atmel* AT91SAM3X8E processor, with an 84 MHz clock speed, and an 12-bit DAC/ADC. This is important to note in order to convert to physical units later. A useful guide to the SAM3X family of processors can be found at [106]. We will briefly describe here how the programme is coded to work.

The programme flow is is based on Interrupt Service Requests - certain events, called interrupts, trigger the software to carry out certain tasks, before returning to the normal flow of the programme. For example, the rising edge of the cavity scan trigger acts as a trigger for the memory to refresh - the scan trigger acts as a zero point for the timings. The timings of each peak are recorded by the internal clock function (`SysTick`). The voltages for each peak are committed to memory only around in the region around the peak, by the following process: when the voltage reads above a certain (user defined) high threshold, an interrupt triggers the ADC to start acquiring data points and committing them to memory, and when the voltages drop below a certain (user defined) low threshold, another interrupt triggers the ADC to stop acquiring points. The centre of these peaks is determined by a 5 point Savitzky-Golay filter [107],

whereby the derivative of the datapoints is calculated, and the peak centre taken to be the zero point of the derivative.

When the datapoints for each peak centre have been collected, the error signal and subsequent control signal can be generated. The cavity error signal, $e_{\mathrm{cavity}} = t_{\mathrm{set}} - t_l$, is simply the difference between the cavity setpoint (in time units) and the timing of the first peak. This is shown by the arrow labelled e_c in Figure 4.7. The laser error signal, is defined by $e_{\mathrm{laser}} = r_{\mathrm{set}} - r$, where r is the ratio defined in eqn. 4.28. In the code, the setpoint and r include a factor of 10^6, presumably to bring the values into a similar range as the other setpoint. The output control signal was then calculated with a PID servo loop, by discretization of eqn. 4.1.

In implementing this setup, elements of the code were modified, in collaboration with Adam Selyem and Brynmor Jones of the Fraunhofer Centre for Applied Photonics [17]. They modified the PID loop from the original paper, to include a derivative term, so that in the digital equivalent of eqn. 4.1, the integral becomes a sum over previous error signals, multiplied by a small time, ΔT, using an addition-assignment operator and the derivative becomes a difference between the current and previous signals, divided by ΔT. A derivative term for the cavity lock was not used, as it would not require a fast response.

We modified the "rails" on the output (designed to prevent windup, or too large an output control signal), as the way it was defined prevented any output to the cavity. Fraunhofer also implemented code to communicate with the programme while it is running, without using the IDE's serial monitor. This allowed variables to be changed and printed without reprogramming the board. They developed a Labview virtual instrument to encapsulate these communication abilities, a screenshot of which is shown in Figure 4.8. The user interface
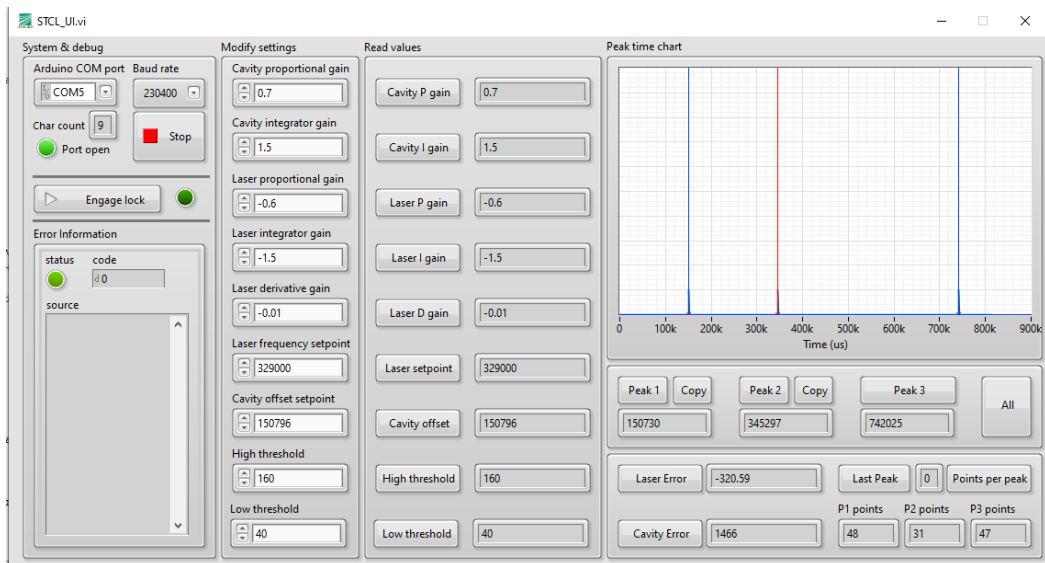
Figure 4.8: Labview virtual instrument to control the STCL. See text for explanation of features. Credit for design: Adam Selyem & Brynmor Jones, Fraunhofer Centre for Applied Photonics.

was set out as such:

- The leftmost section allows for a COM port for serial communications to be selected, a Baud rate to be set, and for the lock to be engaged, via "Engage lock". A green light indicates whether the lock is engaged or not. The column beneath it displays any error messages.

- The next column allows for the modification of relevant parameters. The PID gain parameters for the cavity and laser lock can be changed here, as well as the two setpoints, and the high and low peak detection thresholds.

- The next column allows the parameter values to be printed, when the associated buttons are pressed.

- The rightmost section shows an illustrative diagram of the peak locations (Note: the time axis units are incorrect - see next section). Underneath that, the "All" button refreshed the positions of every peak on the diagram, and displays their detected timings in the 3 boxes. The first "copy"

button copies the value of the first peak position into the cavity offset set-point variable, and the second "copy" button copies the current value of r into the laser frequency setpoint variable. These features make it easy to lock the peaks to the position they are currently in. Beneath this, the laser and cavity error buttons print the current values of the error signals. The "Last Peak" button displays the number of the last peak the programme detected, and the "Points per peak" displays the number of datapoints that the programme has picked up between the thresholds. This is useful for determining whether sensible threshold values have been chosen.

It is useful to know how the digital parameters convert to physical units, in order to select their values appropriately:

- The gain parameters are all unitless.

- All timings are recorded in terms of ticks from the internal 84 MHz clock. This means that a single tick is equivalent to $1/(84 \cdot 10^6) = 1.2\text{E-8}$ seconds. A peak at say, 150,000 in the software, therefore appears 1.78 ms after the scan trigger. These are the units that the cavity setpoint is in, for example.

- The laser frequency setpoint is represented in units of $10^6 \cdot r$. Therefore, a software value of 300,000 actually corresponds to an r of 0.3.

- Voltages are interpreted via the 12-bit ADC/DAC. This means that a signal unit converts to voltage by a factor of $1/2^{12} = 1/4096$. A high threshold of 180 therefore converts to 43.9 mV.

4.3.5 Results

Once the lock was set up, the lock parameters could be manually optimised by the usual methods, using the Labview UI in order to achieve the best stability. The locked peak could then be tuned by adjusting the laser frequency setpoint in the software. The frequency could also be adjusted in a Python script by writing to the programme using `Pyvisa`, which turned out to be a very powerful feature. The frequency could in principle be tuned freely across the entire scan range of the follower laser, with the exception of where the leader laser is resonant. However, as the peak datapoints are collected within a set timing window, with appropriate choice of thresholds, the resolution between peaks detected could be narrower than width of the peaks, meaning the 'holes' in the tuning range should be minimal. In order to use the tuning ability to best effect, it was useful to know the conversion factor between a change in r and a change in frequency.

4.3.5.1 Frequency Calibration

On first principles, the frequency change, $\Delta\nu_f$, associated with a change in r, Δr could be calculated from the cavity properties as [80],

$$\Delta r \approx \frac{q_f \nu_l}{\nu_f^2} \Delta\nu_f = \frac{4L\lambda_f}{c\lambda_l} \Delta\nu_f = \beta^{-1} \Delta\nu_f, \tag{4.32}$$

where $\lambda_{f,l}$ represents the wavelengths of each laser, and the approximation comes from assuming $n_f, n_l \approx 1$. This beta-factor can be used to convert a change in r into a change in frequency, and $\beta = 1.516$ GHz in this system. To scan over the Rydberg transition, we use a scan range that corresponds to $\Delta r = 0.14$. Using eqn. 4.32, this converts to a frequency span of 212.3 MHz. The largest uncertainties in this value come from possible uncertainties in the
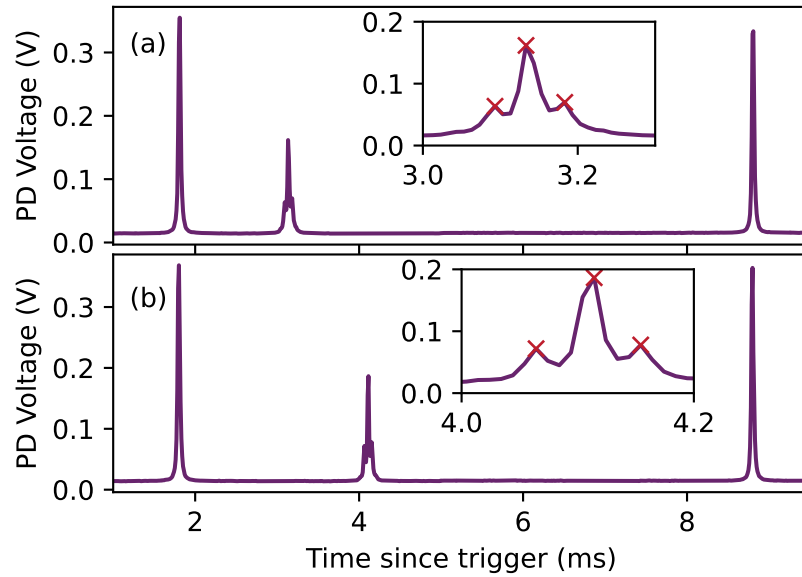
Figure 4.9: Cavity oscilloscope traces, taken to calibrate the frequency conversion of the digital lock, with, (a) the follower peak setpoint set to $r = 0.19$ and (b) the follower peak setpoint set to $r = 0.33$. The insets show the follower peaks on a smaller scale. The modulation sidebands can be seen more easily, and the detected peak positions are labelled with red crosses.

cavity length. For example, a ± 1 μm error in cavity length would lead to an error in this frequency value of 10^{-3} MHz, whilst an error of ± 0.1 pm (or equivalently ≈ 41 MHz in frequency) in the wavelength would result in a frequency error of $\pm 10^{-5}$ MHz

In order to confirm this value, some further calibration was performed, by two different methods. This involved taking oscilloscope traces, with the follower laser locked at two different values of r: 0.19 and 0.33. These traces are shown in Figure 4.9, in panel (a) and (b), respectively.

The first method involved measuring the times between the two leader peaks, and relating this to a free spectral range, to get a measure for the frequency per millisecond. The peaks locations were found using `scipy.signal.find_peaks()`, and the time between the two peaks found to be 6.99 ms. With a free spectral range of 1500 MHz, this works out to be 214.4 MHz per ms on the scope. Then,

subtracting a small offset to line up the first peak in traces (a) and (b), the difference between the follower peaks at either setpoint was found to be 0.991 ms. Using the prior calculation, this turns out to be a scan range of 214.4 * 0.991 = 212.4 MHz, within a decimal place of the value calculated from first principles. The main uncertainty from this method may come from non-linearities in the scan, meaning that it is slightly slower or faster near the beginning/end of the scan, which would affect the MHz-to-ms converstion.

The second method involved modulating the follower laser with an EOM at a known frequency, to generate sidebands on the peaks at that frequency. The timing between the sideband and the carrier peaks could then, again be used to get a measure for the frequency per millisecond. With an EOM modulating at 8.6 MHz, the timing between the sideband and carrier peaks was found to be 0.04 ms, which gave 214.8 MHz per ms on the scope. Multiplied by the timing between the peaks at each setpoint, gave a total scan range of 212.8 MHz. This method reduces the uncertainty from the linearity of the scan (as it is calibrated over a much smaller region), but the largest uncertainty introduced is actually from the frequency of the EOM. A basic *TTi* TG320 function generator was used to generate the modulation, but this was controlled with only a potentiometer knob to select the frequency, which could be imprecise. A modulation frequency of ± 0.1 MHz led to an uncertainty in the total frequency over the scan range of ± 2.5 MHz, so this was the largest source of error. Nonetheless, the three methods agree within .5 MHz, so this frequency calibration was used whenever the Rydberg laser was scanned.
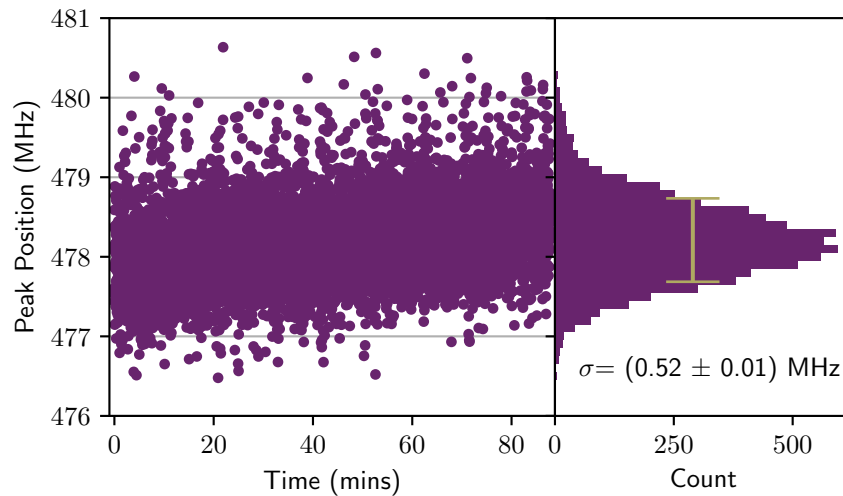
Figure 4.10: Rydberg laser / follower peak stability, recorded with 7200 data-points over almost 90 minutes. The peak position in converted frequency units is plotted on the y axis against time on the x axis. The right hand histogram plots the cumulative frequency distribution with 60 bins. The label shows the standard deviation of the measurements, where the error comes entirely from the error in the frequency calibration.

4.3.5.2 Stability

The main desired outcome for the lock was to maintain long term stability, and remove the need to adjust the Rydberg laser frequency offset to compensate for drift. To that end, we monitored the cavity peak positions over time. The follower peak position, tracked using the programmes peak detection algorithm, is shown, sampled 7200 times over 90 minutes, in Figure 4.10.

The follower peaks position in frequency space was calibrated according to the beta conversion factor (eqn. 4.32). There is a slight drift visible over the course of the 90 minutes, that could be attributed to a drift in cavity temperature as all of the peaks drifted equally (meaning it does not correspond to a frequency drift), but plotting a histogram of the cumulative values and finding the standard deviation, the average spread in frequency was only 0.52 ± 0.01 MHz. The uncertainty is purely derived from the uncertainty in the frequency calibration.
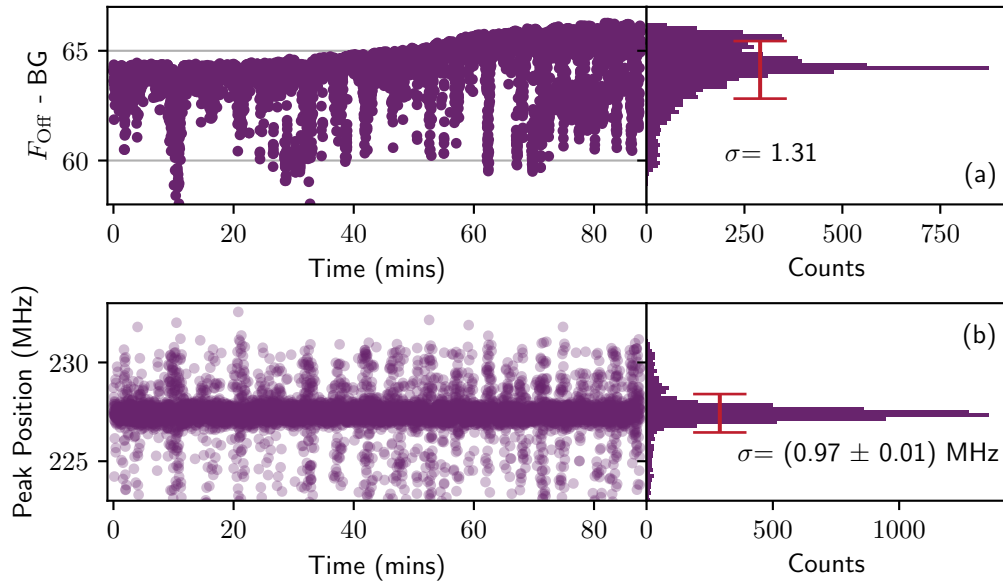
Figure 4.11: (a) "THz Off", F_{Off} fluorescence, averaged over the beam area, with a background measurement subtracted. (b) The probe / leader peak position, in converted frequency units, over time. In both, the histograms on the right represent the cumulative counts of the datapoints, divided into 60 bins. The standard deviations are also labelled. In (b), the error is calculated purely from the error in the frequency calibration.

This seems more than sufficient for our purposes. We also measured the F_{Off} signal over this period, which is plotted, with a background shot subtracted, in (a) of Figure 4.11.

The "THz Off" fluorescence signal (measured to exclusively evaluate Rydberg laser stability) shows an overall upward drift over the course of the measurement, that could likely be attributed to a temperature drift, affecting the number density of atoms in the cell. This drift was of the order of 3% over 90 minutes. There was also an effect whereby the fluorescence spiked downwards occasionally. The standard deviation of all the datapoints was 1.31, which represents a 2% fluctuation over this timescale. This number was increased by the dips in fluorescence that occur.

Upon further investigation, it was found that, by tracking the leader peak posi-

tion over time, this also showed spikes away from resonance, at the same times as the fluorescence dips. This suggests that at the time, there was some ringing occurring on the probe laser lock, that was causing the frequency to occasionally jump away, and quickly return. This was likely due to sub-optimal PID gain parameter settings. The ringing effect caused an overestimate in the average peak position fluctuation, as 0.97 ± 0.01 MHz was measured over this timescale. If we artificially eliminated the frequency jumps, a standard deviation of 0.35 ± 0.01 MHz was measured. Again, here the uncertainties are derived purely from the uncertainty in the frequency calibration. The fact that this ringing effect is not seen the follower peak position likely suggests that either the bandwidth of the lock was not quick enough to respond to the frequency spikes of the leader peak in time, or that the cavity lock was able to adjust in tandem with the leader peak frequency. As the cavity scan speed was ≈ 50 Hz, and the bandwidth is limited by this speed, the first reason seems the more likely of the two.

Using the fluorescence data, we can acquire a total upper limit on the Rydberg laser stability. Say we naively assume that the fluctuation in the fluorescence, given by the standard deviation, is entirely due to fluctuations in the Rydberg laser frequency. We can compare this value to a previously taken measurement of the effect of the detuning of the Rydberg laser in 'Experiment B' on the fluorescence. A fluctuation of 1.31 would, in that case, correspond to a frequency detuning of 2 MHz. The assumption that the fluorescence fluctuation is entirely due to Rydberg laser frequency fluctuations is clearly wrong, so this represents a high upper limit on the stability of the lock.

4.4 Conclusion

In this chapter, we have discussed two methods for frequency stabilisation of the Rydberg laser. We first introduced the basics of PID controllers, which are the universal feedback controllers used for implementing frequency stabilisation. We then introduced the basic Fabry-Perot resonator theory required to understand the basis for the two locking schemes, as both utilised cavities for frequency references. A theoretical basis was developed to understand the Pound-Drever-Hall technique, and an account of how the lock was set up was given. Similarly, a brief theoretical introduction was described to understand how the properties of a cavity allowed us to generate a scanning transfer cavity error signal.

Each lock was implemented in a different experiment, and both saw levels of stability that were entirely sufficient for the lenient requirements we desired. The main parameter of interest, F_{sig}, the fluorescence signal, saw similar levels of fluctuations with both locks, which suggests that the Rydberg laser lock was not the limiting factor on the stability of the measurements.

Ultimately, this meant that either locking method could be suitable for our application, or an application that does not have high bandwidth requirements. For linewidth narrowing or similar applications, only the PDH lock can provide sufficient bandwidth, as the STCL is limited by the scanning rate of the cavity, due to the fact the refresh rate of the programme is linked to the scan trigger events. On the other hand, for more lenient requirements, the STCL is much cheaper, and is much less demanding in terms of the optical alignment requirements. If, however, issues are encountered with the Arduino or the shield board, then troubleshooting can require a diverse range of knowledge of elec-

tronics, Arduino architecture, `C++` etc. Nevertheless, when working, the implemented communications protocols allow for very easy interfacing of the digital lock with other systems, which is a very valuable feature that allowed for dynamic setpoint changes within an experimental control sequence.

Fluorescence Characterisation

In this chapter, we investigate the effect various experimental parameters of the imaging system have on the magnitude of our fluorescence signal, $F_{\mathrm{sig}} = F_{\mathrm{On}} - F_{\mathrm{Off}}$. We aim to increase the signal to noise ratio in our images, for a number of reasons. For example, this would lead to improved sensitivity, and improved performance at low THz field strengths. A larger signal could help to enable the development of potentially lossy techniques such as THz spatial light modulation [108] and super resolution imaging [109] in this system. Characterisation of the system parameters will also aid in progress towards commercialisation or further development of the system, by providing benchmark measurements for troubleshooting. Ultimately, the effect of optimising these parameters is to increase the Rydberg level populations, and therefore increase the amount of decay fluorescence. The experimental parameters that influence the Rydberg level populations include the detuning and intensity of all 3 excitation lasers, the temperature of the cell, which affects the number density of atoms, and the polarisations of the driving fields.

Section 5.1 will cover the method and effects of varying each laser intensity, and thus the Rabi frequencies on each transition. Data will be presented through

colourmaps, and a basic model based on the density matrix master equation method will be introduced in order to simulate results. Section 5.2 will cover the method and effects of varying the polarisation states of each laser, which in turn affects the dipole allowed transitions via selection rules, and so transfers population among m_F states differently. Sections 5.3 and 5.4 will cover the effects of varying the Rydberg laser detuning, and both the Rydberg laser and THz source detuning, on the spectra and fluorescence signal, and make use of the Lindblad master equation (see section 2.45) to simulate these results.

5.1 Effect of laser powers on fluorescence emission

In previous use, the imaging system has been operated with moderate laser intensities on the first two transitions, and as much power as possible on the final step, based on an intuition about the relative dipole matrix elements of each transition, i.e that the Rydberg level transition has a much weaker dipole matrix element than the others, and so requires more laser intensity to drive it.

In this subsection, a full characterisation of the fluorescence signal dependence on the relative laser intensities is performed, and the optimal powers extracted. This means taking average fluorescence measurements, across the range of laser powers we have available, across all 3 excitation lasers, in experiment 'A'. In experiment 'A', the beams are collimated through the cell, with a beamwidth of ~ 1 mm each. This should also serve as a benchmark reference for the power requirements of each step, should the system be replicated commercially.

5.1.1 Calibration of noise-eater attenuation voltage with output power

Free space-coupled commercial noise eaters were used in this investigation for each beam, to both stabilise the power into the cell, and to attenuate it controllably with an applied voltage. These consisted of the *Thorlabs* NEL04A/M and NEL03A/M for the coupling beam and then the probe and Rydberg respectively. Internally, they consisted of a liquid crystal retarder, combined with a linear polariser and beamsplitter pick-off. The liquid crystal retarder rotated the polarisation of the input light, in response to an applied voltage, which had the result of changing the output power through the polariser. The pick-off monitored the power, and was fed back in a servo loop to the liquid crystal retarder stabilise the output power. A potentiometer on the top or an external voltage supplied via SMA allowed the user to change the setpoint, to change the output power. As such, the noise eaters were used to controllably vary the power of each individual beam, as fluorescence measurements were taken. Figure 5.1 shows the output power response across the an applied voltage range (0.2–0.8 V), measured with an optical powermeter.

Because there is a minimum and maximum voltage where the change in voltage is linear with the change in power, only this region was used in data runs. The dynamic range of this linear region depended on the input polarisation, so that it was not possible to attenuate fully from maximum power to zero power. Because of this, a calibration run was always taken prior to any fluorescence measurements and the appropriate voltages changed, in order to account for any long term polarisation drifts. A calibration run consisted of a measurement of the power of the beams being investigated with an optical power meter
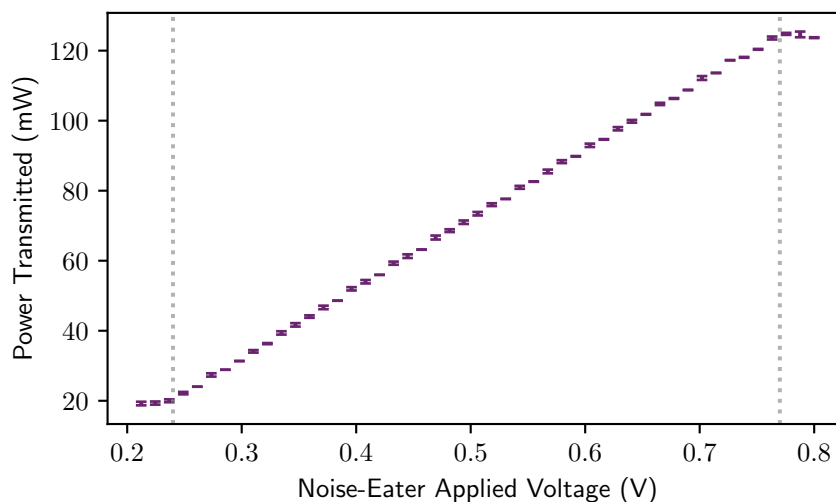
Figure 5.1: A calibration scan for a data run with the noise eater - the applied voltage to the noise eater against the transmitted power for the 843 nm beam. The dotted lines indicate the linear region that would be taken for a data run. The errorbars represent the standard error on the mean with 3 repeat measurements. The input power was around 125 mW. Under normal operating conditions there was negligible power drift at a set voltage.

placed immediately before the vapour cell, as a function of the voltages chosen to apply to the noiseeater. These power measurements were recorded, and the powermeter heads removed, to allow the light to reach the cell, and excite the atoms and the recorded power measurements were taken to be the power at each particular voltage.

5.1.2 Results

For data runs, the voltages set during the calibration run were used, but could be passed through in a random order, in order to prevent any bias through long term drifts as a measurement run was taking place, such as temperature drifts due to air conditioning in the lab. Each data run varied the power of two of the beams at a time, with the third being fixed, and the 3 different configurations of each beam were taken (probe+coupling , coupling+Rydberg, probe+Rydberg).

Figure 5.2 shows the results for each of the 3 configurations, for the average of 190 consecutive repeat runs each. The powers of the fixed beams were 3.5 mW, 8 mW and 120 mW, for the probe, coupling and Rydberg lasers respectively.

The colourbar represents the $F_{\text{sig}} = F_{\text{On}} - F_{\text{Off}}$ fluorescence signal, when averaged over the beam area, from images taken with 50 ms exposure. Each graph is plotted against the calibrated power, and the secondary axes represent the equivalent approximate Rabi frequencies for each beam. The Rabi frequencies were calculated using `ARC`, (see section 2.4), based on linearly polarised beams exciting the $m_J = 1/2 \rightarrow m'_J = 1/2$ transition on each step, and assuming a circular beam, the size of the measured beam waist for each beam at the cell. We note some periodic fluctuations visible in the third panel, that can be mapped to consistent temperature fluctuations, likely due to air currents from the air conditioning unit being left on overnight, as this run was not taken in a randomised order.

The results show that the most important beam power to consider is the Rydberg laser, as expected, due to the small line strength of the transition (of order $0.00011e^2a_0^2$). The lowest signal values by far are seen when the Rydberg laser power is low. This can also be seen by the fact there is no maximum fluorescence in the 843 nm plane in either configuration - so the more Rydberg laser power we input, the more fluorescence we get out. In contrast, the first step laser can be seen to saturate - in both the first and second panels, the 852 nm beam reaches a maximum signal value around 1-3 mW. These panels also show the 1470 nm beam begin to level off at around 8-10 mW, before likely beginning to decrease. This saturation effect is likely due to splitting of the line due to the AC stark shift [56], the magnitude of which is proportional to the Rabi frequency. As the line splits, the beams will become off-resonant
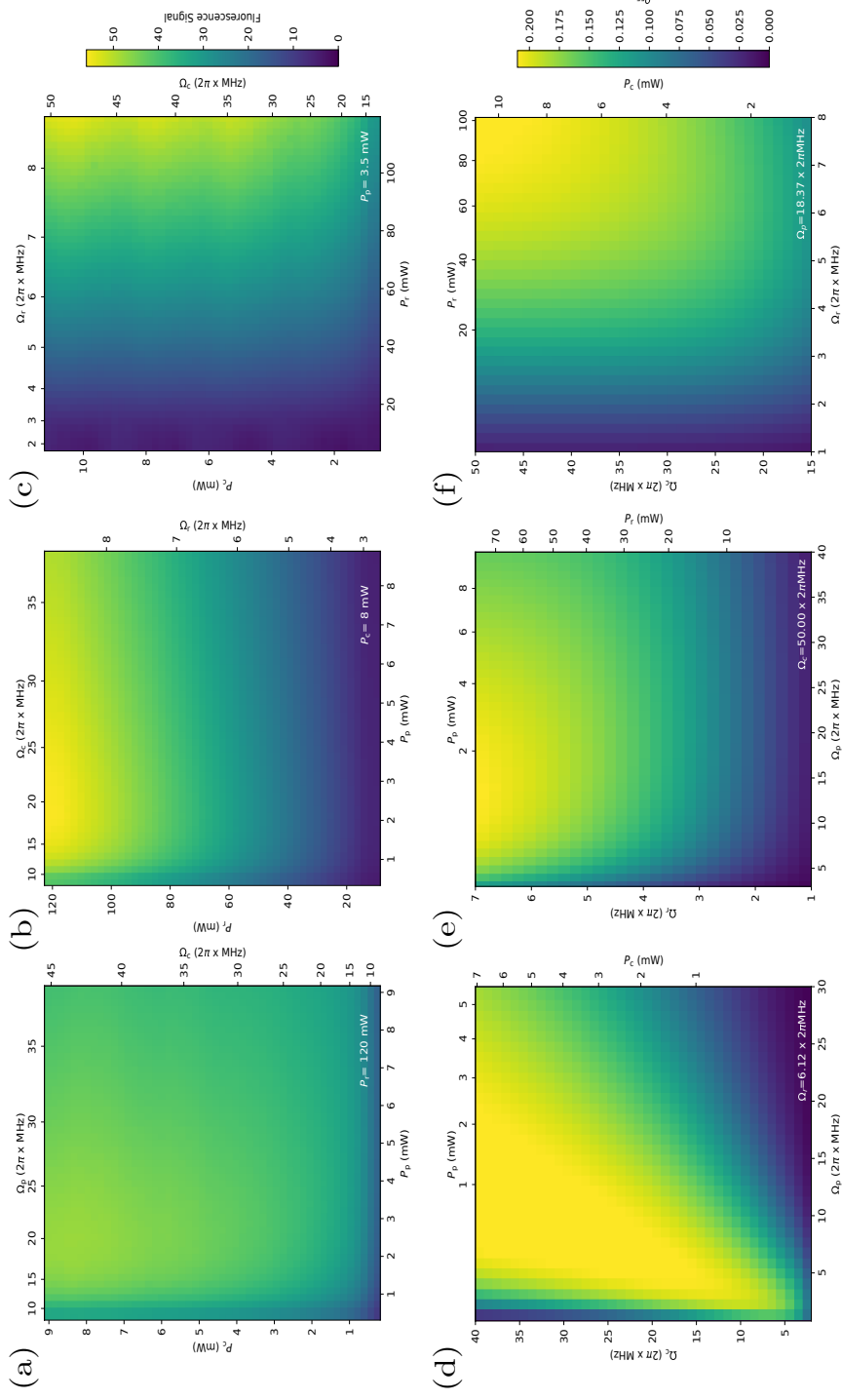
Figure 5.2: (a-c) Experimental and (d-f) modelled data, showing the fluorescence signal, F_{sig}, as a function of the powers/calculated Rabi frequencies of each beam. The first, second and third panels show the (probe & coupling), (probe & Rydberg) and (Rydberg & coupling) lasers respectively, on each axis, with the 3rd, 2nd and 1st powers fixed. The fixed values for each plot are shown in the bottom right. The secondary axes in (a) show the equivalent calculated Rabi frequencies, whilst the secondary axes in (b) show the equivalent calculated powers, from the modelled Rabi frequencies. The simulation parameters were $\Delta_{\mathrm{p,c,r,THz}} = 0$, $\Gamma_{\mathrm{p,c,r,THz}} = 6, 1, 1, 1 \times 2\pi$ MHz

with the transition being split. The multi level nature of the system, however, means that the values at which the signal saturates depends on the power of the fixed beam. This can be more easily investigated through modelling.

Figure 5.2(d-f) shows colourmaps of the same sets of parameters, each corresponding to the panel above it, with the colour representing the modelled $13D_{5/2}$ population, taken by the fifth diagonal element of the density matrix that is a solution to the Lindblad master equation. The terahertz-coupled level population is taken as a proxy for the fluorescence signal, as the number of atoms that can decay via the 535 nm route is directly proportional to the number of atoms in that level. A five level Hamiltonian was initialised to represent the atomic system, with zero detuning for each beam, and a Lindbladian operator representing spontaneous decay for each level to that directly below it, and a 100 kHz linewidth for each laser. The master equation (section 2.4.3) was solved for varying Rabi frequencies for each transition, in order to model the varying powers. The parameters were then adjusted until the model showed good qualitative agreement to the trends shown in the data. The Rabi frequencies calculated do not necessarily match up well, due to the assumptions made in calculating them, i.e, only considering one sub-level transition, and taking the peak power of the Guassian beam to represent the power, rather than the integrated area, etc. Due to the square relation between the power and the Rabi frequency, and the uncertainty of the calculation, the experimental data was left plotted as a function of the power, to avoid distorting the colourmap. This means, however, that there was not a one-to-one mapping between the model and the experimental data. The Rabi frequencies required for the model to match the data are shown in Figure 5.2.

5.2 Effect of laser polarisations on fluorescence emission

In order to investigate the effect the polarisation of each laser had on the overall fluorescence signal, we first needed to accurately determine and change the polarisation states of each beam. To allow control over the polarisation states, we use quarter waveplates in each beam path, just before the cell, mounted in automatic rotation mounts that can be controlled via the computer.

5.2.1 Polarimetry

In order to most effectively isolate the effects of changing polarisation, the polarisation states first had to determined. This amounted to calculating the Stokes parameters for each beam, which fully describe the classical polarisation state of the light. As described in [110], in order to determine the polarisation state, a quarter wave-plate (QWP) and a PBS were used in an compensator-analyser combination, as shown in Figure 1 of [110]. In general, for a monochromatic plane wave, the intensity of light transmitted to the detector in this setup can be described by,

$$
\begin{aligned}
I(\theta, \alpha, \Delta) = \frac{1}{2}[&S_0 + (S_1 \cos 2\theta + S_2 \sin 2\theta) \cos 2(\alpha - \theta) \\
&+ (S_2 \cos 2\theta - S_1 \sin 2\theta) \sin 2(\alpha - \theta) \cos \Delta \\
&+ S_3 \sin 2(\alpha - \theta) \sin \Delta],
\end{aligned}
\tag{5.1}
$$

where S_0-S_3 are the Stokes parameters, and θ, α and Δ are the angles of the compensator and analyser with respect to the transmission axis of the analyser, and the retardance of the retarder, respectively. Using a PBS, the transmission axis is set horizontally, so $\alpha = 0$ and the retardance of the QWP is $\Delta = 90°$, so

equation 5.1 reduces to

$$I(\theta, 0, 90) = I(\theta) = \frac{1}{2}[(S_0 + S_1/2) + \frac{S_1}{2}\cos 4\theta + \frac{S_2}{2}\sin 4\theta - S_3\sin 2\theta]. \quad (5.2)$$

The acquired intensity is therefore a Fourier series of frequencies in θ, whose coefficients are determined by the normalised Stokes parameters of the light. Using a PM100 powermeter as a detector, Figure 5.3 shows an example dataset of the intensity of the probe beam before the cell, in order to initially calculate the Stokes parameters.
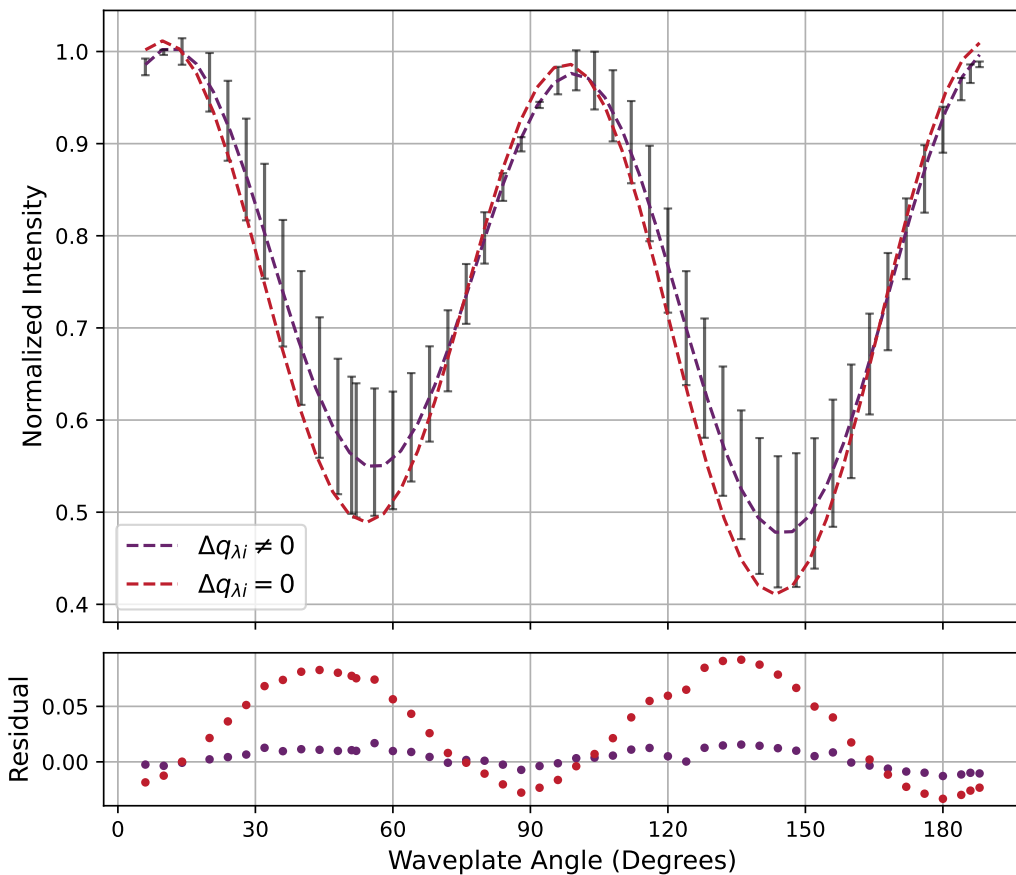

Figure 5.3: Normalised transmitted intensity of the probe beam through a QWP and PBS, as a function of QWP angle. The red dotted line shows a fit, not including a phase difference parameter, whilst the purple dotted line shows a fit including it. The bottom pane shows the residuals of the model from the data. The extracted Stokes parameters were $S_0 = 1.00\pm0.03$, $S_1 = 0.90\pm0.04$, $S_2 = 0.63\pm0.04$, $S_3 = -0.08\pm0.02$, whilst the phase difference parameter extracted was $\Delta q_{\lambda i} = 80°$.

By fitting a curve determined by equation 5.2 to the data, the Stokes parameters can be extracted as parameters of the fit. In this particular data set, the wave-plate angles were set manually, for a total of 3 repeat measurements - the error bars show the standard error on the mean, and are relatively large, likely due to the length of time over which the measurements were taken, resulting in a drift of the polarisation state through a fibre for these early measurements before this was optimised. The extracted Stokes parameters were: $\{S_0 = 1.00 \pm 0.03, S_1 = 0.90 \pm 0.04, S_2 = 0.63 \pm 0.04, S_3 = -0.08 \pm 0.02\}$. It also possible to account for a phase difference due to the mismatch of the wave-plate wavelength and the laser wavelength, as in [111], by modifying equation 5.2 with a phase difference parameter, $\Delta q_{\lambda i}$. The purple dashed line shows a fit including the phase difference term as a fitting parameter (equalling $80°$), which shows better agreement with the data. The difference was likely because a waveplate with centre wavelength, 780 nm was used, rather than centred on 852 nm.

These initial measurements were useful to "clean up" the polarisation - because the light was not purely linear, it was diagnosed that the dichroic mirror before the cell was imposing some rotation of the light due to stress induced birefringence, which was improved by changing the mirror mount. Knowledge of equation 5.2 can also provide some intuition that can quickly give information about the polarisation state. For example, the component containing S_3 oscillates at a different frequency - so any circular component to the light will introduce an asymmetry between adjacent peaks/troughs.

Once the initial polarisation states for each beam were determined, we could then add QWPs to each beam path, in order to rotate the light to the desired polarisation states to perform the investigation. To be rigorous, we also wanted

to confirm the resultant polarisation states at each angle of the QWPs. However, using the manual method described above would be time consuming to perform for every different polarisation state, so a *Thorlabs* PAX1000 polarimeter was also used. These devices work by the same rotating waveplate method, with a rotating QWP and linear polariser inside an internal housing that samples the Stokes parameters using a fast Fourier transform (FFT) at sample rates of up to 400 Hz, due to the rotation speed of the waveplate being up to 200 Hz, and a full measurement being performed between 0°–180°. Reading out data from the PAX1000 via Python, in combination with an automatic rotation mount allowed for a complete profile of the polarisation of the 852 nm and 843 nm beams at the position of the cell, as the QWP was turned, to be performed in a matter of minutes rather than hours.

Figure 5.4 shows the results of these polarisation profiles, across 3 repeats each. The 843 nm light at 0 degrees on the rotation mount was initially almost fully right-handed circular, as S3 is almost 1 and S1/S2 are 0. At 45 degrees, the light was almost perfectly vertical, as S1 was almost -1, and S2/S3 were 0, and then again at 90 degrees, S3 reached -1, and S1/S2 were zero, meaning the light is left handed circularly polarised. We then chose these 3 angles on the rotation mount, to make the light left handed circular, vertical, and right handed circular respectively, such that it would drive transitions corresponding to those polarisations most efficiently. Similarly, the angles 45.63 °, 96.18 ° and 145.63° were chosen for the wave-plate in the 852 nm beam path, to select those same polarisation states, albeit with less purity than the 843 nm, due to the dichroic mirror in the path.

As the QWPs used in the PAX1000 polarimeters are wavelength dependent, they have a limited operating wavelength range, meaning our model couldn't
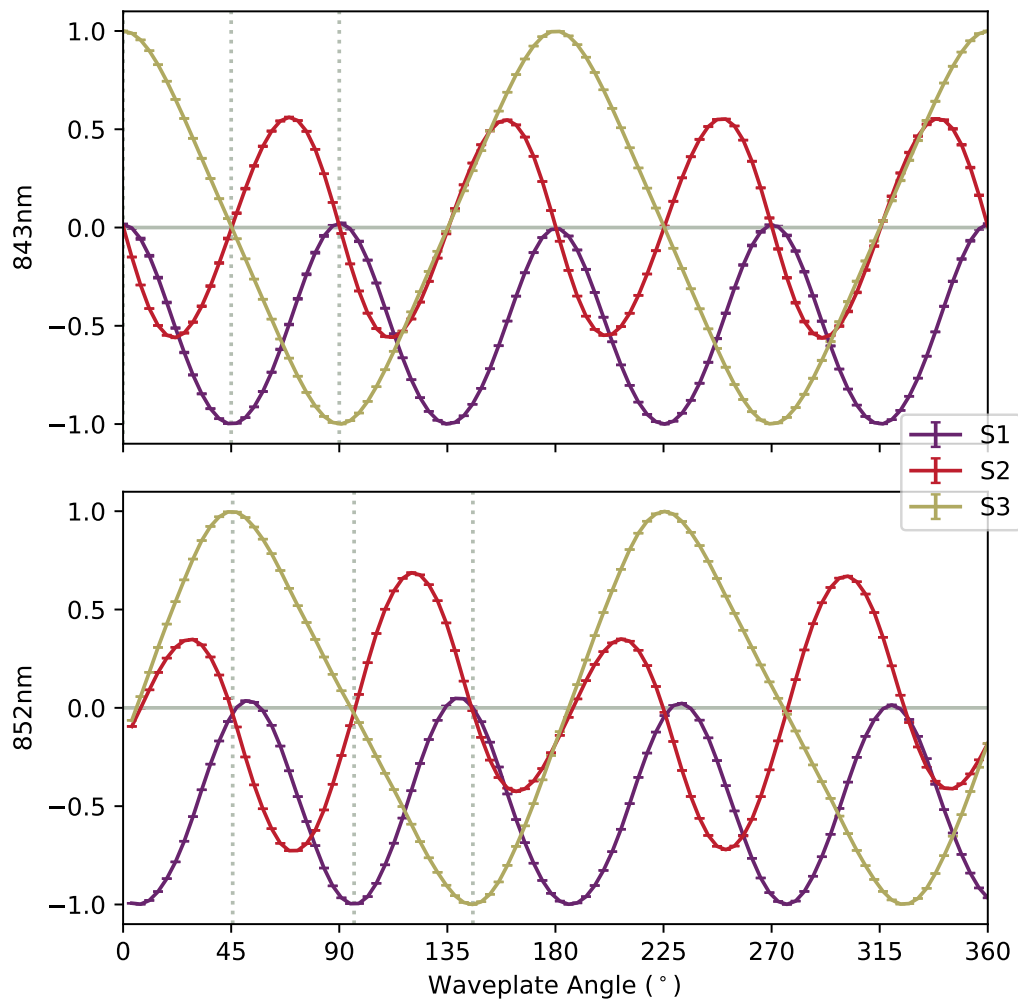
Figure 5.4: Normalised Stokes parameters for the probe and Rydberg beams. The measurements are an average of 3 repeat measurements, with the error-bars representing the standard error on the mean. The dotted vertical lines indicate the angles for each waveplate that were chosen, to provide left handed, linear and right handed circular light respectively (the dotted line at 0 degrees for the 843 nm beam is not visible).

be used with the 1470 nm light. Instead, to quickly determine the desired wave-plate angles, the light was input into a PBS and the transmitted and reflected light monitored with a powermeter. The optical power from each path is plotted in Figure 5.5, as a function of the angle a WPQ10ME-1550 waveplate was rotated to. When the light is almost wholly circular, the power in each arm is roughly equal, as at 67.37° and 157.36°, and when the light is almost wholly ho-
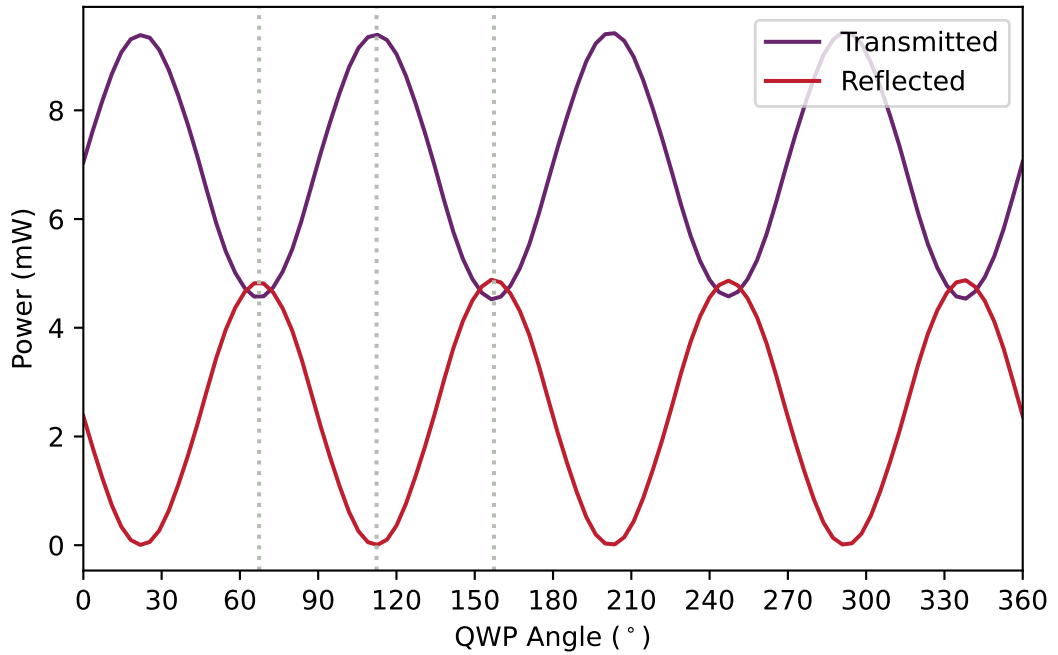
Figure 5.5: Recorded power transmitted and reflected through a PBS for the coupling laser beam just before the cell, as a function of QWP angle. The axes of the waveplate were determined by the maxima and minima of these curves, and the angles used in the experiment are shown by the dotted lines.

rizontal/vertical it is almost wholly transmitted/reflected as at $112.36°$. It was then inferred from the atomic response as to the handedness of the light.

5.2.2 Results

With the polarisation states of each of the 3 beams well established, it was then possible to experimentally investigate the optimal configuration for fluorescence imaging. We again want to measure, $F_{\text{sig}} = F_{\text{On}} - F_{\text{Off}}$, the signal fluorescence signal, whilst varying the polarisation using automatic rotation mounts with QWPs fitted, to the 3 angles each defined in the previous section, to correspond to right circular, vertical and left circular polarisations. The geometry of the system, shown schematically in Figure 3.4, dictates the selection rules that determine the dipole allowed transitions between hyperfine m_F levels -

in this instance, a quantisation axis was set with a magnetic field in the positive z-direction, collinear with the laser beams. In this geometry, the allowed transitions are ones in which $\Delta m = \pm 1$, corresponding to sigma-transitions. It can be inferred that a photon from the Rydberg laser (which is travelling in the positive z-direction) will excite σ^+-transitions if it is left circularly polarised, σ^--transitions if it is right circularly polarised, and a superposition of both σ^+ and σ^- if it is linearly polarised (as linearly polarised light can be described as a superposition of left and right circularly polarised). Oppositely, the probe and coupling beams (co-propagating with the quantisation axis) excite σ^--transitions if they are left circularly polarised, σ^+-transitions if they are right circularly polarised, and both if they are linearly polarised. We will refer to the specific configurations of polarisations of each beam as e.g, ($\sigma^+, \sigma^-, \sigma^\pm$), from hereon, referring to the first, second and third step laser light respectively, and where $\sigma^\pm$ refers to the linearly polarised case where both transitions can occur.

Figure 5.6 shows a schematic of the excitation scheme, decomposed into the hyperfine levels, labelled with quantum number F, and the degenerate hyperfine magnetic sublevels, labelled by quantum number m_F. Each atomic level consists $(2J+1)$ hyperfine levels, of which each is composed of $(2F+1)$ magnetic sub-levels. The most efficient way to populate the Rydberg level should involved population transfer to sublevels where the line-strengths for excitation are the largest. The line strengths were calculated using the Wigner-Eckart theorem [66] for coupling of angular momenta (see section 2.1.2 and equation 2.40)), as the square of the electric dipole moment for each transition and normalised to the weakest transition in each set of transitions between states. We have assumed coupling to the $|14P_{3/2}, F = 5\rangle$ state from the $|7S_{1/2}, F = 4\rangle$ state for simplicity, though in reality the hyperfine components are not resolved within the Doppler width of the transition, and so a change of basis
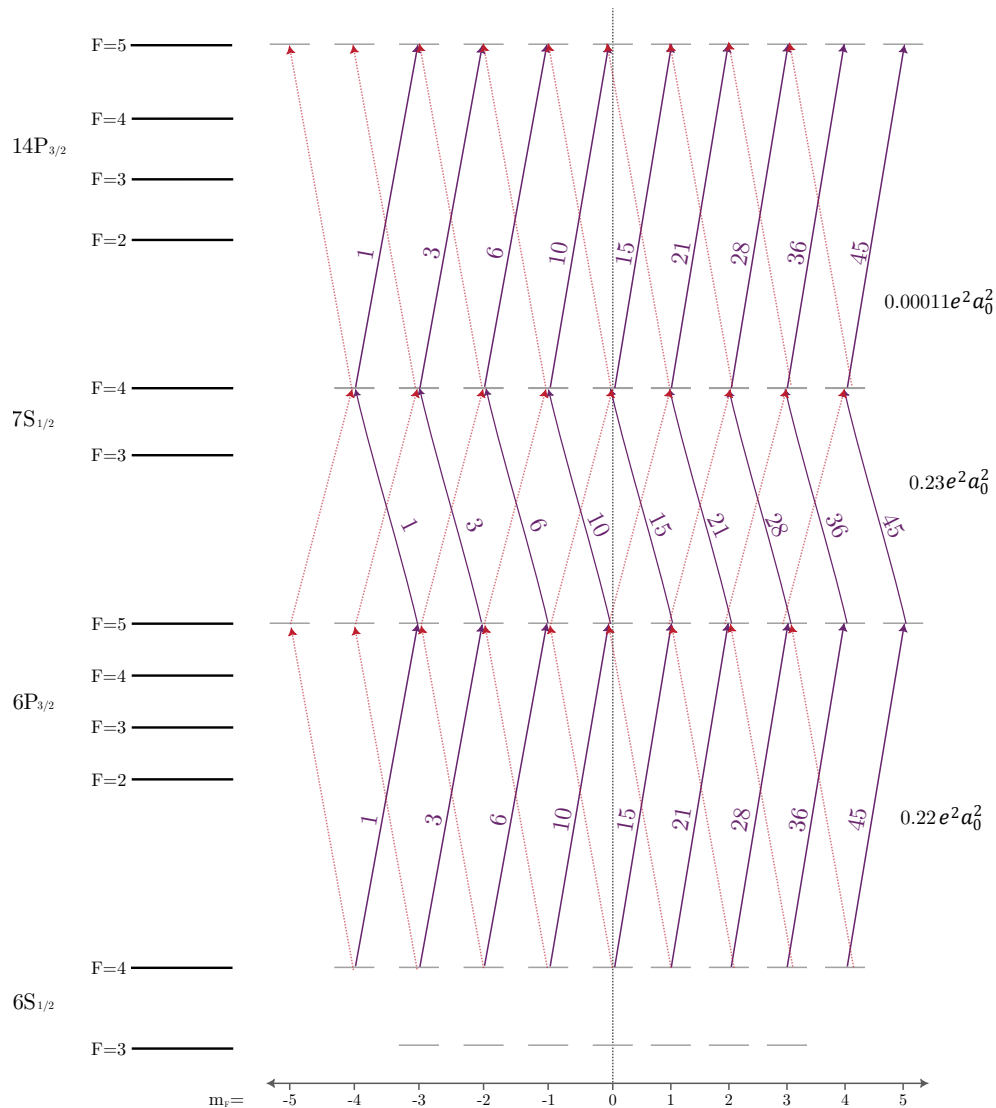
Figure 5.6: A schematic diagram for the levels involved in the 3 laser beam excitations. The overall levels are labelled on the left, decomposed into each of the hyperfine levels, labelled by quantum number, F. The degenerate magnetic m_F sub-levels are plotted out on the right hand side, and the transitions between them are denoted by arrows. The purple arrows represent σ^+, σ^- and σ^+ transitions going up. The opposite handed transition strengths can be found by symmetry, and these transitions are labelled by the dotted red arrows. The relative transition strengths associated with each transition are labelled next to the arrows, and are multiplied by the factor on the right, which represents the squared dipole matrix element of the weakest transition in each set of transitions.

Table 5.1: Table containing the lifetime, natural linewidth, and approximate driving Rabi frequency up to each state in the ladder scheme.

State	Lifetime, τ	Natural Linewidth, $\Gamma/2\pi$	Typ. Rabi Frequency, $\Omega/2\pi$
$6P_{3/2}$	30.4 ns	5.2 MHz	41 MHz
$7S_{1/2}$	48.2 ns	3.3 MHz	43 MHz
$14P_{3/2}$	3835 ns	0.04 MHz	6.8 MHz

would likely be required to describe the transitions.

Table 5.1 shows the typical decay lifetimes, and excitation Rabi frequencies for each state. In order to consider the effect of optical pumping, we must consider how many photons an atom can absorb and emit in the interaction area of the beam. The shortest transit time possible would be for an atom crossing the beam at right angles. The most probably speed for an atom in a Boltzmann-distributed gas is $u = \sqrt{\frac{2k_B T}{M}}$, where T is the temperature, M the mass, and k_B is Boltzmann's constant. For caesium this corresponds to u=191 ms^{-1}. For the 0.64 mm diameter beam, the most probably transit time is therefore 3351 ns, which is more than sufficient time for an atom to undergo the multiple excitations and decays to transfer to extreme sublevels, if we consider the photon scattering rate to be (in the high intensity limit) approximately half the linewidth. For example, this transit time equates to more than 100 lifetimes for an atom in the $6P_{3/2}$ level.

Figure 5.7a shows the experimental results for the procedure described above, with 190 repeat measurements. The 3 panes, from left to right, represent the polarisations of the probe beam (σ^+, $\sigma^\pm$, σ^- respectively), and each individual grid further decomposes into the configurations of the coupling and Rydberg laser polarisations. The numbers represent the fluorescence signal, F_{sig}, averaged over the beam area, then averaged over 190 repeat runs of the experi-
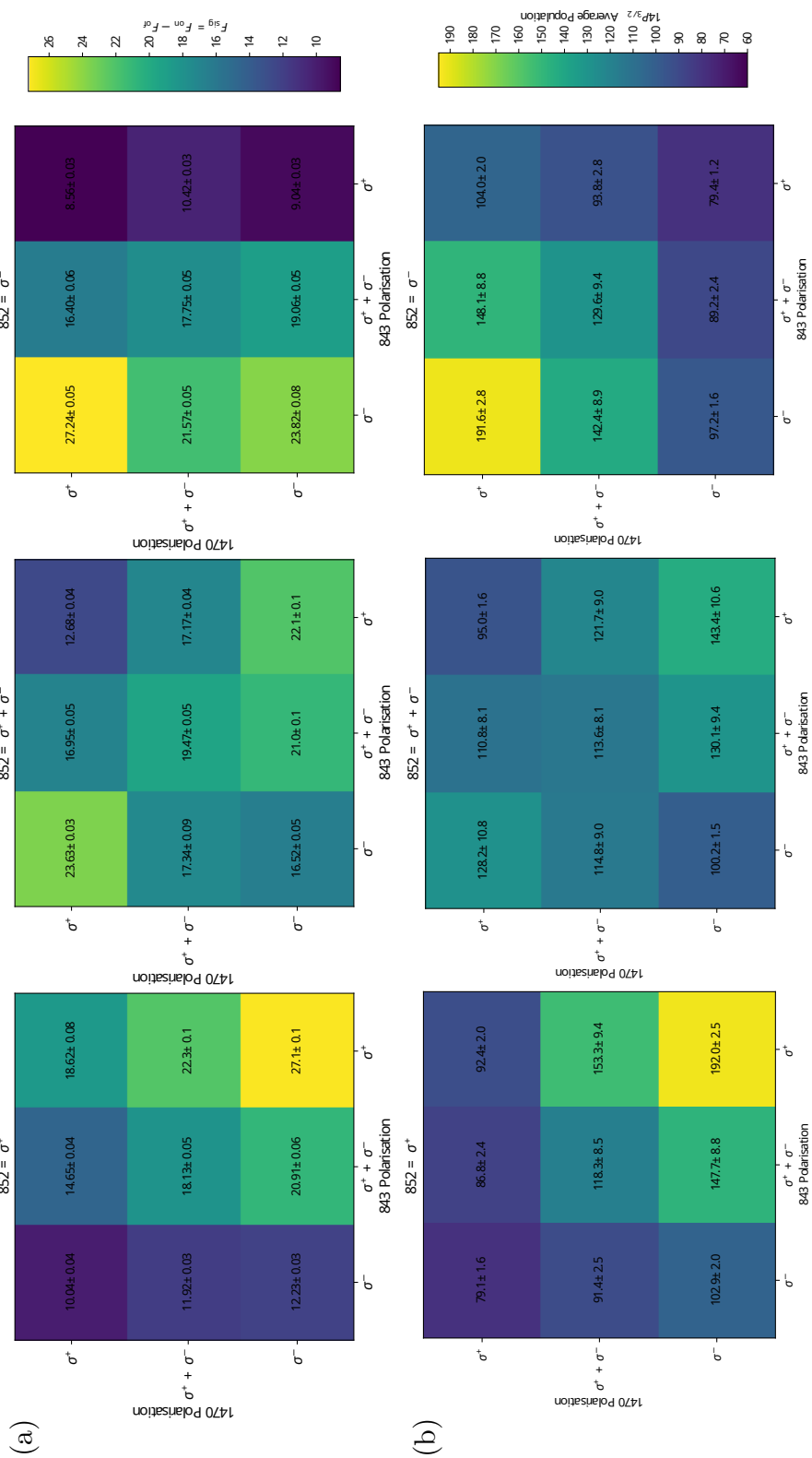
Figure 5.7: (a-c) Colourmap showing the configurations of the probe beam (σ^+, $\sigma^\pm$, σ^- respectively), and each individual grid shows the simultaneous configurations of the coupling and Rydberg laser polarisations. The colour and numbers match up, and represent the fluorescence signal measured, whilst the errorbars are the standard error on the mean across 190 repeat measurements. (d-f) Results from a simulated Monte-Carlo model. The colour bar in this case represents the percentage of population in the $14P_{3/2}$ level, and the errorbars are the standard error on the mean across 30 repeat simulations.

ment. The errorbars represent the standard error of the mean for the 190 runs. The exposure time of each shot was 50 ms, and the power in each beam was 130 mW, 10 mW and 3.5 mW respectively. The cell was at room temperature for these measurements.

The results show that indeed, the configuration with the largest signal values are those that involve pumping on the strongest transitions, either $(\sigma^+, \sigma^-, \sigma^+)$ or $(\sigma^-, \sigma^+, \sigma^-)$. These configurations led to a $\sim$38% increase in fluorescence compared to $(\sigma^\pm, \sigma^\pm, \sigma^\pm)$. In these configurations, population is driven towards the extreme m_F states, and preferentially carried up the ladder on the strongest lines. Comparatively, the weakest signals are obtained when two consecutive beams in the ladder drive the same sense transitions, and the other drives the opposite, e.g, $(\sigma^+, \sigma^+, \sigma^-)$. It is clear, by looking at Figure 5.6, why this is the case - the initial beam drives population towards the extreme m_F and $m_F' = m_F + 1$ state, which appears dark to a second beam driving the same transitions, as there are no dipole allowed transitions in the level above that, so population becomes trapped between the lower levels, and never makes it to the Rydberg level. By symmetry of the line strengths about $m_F = 0$, the same occurs in the opposite sense. A simple model based on the relative line strengths of each transition could help to qualitatively describe this.

Using a simple Monte-Carlo model, some of the general qualitative features of the experimental data could be replicated, as shown by figure 5.7b. We consider only a closed system consisting of the sublevels shown in Figure 5.6. We account for excitations between individual m_F states, with probabilities determined by calculated line strengths, multiplied by some factor to represent the power. An atom can also randomly decay by any allowed path, weighted by the line strengths. We again assume coupling to the $|14P_{3/2}, F = 5\rangle$ level to

remain as simple as possible and avoid mixing in m_J states, as the dynamics should be similar. We start with 100 atoms in each ground state m_F state, as an approximation to a system in thermal equilibrium. In this sense, we also make the assumption that the hyperfine m_F sublevels are totally degenerate, which is valid experimentally as we attempt to cancel any unwanted magnetic field that could create non-degeneracy. For every time step in the simulation, an atom has a chance to excite or decay on each level, providing there is an atom in that level, and that there is a dipole allowed transition for it to make. After a certain number of time steps (in this case of Figure 5.8, 1000), the simulation stops, and the percentage of atoms in any of the final m_F states is recorded. As the coupling via the THz field to the $|13D_{5/2}\rangle$ level is not varied in this experiment, we assume it to be independent of the signal strength in this instance, and take the population of the initial Rydberg level as a proxy for signal strength. The simulation is then repeated 30 times, and the resultant average and errorbars represent statistics on these repeats.

Fair agreement is found between the simulated $14P_{3/2}$ population and the experimentally obtained signal value, though there is better agreement with the F_{off} values (not shown). Discrepancies in the model compared to the data, for example in the underestimation of the $(\sigma^-, \sigma^-, \sigma^-)$ configuration or the overestimation of the $(\sigma^-, \sigma^+, \sigma^+)$ configuration can be attributed to the effect of the THz field polarisation, which is not accounted for in the model. This is because, whilst the THz polarisation was not varied, the differing resulting Rydberg level population distributions may be excited more or less efficiently to the THz-coupled level. Attempting to model the THz field as exciting different fixed transitions ($\Delta m = 0, \pm 1$) could not replicate the data, as a non-trivial mixture of transitions were likely occurring due to the alignment of the incoming THz beam. It also important to note that the actual percentage pop-
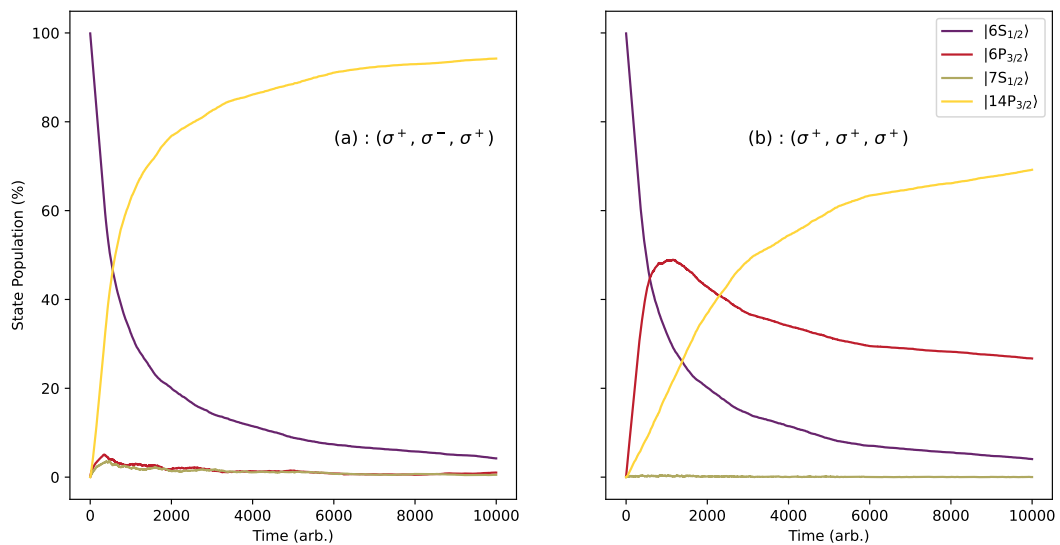
Figure 5.8: (a) and (b) show the extracted populations of each level over simulated time, for two different polarisation configurations, (a) $(\sigma^+, \sigma^-, \sigma^+)$ and (b) $(\sigma^+, \sigma^+, \sigma^+)$. (a) shows the most efficient population transfer to the Rydberg state, whereas (b) shows that population ends up trapped in the extreme m_F sublevels of the $6P_{3/2}$ level. In reality, the populations would not transfer with such high fidelity due to dephasing and decay effects.

ulations calculated by the model are non-physical as dephasing processes and the use of continuous wave lasers prevent such high fidelity population transfer, however the model simply illustrates the effect of individual transition linestrengths.

To conclude this subsection, the results found determined that, as expected, a pumping scheme using circularly polarised light when a quantisation axis is known, to induce sigma transitions, gives the largest fluorescence signal in comparison to other polarisation configurations, with an approximate 38% increase compared to the standard all-linear configuration. Without knowledge of a quantisation axis, however, it would not be clear as to which transitions are being driven, and so there may not be as much to gain, given that some configurations produce less signal overall.

5.3 Effect of Rydberg laser detuning on fluorescence emission

Due to the work done in Chapter 4, to lock the Rydberg laser, we were also able to tune the setpoint of the lock in order to tune the frequency. This opened up the possibility to investigate the effect on the fluorescence of the 3rd step laser detuning, which we will dissect in this section.

We will firstly investigate the effect of the final step detuning on the spectral decay using the *OceanOptics* spectrometer. Interesting effects have previously been seen through spectral fluorescence analysis, such as decay lines that originate from states that are not predicted by dipole allowed transitions [71], likely meaning there is collisional population transfer. Decay lines whose behaviour changes with temperature have also been observed. We therefore probe the system with a new tool, by changing the Rydberg laser detuning.

We collect the light in Experiment 'A' from the cell by clipping an SMA fibre in place on the camera side of the cell, with a *Thorlabs* FESH0750 low pass filter attached, to avoid collecting the high intensity scattered IR laser light. The SMA fibre is directly coupled to the spectrometer, which is USB interfaced with the lab PC. Python could then be used to scan the Rydberg transition via the *Arduino* microcontroller, whilst taking measurements. An initial "dark" measurement was taken at the start of every data run, whereby the Rydberg laser was detuned far away from resonance, in order to eliminate any unwanted background light. This dark count was then subtracted from the measured spectra, in order to give a zero background.

The on resonance spectrum is shown in Figure 5.9. We use the peak-finding al-
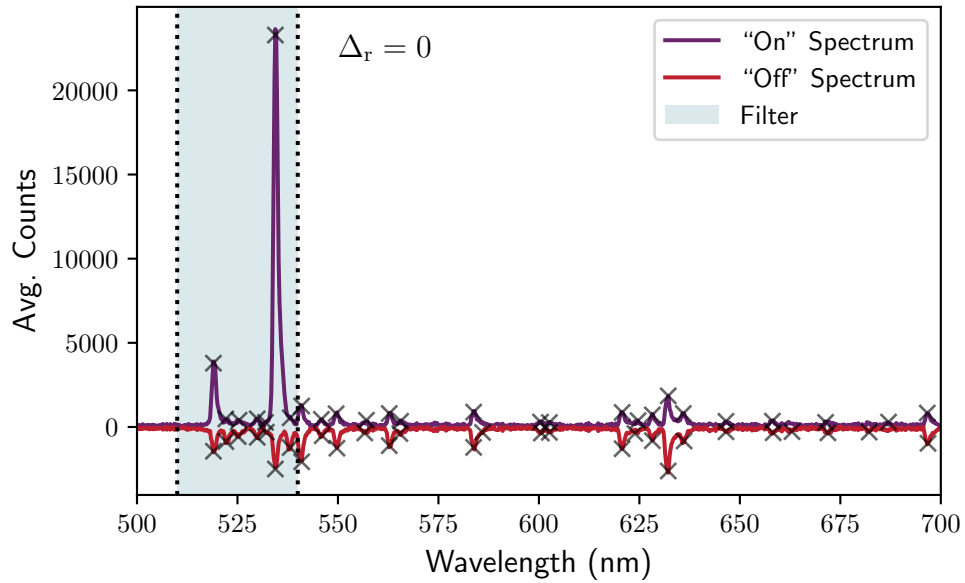
Figure 5.9: Spectrometer trace taken with 200 ms exposure, of fluorescence when the THz source is on in purple above, and off in the red, in inverse. The Rydberg laser is taken to be on resonance as this is where the 535 nm decay peak is the largest. Each detected peak above a certain threshold is labelled with a cross.

gorithm, `find_peaks()` from the Python package `scipy`, to detect the location of each decay line, represented by the crosses. This data was taken with the cell heated to $\approx 40°$ C, with spectrometer exposure times of 200 ms, and 5 repeat runs. By scanning the laser around resonance, we acquire Figure 5.10. A vertical slice across the centre returns a subtraction of the two spectra from Figure 5.9. The blue/red lines are those in which the fluorescence increases/decreases when coupled to the $|13D_{5/2}\rangle$ level. The colourbar was chosen on a smaller scale to make the smaller lines visible, but the line at ~ 535 nm is by far the largest in magnitude, which causes the detected wavelength on the spectrometer to broaden.

If we track the spectrometer counts at the wavelengths of each peak, we can form lineshapes of the detected decay light intensity from each level as a function of the Rydberg laser detuning. This method also helps to determine actual
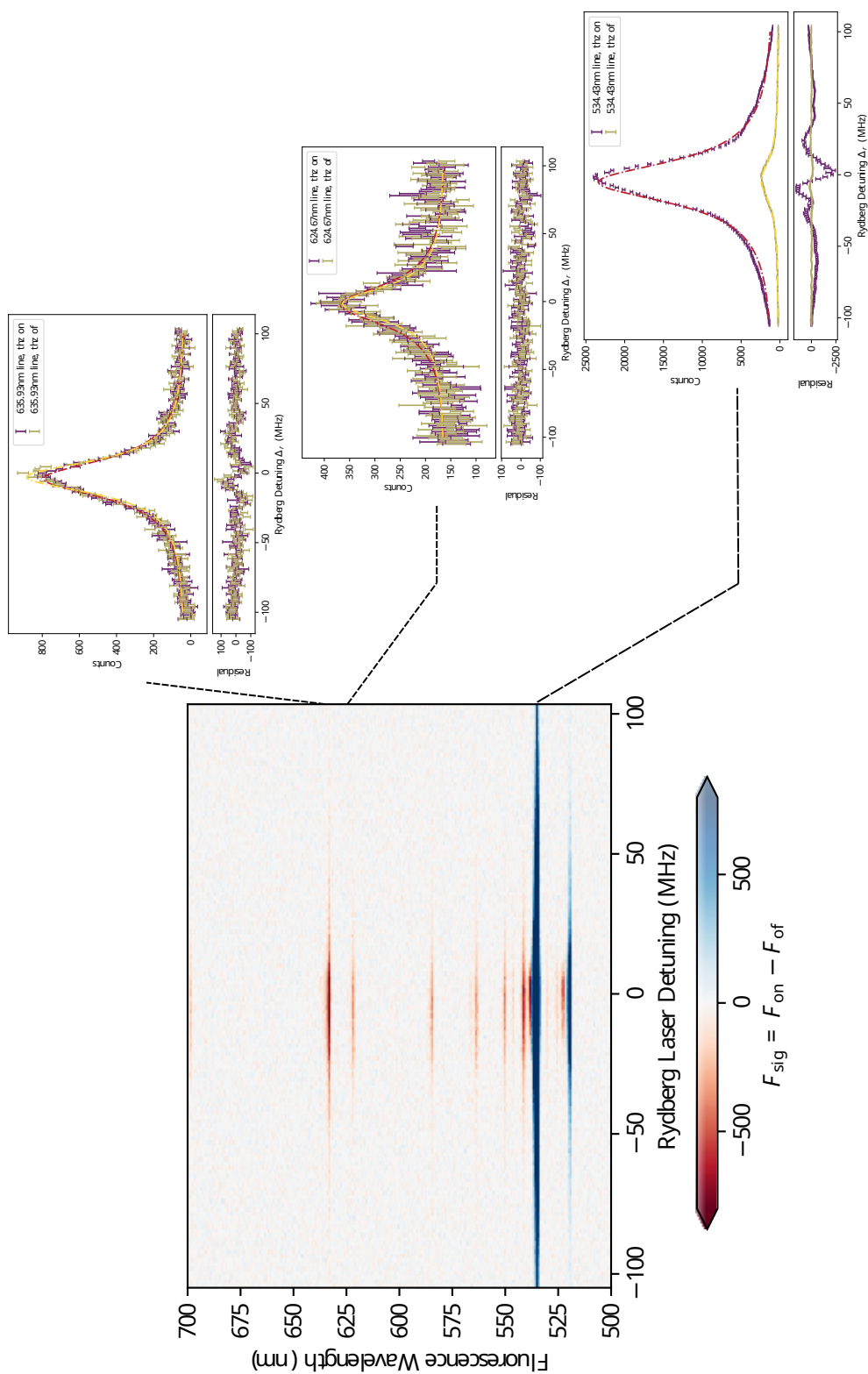
Figure 5.10: Colourmap for the subtracted ("On" - "Off") fluorescence counts, as a function of wavelength and Rydberg laser detuning. A positive value (blue) means the counts are larger when the THz source is on, and a negative value (red) means the counts are smaller when the THz source is on. The colourbar is shown with a restricted axis to highlight the smaller peaks.

decay lines, as spectrometer noise would have no response to laser detuning. Every determined decay line lineshape from these scans can be found in Appendix A. Fitting these decay lineshapes with a Lorentzian lineshape, we find a typical FWHM of around 17 MHz. Most of the lineshapes show reasonable agreement with a Lorentzian fitting, however several of them show some asymmetry, seemingly manifested in a "lean" towards blue detuning near the top of the peaks. The origin of this is not clear. In some cases, it is possible that the line is not resolved, and that there are multiple decays occurring within the resolution of the spectrometer, however it is not obvious how these decays would respond differently to detuning. In general, all the lines show an expected response to the Rydberg laser detuning, but this method is useful for resolving smaller decay lines from noise.

5.4 Effect of THz & Rydberg laser detuning on fluorescence emission

In order to most efficiently populate the $|13D_{5/2}\rangle$ state compared to the $|14P_{3/2}\rangle$, it could be possible that a two photon transition, where we maintain two-photon resonance with the final state, but are detuned from the intermediate state and so do not populate it much, would produce a larger F_{sig} than two on-resonant transitions. This is by the fact that F_{on} would increase whilst F_{Off} would decrease. This two photon resonance condition can be expressed by, $\Delta_1 + \Delta_2 = 0$, where $\Delta_{1,2}$ are the detunings from the intermediate and final state respectively. This results in an effective Rabi frequency,

$$\Omega_{\mathrm{eff}} = \frac{\Omega_1 \Omega_2}{2\Delta_1},$$

where $\Omega_{1,2}$ are the ordinary Rabi frequencies of each driving field. We therefore investigate the detuning of the Rydberg laser and the THz field simultaneously, and their effects on the overall fluorescence levels. We will find that, in fact, the on resonant scenario still gives the largest signal to noise for the subtracted signal, but the detuned case may be useful for detection when the THz power is strong enough to saturate the transition and split the line.

To investigate this, in experiment 'A', the THz source was focussed onto the middle of the cell, and the region of interest was reduced to the central portion of the beam in the cell. The THz frequency was tuned via Python by changing the microwave seed frequency outputted from the *Windfreak* SynthHD, and the Rydberg laser could be tuned via Python with the scanning transfer cavity lock. The THz power was changed by adjusting the UCA voltage in intervals of 0.1 V, and the resultant powers were interpolated from the data in Figure 3.7. This power represents the total output power from the horn, so gives an upper limit for the actual power incident on the region of interest in the cell. Figure 5.11 shows the values of F_{sig} for 6 increasing THz powers. The maximum signal occurs for an intermediate power, at 0.02 mW, where the Rabi frequency is large but not enough to split the line. The line begins with a THz detuning FWHM of about ≈ 16 MHz, and a Rydberg laser detuning FWHM of about ≈ 50 MHz. The natural linewidths of these transitions are 0.19 $2\pi x$MHz and 0.04 2π MHz respectively - clearly these are both initially very broadened. We predict a power broadened linewidth of around 7 MHz for the Rydberg transition [56], which suggests that residual Doppler broadening, and other terms such as collisional broadening contribute more to the overall linewidth. As the overall fluorescence signal is still a combination of various lines, this may also not be a good parameter to measure the linewidths. As the THz power increases, the line broadens and then begins to split, until eventually there is no
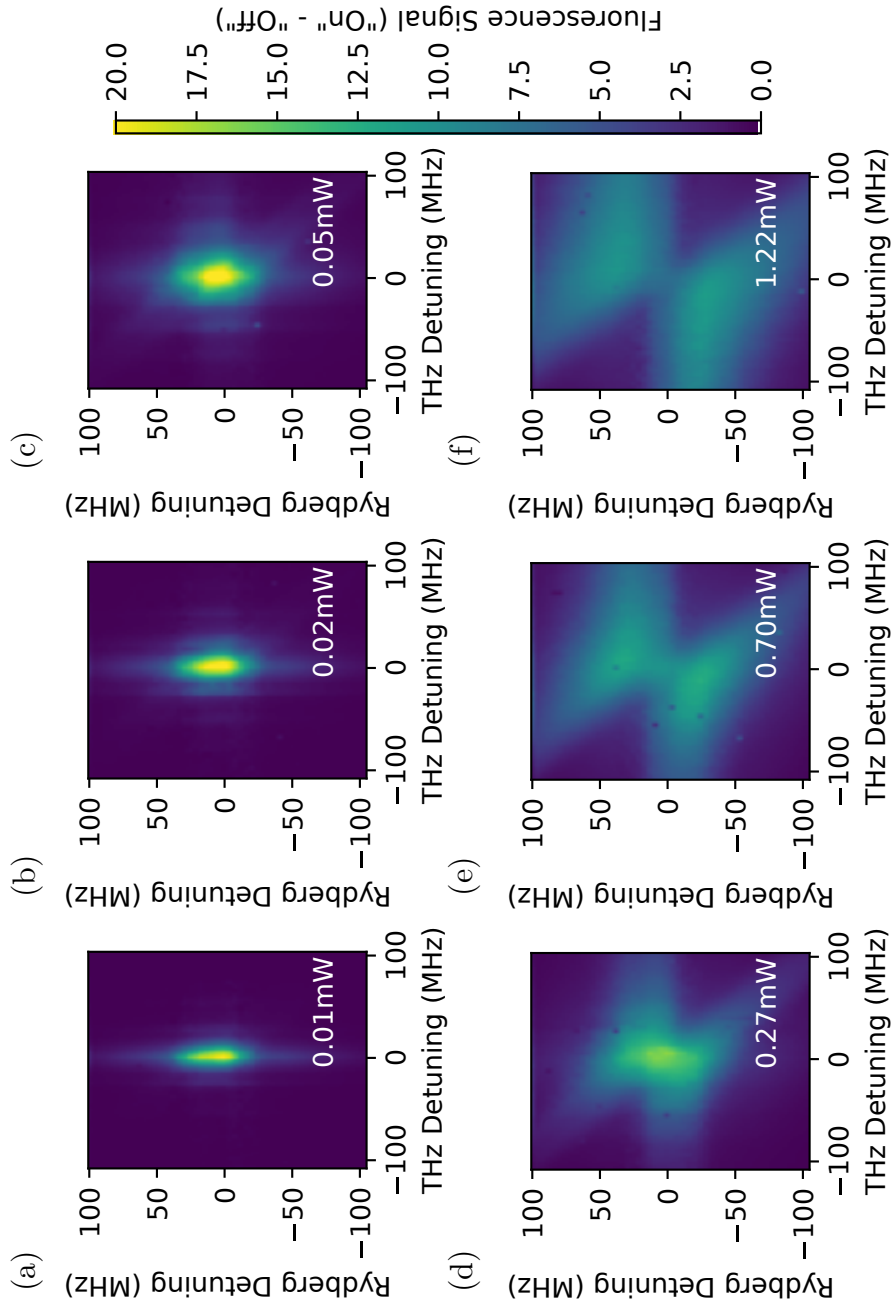
Figure 5.11: The fluorescence "On" - "Off" signal, as a function of THz and Rydberg laser detuning, across increasing THz powers. From top left to bottom right, from (a) - (f), the maximum power onto the cell increases as: 0.01 mW, 0.02 mW, 0.05 mW, 0.27 mW, 0.70 mW, and 1.22 mW. The feature can be seen the broaden and eventually split.

signal at $\Delta_{\mathrm{r,THz}} = 0$. The signal then follows a pattern of an avoided crossing.

In order to model this, a similar 5 level master equation model from previous sections was used. One inconsistency between modelled results and the data was the lack of a diagonal across the data plots corresponding to the two photon resonance condition ($\Delta_{\mathrm{r}} + \Delta_{\mathrm{THz}} = 0$). This was prominent in the model for zero velocity atoms. It was found that incorporating some Doppler averaging due to imperfect wavevector matching reduced the appearance of this diagonal, however. Given that the Rydberg laser was counter-propagating with the first two step lasers, a narrow range of velocity classes around zero, perpendicular to the propagation direction will be resonant with the Rydberg laser. The THz beam was incident in this perpendicular direction, meaning it could be resonant with the whole range of velocity classes, albeit with a much smaller effect due to the lesser magnitude of the wavevector. We incorporated this effect by solving the master equation separately for atoms at varying velocity classes, then taking the total to be the average of each velocity class, weighted by the velocity probability distribution. We assume the velocity of the atoms to follow a Maxwell-Boltzmann distribution and consider 36 velocity classes between -50 m/s and 50 m/s. We make the substitutions

$$\Delta \to \Delta - \vec{k} \cdot \vec{v} \tag{5.3}$$

$$\sigma_{55}(\Delta) \to \int_{-\infty}^{\infty} \sigma_{55}(\Delta, v) f(v) dv, \tag{5.4}$$

where Δ represents the detuning for each field, k is the wavevector for each field, v, the velocity vector described by the velocity class, $f(v)$ is the Maxwell-Boltzmann distribution and σ_{55} is the population in the fifth level. In effect this means solving for the density matrix population element at each velocity class, and acquiring a final result by integrating over the proportion of atoms in each velocity class by the Maxwell-Boltzmann distribution.
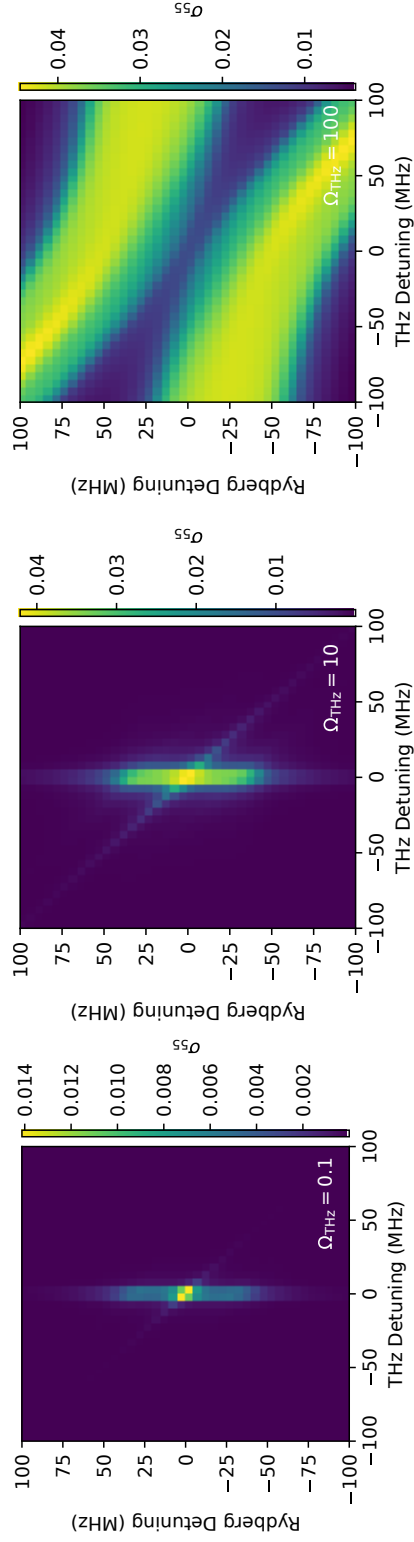
Figure 5.12: Results from a density matrix model to simulate results in Figure 5.11. The colorbar represents the $13D_{5/2}$ extracted population, as a function of THz and Rydberg laser detuning. The THz Rabi frequencies are increased in each pane, as (0.1, 10, 100) x 2π MHz. The model parameters are $\Omega_{p,c,r} = (40,60,6)$ x 2π MHz, $\Gamma_{p,c,r,THz} = (32.71,13.39,0.016,0.0015)$ MHz, $\gamma_{p,c,r,THz}=0.1$ MHz, $\Delta_{p,c} = 0$

Figure 5.12 shows the results of the simulation for three different THz Rabi frequencies, $\Omega_{\text{THz}} = 0.1, 10, 100 \times 2\pi \text{MHz}$. Plotted is the calculated $|13D_{5/2}\rangle$ population, as a proxy for the fluorescence signal. Similar behaviour is seen to the experimental data, whereby the line broadens and then splits, following the avoided crossing. The two-photon diagonal pattern is more prominent still, which suggests there are potentially other dephasing effects that largely eliminate this condition. There is also somewhat of a discrepancy in the populations compared to the experimental signal, as the populations increase with increasing Rabi frequency, which is not reflected in the signal fluoresence in the data. This again could indicate there is some dephasing that occurs at non-zero detuning that is not well accounted for in the model, or that further care is required in relating the defined signal to the population. Nonetheless, we conclude from the data that keeping both the Rydberg laser and THz source tuned resonantly with the two Rydberg states provides the largest signal to noise for our imager. It could still be useful however, that if a THz field of a fixed power out of our control must be imaged (one that is of sufficiently high power to split the line), then a signal can still be extracted by choosing appropriate final step detunings.

5.5 Conclusion

In this chapter, we have characterised the effects various experimental parameters have on the fluorescence signal, F_{sig}, that we measure with our THz imaging system. These parameters include the laser intensities and polarizations, and the final step laser and THz source intensities.

It was found that the optimal laser intensities were a maximised Rydberg laser

intensity, and moderate first and second step intensities. In this system, at a fixed Rydberg power of 120 mW, these were found to be around 2 mW and around 8-10 mW for the first and second step respectively.

It was also found, that the optimal polarisation configurations for each beam were those resulting in $(\sigma^+, \sigma^-, \sigma^+)$ or $(\sigma^-, \sigma^+, \sigma^-)$ transitions, on each step respectively. Assuming that the previous default configuration of all beams being linear led to mostly π transitions, this would be a $\sim 38\%$ increase of fluorescence signal when compared to the default operating polarisations of the imager (or (π, π, π)). However, using light that is circularly polarised in the wrong senses also has the potential to decrease the overall signal, and so may not always be advised.

Finally, the fluorescence signal with both the camera and spectrometer was found to be maximised with both the THz and Rydberg laser on resonance, which was the standard operating parameters. Individual decay lines were found to fit Lorentzians as a function of Rydberg laser detuning with fair agreement, and possibly some unresolved further structure that could be cause for additional investigation. A use case was also determined for detuned light, in the case of a system with high fixed THz power.

The most effective method for increasing the signal to noise of the imaging system, was the implementation of an additional repump laser, which will be the subject for discussion in the next chapter.

Implementation of a repump laser

In this chapter, we will introduce an additional method for optimization of the fluorescence signal, separate to the parameter optimizations of the previous chapter. We will aim to increase the Rydberg population by introducing an additional laser in the form of a ground state "repump". This was found to lead to four-fold increase in the fluorescence signal in some cases. This chapter will discuss how this repump laser, labelled Laser 4 in section 3.2.1, was set up, and the effect of the detuning (sec. 6.1, 6.2.1), the power (sec. 6.1.1), and the input direction of the repump (sec. 6.1) on the fluorescence signal will be investigated. Finally, a measurement of the overall sensitivity to THz power of the imaging system will be made, with the improved effects from the repump laser (sec. 6.2.3).

The ground state of the caesium atom, $6S_{1/2}$, consists of two hyperfine levels, $F = I \pm \frac{1}{2} = 3, 4$, that under thermal equilibrium, are approximately equally populated. These levels are separated by $\approx$ 9.2 GHz, meaning that a single laser cannot address both within its linewidth. In our experiment we typically coupled from the $F = 4$ state upwards with a single probe laser, and so any population in the $F = 3$ state was not addressed by the light - this is known as
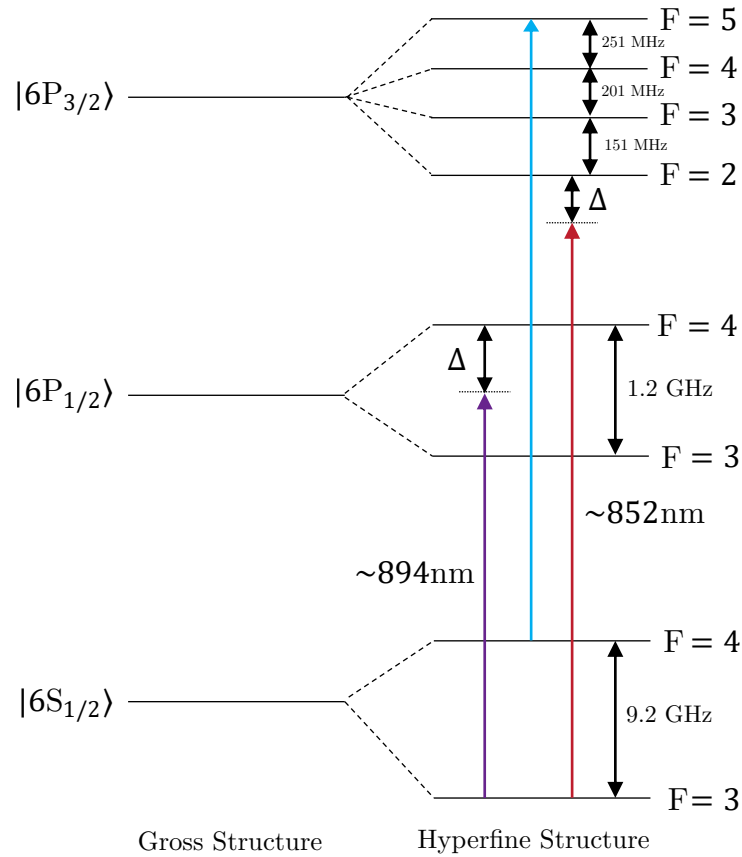
Figure 6.1: A level diagram for the repump transitions. The purple arrow represents the D1 repump transition, detuned by some Δ from the $F = 4$ level, the blue arrow represents the locked probe transition, and the red, the D2 repump transition detuned by some Δ. A more detailed diagram can be found in *Steck* [112].

a dark state. To increase the proportion of atoms in the upper Rydberg levels, we could implement a "repump" laser that pumps population out of this dark state, so that they may interact with the excitation lasers, thereby increasing the average number of atoms that can possibly reach the Rydberg level and decay, contributing to our signal.

Figure 6.1 shows the level diagram for two potential repumping schemes. These two options for the repump transition are the $|6S_{1/2}, F = 3\rangle \rightarrow |6P_{1/2}, F = 3, 4\rangle$ or the $|6S_{1/2}, F = 3\rangle \rightarrow |6P_{3/2}, F = 2, 3, 4\rangle$, known as the D1 and D2 lines, shown by the purple and red arrows respectively. The line strengths differ by

a factor of 2, in favour of the D2 line. We therefore set up a D2 line repump laser in Experiment 'A' to test its effect initially. Once we had those initial results, a repump laser was also set up in Experiment 'B', where a more reliable Titanium:Sapphire laser could be used to look at both lines.

6.1 Implementation in Experiment 'A'

The repump laser in Experiment 'A' was a DFB, described as Laser 4 in Chapter 3. A reference pump-probe spectroscopy arm was set up, using a separate standard 75 mm caesium vapour cell. This consisted of a weak probe beam that passed through the vapour cell, to be detected on a photo-diode. A pick-off prior to this reference was created using a half waveplate and a PBS, which would act as a pump, where the relative intensities of the pump and probe were controlled by the half waveplate. The pump beam was overlapped and counter-propagated with the probe beam, in order to burn holes in the spectrum, and resolve the sub-Doppler hyperfine features. The main beam was then passed through a *Thorlabs* NEL03A/M noise eater, then fibre coupled, to be taken over to the main experimental cell, where it was combined with the probe beam with an orthogonal polarization on a PBS. The frequency could be controlled by altering the current, via the *Thorlabs* Laser Diode Controller. In order to controllably scan over the D2 $F = 3 \rightarrow F' = 3, 4$ transition, whilst taking images of the fluorescence, a USB-6008 was used to output a voltage to the current offset input of the controller. With this method, using one Python script, the offset could be incremented, a THz "On" and "Off" image could be taken, and the reference photo-diode voltage could be read by an input of the USB-6008 in each step, in order to synchronise the measurements. This would result in a triangular scan taking 1-2 minutes. The main disadvantage of this
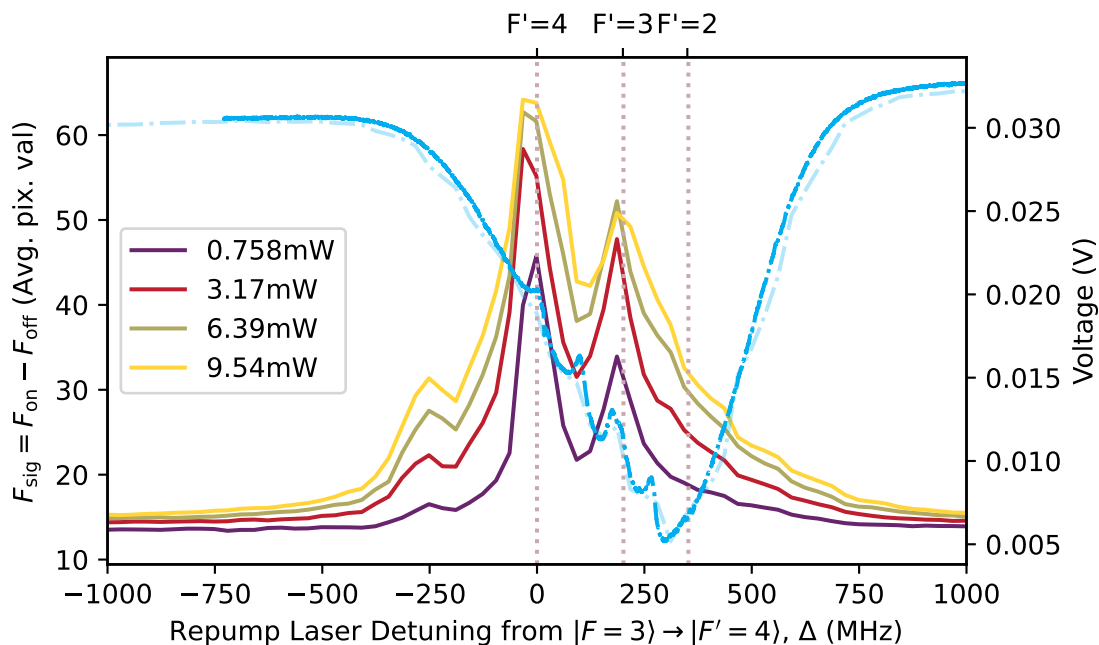
Figure 6.2: The fluorescence ($F_{sig} = F_{on} - F_{off}$) signal, as a function of repump laser detuning and power. The region of interest that was averaged over was the entire beam. The dotted vertical lines indicate the $F = 3 \rightarrow F' = 4, 3, 2$ transitions, from left to right. The frequency axis is scaled based on the reference spectrum, as described in the text. The dashed blue trace shows the overlayed reference pump-probe spectrum, on the secondary axis (right), with some filtering applied to remove noise. The fainter blue line is the original trace that was taken simultaneously with the longer scan.

method was that it was more susceptible to noise, due to frequency drifts during the long scanning time. Because of this, and some issues with optical feedback due to insufficient isolation, a separate spectroscopy reference was also recorded, with the laser scanning quickly (30 Hz), and this was overlaid onto the synchronised data.

Figure 6.2 shows the fluorescence signal response to the repump laser detuning around the D2 line transition, at four different repump laser powers. The probe, coupling and Rydberg laser were set to powers of 1.5 mW, 8 mW, and 110 mW respectively, and images were taken with 25 ms exposure. The frequency axis was calibrated based on the known hyperfine splittings, from the

faster scanned spectrum (the bold blue trace). A linear fit between the data-point number and the frequency distance of each sub-Doppler feature in MHz was made, and the axis was scaled according to the gradient of that fit.

There is a clear and significant increase in the level of the fluorescence signal when the repump is resonant within the Doppler width of the transition, but especially so when it is resonant with the $F = 3 \rightarrow F' = 4$ and the $F = 3 \rightarrow F' = 3$ hyperfine transitions. The signal is at its maximum at zero detuning (≈ 60), and compared to the normal signal when the repump is far detuned (≈ 15) represents a ≈ 4 times improvement. The features broaden and increase in height with increasing repump powers in the range of powers used.

There is also a peak at $\sim$ -250 MHz, that does not correspond to an allowed hyperfine transition, but correponds with the frequency difference between the F=4 and F=5 states. It is likely that this feature appears due to a two photon resonance to the upper levels between the repump and the coupling lasers, when it is driven hard enough. With insufficient repump power (in this case < 0.75 mW), the feature will not appear. It could also be possible that the feature is increased by some Doppler effect, whereby atoms of a certain velocity class are effectively sufficiently detuned to make up the two photon resonance condition.

In order to test this hypothesis, the direction of the repump laser was reversed by combining it on a PBS with the Rydberg laser. This geometry was such that the repump beam was counter-propagating with the coupling laser, leading to some Doppler cancellation, due to the reversal of the repumps wavevector. Figure 6.3 shows the resultant lineshapes, as the repump is scanned over the D2 line in either geometry. The effect is almost identical regardless of the propagation direction of the repump beam, as the two sets of datapoints are relatively
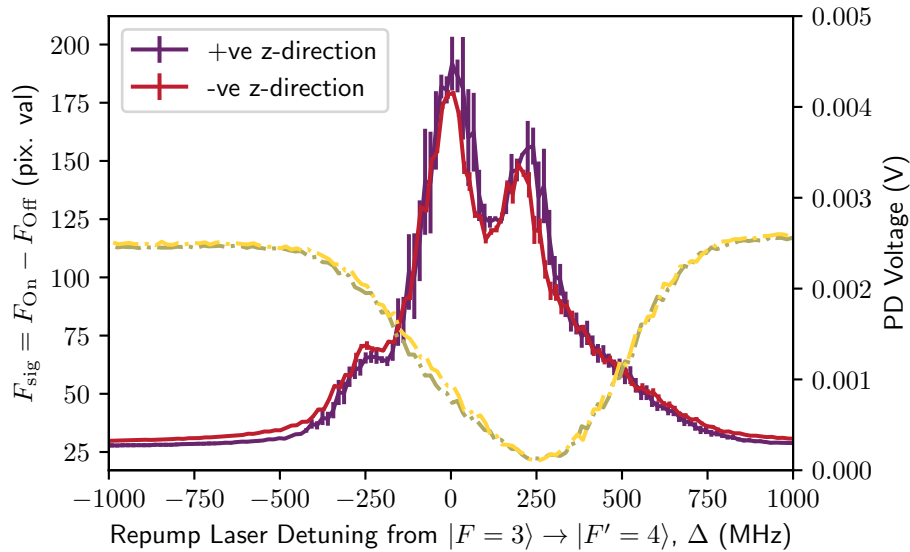
Figure 6.3: Fluorescence signal as a function of repump laser detuning, with propagation in the positive z-direction (opposite to coupling beam) in purple and negative z-direction (parallel with coupling beam) in red. THe errorbars represent the standard error on the mean of 3 repeat measurements each. The dotted traces shows the Doppler broadened reference spectra for each measurement, without a pump beam present, and are represented on the secondary (right) axis. There is little difference in the signal from either direction.

well overlapped. The feature of interest is unchanged, which rules out the a Doppler related effect. This is likely because the velocites required would be too high at this temperature, $\approx 50°$. It is also possible that due to the Rydberg laser being in the counter-propagating geometry, that only atoms in a velocity class with approximately $v = 0$ in the propagation direction would be excited to the Rydberg state, and subsuquently decay to produce a signal.

6.1.1 Probe-Repump Power Dependence Characterisation

As can be seen by Figure 6.2, increasing the repump power led to a further increase in fluorescence signal. It was empirically observed, however, that increasing the repump power beyond a certain value actually led to the fluorescence decreasing across the cell. This likely occurred as the vapour became

optically thick to the probe beam, which would become saturated, and be absorbed within the width of the cell. This would result in the fluorescing region of the cell to become visibly extinguished. This could be counteracted by increasing the probe power in tandem with the repump. As such, we attempted to characterise the dependence of the fluorescence signal on both the repump, and probe laser powers, using the same methods from section 5.1. Figure 6.4 shows the results, with the coupling and Rydberg beam powers at 8 mW and 120 mW respectively.
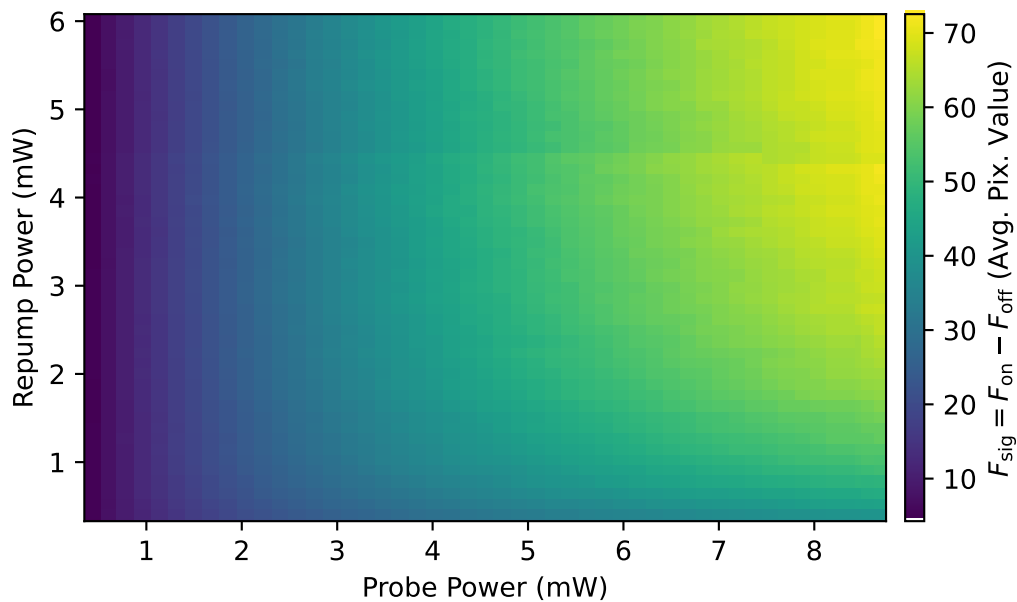

Figure 6.4: Fluorescence signal represented on a colourmap, as function of probe and repump powers. Larger signal values are obtained towards the top right region of the graph, with larger probe and repump powers.

As can be seen in the figure, when a repump beam is present, the probe beam no longer saturates around ~3.5 mW, as in Figure 5.2. Instead, compensating for an increase in repump laser power by also increasing the probe laser power leads to a larger signal. Powers at which this stopped being the case could not be reached using the laser powers available in this experiment. By optimizing the powers according to this principle, an even larger gain in signal could

be achieved, as in Figure 6.3 - a peak signal being ≈ 6.8 times larger than the standard baseline signal. We next look to the D1 line for a comparative measurement in the following section.

6.2 Implementation in Experiment 'B'

In order to excite on the D1 line (894 nm), a different laser was required. We also wished to investigate whether the increase in fluorescence from a collimated beam in Experiment 'A' translated into better images in a light sheet. To this end, we set about implementing a repump scheme in Experiment 'B'.

To excite the D1 line transition, we used an *MSquared* Titanium:Sapphire laser (Laser 4 in section 3.2.1.2), fibre-coupled and combined with the probe beam on a PBS, before any of the beam shaping optics that form the beams into a light sheet. Again, a pump-probe spectroscopy arm was setup before the fibre coupling to provide a frequency reference in the same manner. The frequency of this laser could be tuned to arbitrary wavelengths and locked to a wavemeter. The scanning method was the same as the previous section, whereby an external voltage was applied with an *NI* USB-6008, and images and the reference photo-diode data were taken in steps as the voltage was stepped. A metal mask with a a "psi" cut out was placed in the imaging plane, and imaged onto the vapour, and the region of interest, averaged over to provide a value for F_{sig}, was taken to be a square in the centre of the psi.

6.2.1 Effect of detuning on fluorescence signal

Figure 6.5 shows the fluorescence signal in purple for a frequency scan taken with probe, coupling, Rydberg and repump powers set to 9, 8, 80 and 13 mW
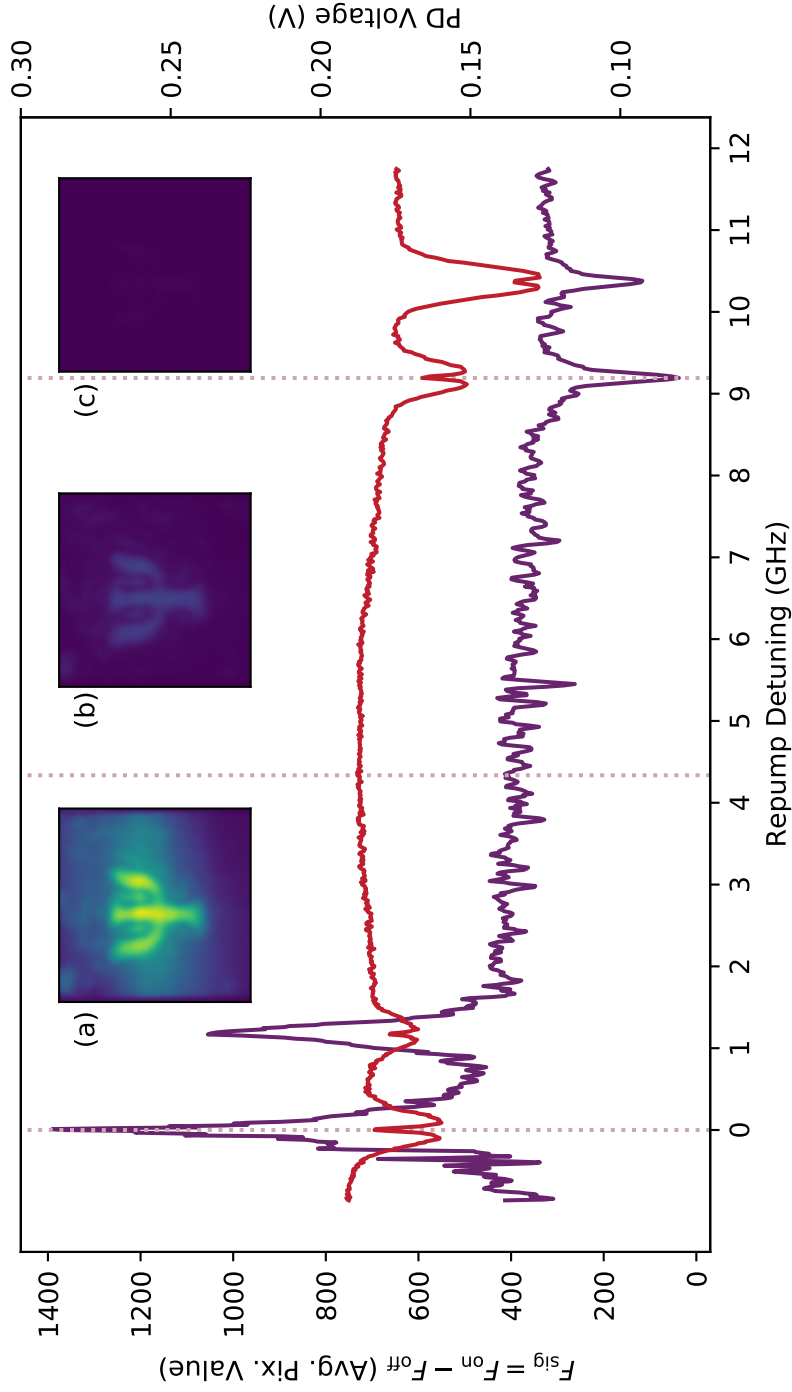
Figure 6.5: Fluorescence signal, averaged over the central region of the "psi", with an exposure time of 25 ms, as the repump laser is scanned over the D1 resonances. The purple trace shows the fluorescence signal, on the left hand axis, and the red trace shows the reference pump-probe spectrum, on the right hand axis. The insets (a-c) show images from the fluorescence, of the "psi" mask, with equal colourbars, at different detunings, indicated by the vertical dotted lines. (a) $\Delta = 0$ GHz, shows the greatest contrast, on resonance with the $F = 3 \rightarrow F' = 4$ transition, (b) $\Delta = 4.34$ GHz shows moderate contrast, whilst (c) $\Delta = 9.18$ GHz shows the worst, on resonance with the $F = 4 \rightarrow F' = 3$ transition.

respectively. As a different camera with a larger bit rate than in experiment 'A' was used, the fluorescence signal values are on a different scale. The frequency was scanned over all four allowed transitions: $|6S_{1/2}, F = 3, 4\rangle \rightarrow |6P_{1/2}, F' = 3, 4\rangle$, with the detuning centred on the $F = 3 \rightarrow F' = 4$ transition. The reference pump-probe spectrum is shown in red.

Similarly to the D2 line data, the largest increase in fluorescence signal was when the repump was resonant with the $F = 3 \rightarrow F' = 4$ transition, whilst resonance with the $F' = 3$ transition resulted in a smaller increase. Interestingly, on resonance with the $F = 4 \rightarrow \ldots$ transitions, there is a decrease in fluorescence signal. At these detunings, the probe and repump lasers address the same atoms, and so the repumping effect is lost and the transition becomes saturated and likely split. This leads to an almost total extinguishing of the signal.

The insets (a-c) show images at the detunings indicated by the vertical dotted lines, taken with identical exposure times (25 ms). Inset (a) shows the resulting image when the repump is tuned to the $F = 3 \rightarrow F' = 4$ transition, (b) shows an image at 4.1 GHz detuning, which is sufficiently detuned from any transition for this to be considered the "no repump" case, and (c) shows an image on the $F = 4 \rightarrow F' = 3$ transition. Clearly, the image in (a) is much brighter and with larger contrast than in the standard case of (b). There is virtually nothing visible at this exposure time in (c).

The experiment could be repeated for the D2 line easily by retuning the Ti:Saph laser. The results for this are shown in Figure 6.6. The same effects are seen as in Experiment 'A'. The signal is more noisy however, as fewer pixels are averaged over in the region of interest in the centre of the "psi", than across the beam in Experiment 'A'. The reference spectrum also looks slightly different, as no care

was taken with regards to the polarizations of the pump or probe beam in the spectroscopy arm. These polarizations govern the anistropy of the atoms, or can induce optical pumping that will distribute the populations around the magnetic sublevels differently [78]. This leads to differing levels of absorption on each transition, and changes the appearance of the pump-probe spectrum. This data was taken with probe, coupling, Rydberg and repump laser powers of 9, 8, 80, and 13 mW respectively. The largest signal at zero detuning is $\approx$ 4.3 times bigger than without the repump. This is less than on the D1 line, however a direct comparison is difficult to make, as experimental parameters such as cell temperature and laser powers may differ slightly. This could be explained by the fact that stimulated emission from $6P_{1/2}$ level increases when the repump is active on the D1 line.

6.2.2 Fluorescence Spectral Analysis

In order to further investigate how the repump laser affects the overall fluorescence signal, we also analysed the spectrum of the emitted light with the methods from section 5.3. Again, the light was collected with a fibre, with a FESH0750 low pass filter applied, as the repump was scanned over the D1 line resonances. Figure 6.7 shows the results, limited to the region around the $F = 3 \rightarrow \ldots$ transitions, with a spectrometer exposure time of 50 ms, where zero detuning is defined relative to the $F = 3 \rightarrow F' = 4$ transition.
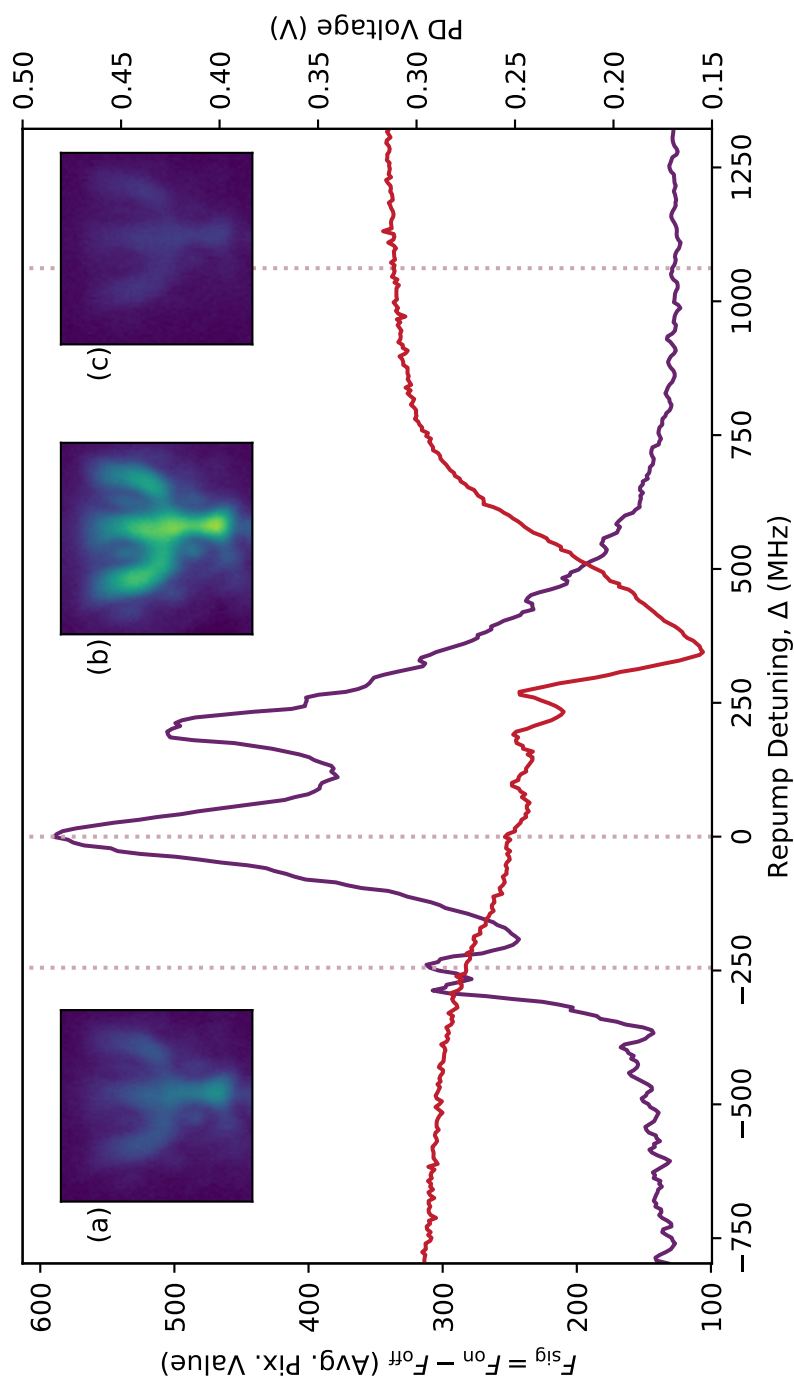
Figure 6.6: The purple trace shows the fluorescence signal averaged over the central portion of the "psi", whilst the red shows the reference pump-probe trace. Images were taken with 25 ms exposure time. The inset images (a-c) show images of the cell at 3 different detunings indicated by the vertical dashed lines - (a) $\Delta = -244.8$ MHz, (b) $\Delta = 0$ Mhz, and (c) $\Delta = 1061.8$ MHz. The image is slightly blurred and non-uniform, as the metal mask was placed slightly too low in the imaging plane.
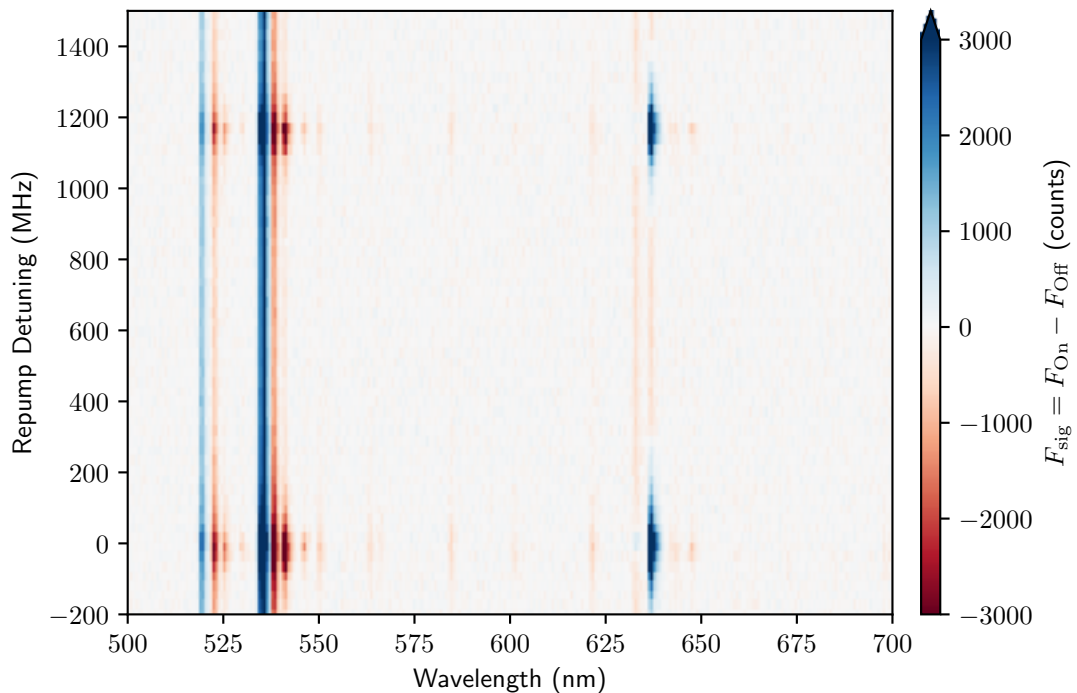
Figure 6.7: A colourmap showing the spectrometer counts of the fluorescence signal, $F_{\text{sig}} = F_{\text{On}} - F_{\text{Off}}$, as a function of repump laser detuning. The colourbar is limited, and the main decay line (at 535 nm) is divided by 4 in order to make the other lines more visible. The x axis shows the wavelength of fluorescence detected, at the repump detuning shown by the y axis value.

For most of the decay lines, applying a resonant repump did not change the behaviour of the line, only increasing the magnitude of the line. We note that, importantly, the decay lines within the width of our bandpass filter $(525 \pm 15 \text{ nm})$ that contribute most to our signal, continue to display the same "On"/"Off" behaviour. The effect of the repump for these decay lines is to simply increase the magnitude of this behaviour.

For example, on the 535 nm decay line corresponding to the $|13D_{5/2}\rangle \rightarrow |6P_{3/2}\rangle$ transition, the F_{On} signal continues to be larger than the F_{Off}, as shown by the darker blue regions around the resonance. Similarly, the 520 nm decay line, corresponding to the $|13D_{3/2}\rangle \rightarrow |6P_{1/2}\rangle$ also shows an increase in F_{sig}. Conversely, for example, the line around 541 nm shows a larger decrease on reson-

ance, meaning there is more decay via this path from the "Off" level than the "On". This line contained two unresolved transitions; the $|12D_{5/2}\rangle \rightarrow |6P_{3/2}\rangle$ and the $|12S_{1/2}\rangle \rightarrow |6P_{1/2}\rangle$.

It would seem that the repump laser has an effect on all lines, due to atoms that would otherwise be 'trapped' in a dark state, being available for excitation, but decays to the $|6P_{1/2}\rangle$ level are those that have the largest response to the resonance of the repump laser - this is precisely the level that the repump excites to. It may be that atoms that decay into this level are cycled more quickly back into the system due to stimulated emission as a result of the repump laser. It is also good to note, that although every decay line increases with the repump, we do not end up increasing the non-relevant fluorescence at the same rate as the signal fluorescence, thereby giving us no increase in signal to noise. The decay lines that result in green signal fluorescence still show a larger increase from the "On" state relative to the "Off", which manifests in a larger F_{sig}. In the imaging system, when the bandpass filter is applied around the green decay wavelengths, the increase in non-signal fluorescence (outside of the bandpass) becomes irrelevant regardless.
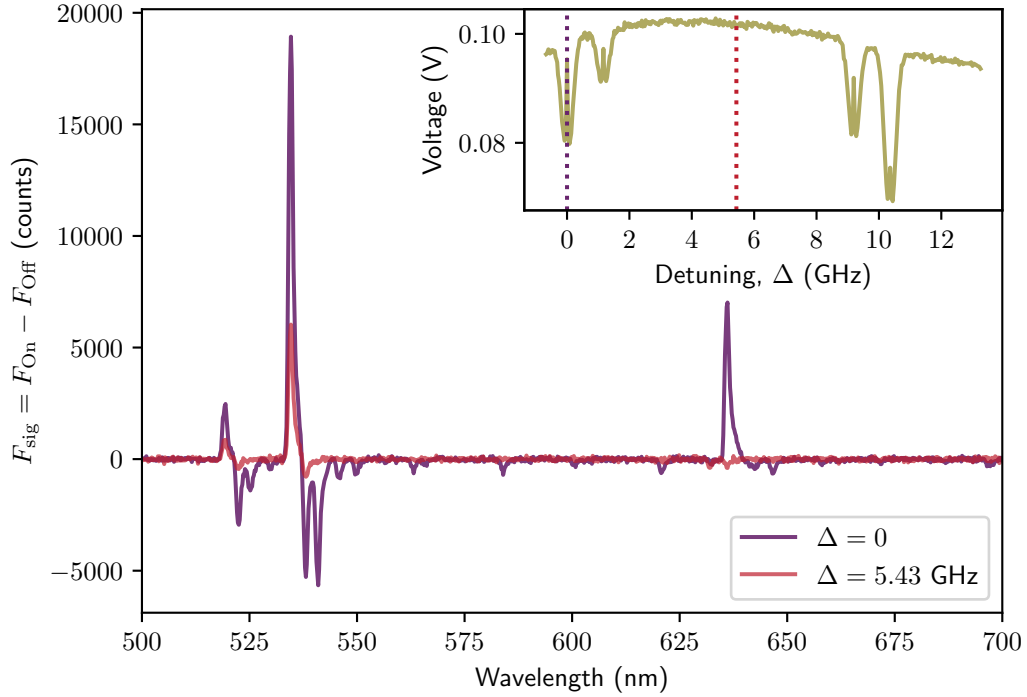
Figure 6.8: THz "On" - "Off" spectrometer measurements (F_{sig}), showing the wavelengths of the emitted photons, at two different repump laser detunings. The inset shows the reference D1 spectrum, where the purple dashed line indicates the detuning of the purple spectrum and the red dashed line indicated the detuning of the red spectrum. The change in behaviour around 636 nm when the repump is resonant is obvious here.

There is a noticeable unique change in behaviour around the 633 nm and the 636 nm lines, as the "On" fluorescence becomes more than the "Off" fluorescence, on resonance, whilst it is the other way round off resonance. Both of these consist of two unresolved transitions - $|10F_{5/2}\rangle \rightarrow |5D_{3/2}\rangle$ / $|14P_{3/2}\rangle \rightarrow |5D_{5/2}\rangle$ and $|10F_{7/2}\rangle \rightarrow |5D_{5/2}\rangle$ / $|9S_{1/2}\rangle \rightarrow |6P_{1/2}\rangle$ for the 633 nm and 636 nm lines respectively. The change in behaviour suggests that the repump causes these transitions to occur more often from the THz-coupled state, $|13D_{5/2}\rangle$, than the initial Rydberg state, $|14P_{3/2}\rangle$, but the effect is stronger for the 636 nm line. This suggests that the population increase in the $13D_{5/2}$ level due to the repump makes it surpass the other decays, but it is not clear why these lines

would be uniquely affected. For the case of the 633 nm line, it could be that the increase in population in the $|14P_{3/2}\rangle$ via the excitation scheme, ends up increasing the decay from this level even when it is coupled with the THz field. For the case of the 636 nm line, it is possible that the $|10F_{7/2}\rangle$ and / or $|9S_{1/2}\rangle$ levels are common pathways in decay from the $|13D_{5/2}\rangle$ level.

6.2.3   Improved Sensitivity Measurements

Another important metric that we wished to optimise was the minimum detectable power (MDP) of the imaging system. The MDP is defined as the minimum THz power where the signal to noise ratio SNR $= 1$, and it often quoted in terms of a power per unit bandwidth [113]. In this case, it is used to provide a measure of sensitivity to compare to other THz detection / imaging methods. The high sensitivity $(190 \pm 30 \text{ fWs}^{-\frac{1}{2}}$ per pixel) [15] of this system was already a boon that allowed for record-high framerates for a THz imager, and with the increased signal-to-noise ratio due to a repump laser, an even higher sensitivity could be possible. We therefore set about measuring an MDP, with and without a repump laser, to determine this improvement.

In order to measure an MDP, firstly the power output of the THz source had to be calibrated. This was done using an *Erikson* PM5 powermeter; the idea being, to measure the THz powers at intervals using the powermeter, and then repeat these measurements inside the system, with the powermeter measurements as a bench mark for the power. This was done by focusing the THz beam onto the detector using a Teflon lens, and taking measurements via a USB-6008 from the analog output voltage of the PM5, to the PC. Typically, we would vary the THz power using the voltage controlled attenuation input to reduce the output power, but this response across the whole range was highly non-linear

(see figure 3.7). This meant that at lower powers, much finer voltage increments were required, and we started to lose out on resolution due to the bit rate of the DAC. The powermeter also operated in different regimes - below 200 μW, below 2 mW, and below 20 mW, with decreasing required measurement times with increasing power. This meant that measuring across the power range of the source could not be appropriately done in one set of measurements. For this reason, another form of attenuation was introduced, in order to stay within the linear region of the UCA response, such that uniform voltage increments corresponded to uniform power increments. This was previously done by introducing Nylon discs into the beam path, of varying thicknesses for varying fixed levels of attentuation [71]. Instead here, we attempted to use commercial *Purewave Polarisers* THz linear polariser elements for attenuation. This method, however, led to some interesting unexpected results, in that it altered the spatial distribution of the beam, which prevented an accurate measurement of the MDP. The process of power calibration, and a discussion of the possible origins of this effect will therefore only be included in the outlook in Chapter 7.

Instead, here we show preliminary results, where the THz power was varied using only the UCA voltage. The THz powers output from the source were then interpolated from the UCA voltages measured using the PM5 powermeter coupled with a waveguide, as in Figure 3.7. These powers were measured using only the 20 mW setting of the PM5 powermeter, which was the least sensitive setting. As a result, the measurements at low THz are likely unreliable. This method was used as this dataset was only intended to provide a quick demonstration of the overall behaviour. Nevertheless, the detected fluorescence signal, F_{sig} is shown in figure 6.9, across this power range, with and without a repump laser, resonant with the $|6S_{1/2}, F = 3\rangle \rightarrow |6P_{1/2}, F' = 4\rangle$ transition.
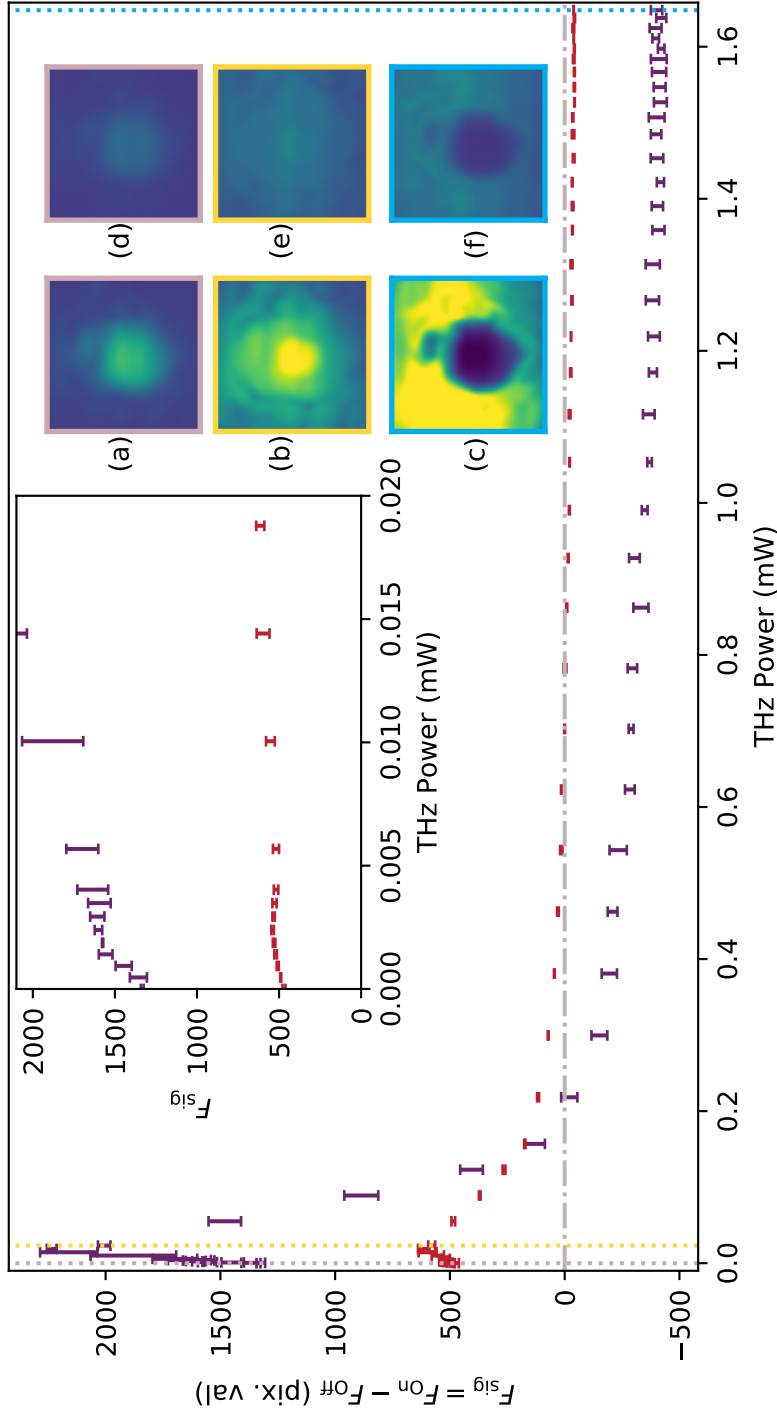
Figure 6.9: Fluorescence signal response to THz power. The purple and red datapoints show the average over the region of interest in the centre of the focused THz beam, with repump on and off respectively. The inset shows the lower power region on a smaller scale. The inset images (a-c) show the images taken at the THz powers indicated by the colour-coded vertical dotted lines, with the repump on, whilst (d-f) show the same for the repump off, with identical exposure times (25 ms). (a) and (d) are taken at the minimum recorded power, (c) and (f) at the maximum, and (b) and (e) at an intermediate 0.014 mW. The dashed horizontal line is a guide for the eye for zero signal.

For this data, the probe, coupling, Rydberg and repump laser powers were set to 9, 8, 80 and 32 mW respectively. This signal was measured by focusing the THz beam, with the same lens as in the powermeter measurements, onto the cell, and taking the region of interest to be the central region of this spot. The images on the right hand side correspond to the F_{sig} (THz "On" - "Off") images, where in the left column, (a-c) the repump is on, and in the right column, (d-f), the repump is off. Each row corresponds to images at different powers, indicated by the color-coded vertical dotted lines.

This results can be analysed in three different sections. At high THz power, shown in (c) and (f), the transition has saturated and the $|14P_{3/2}\rangle$ level has undergone Autler-Townes (AT) splitting due to the intensity of the THz field. This splitting shifts the line away from the original Rydberg resonance, meaning that the region of interest goes dark when the THz is on. When the THz source is off, the line is no longer split, so the Rydberg laser returns to resonance, and there is some "Off" fluoresence. For this reason, in the high THz intensity regime, the "Off" fluorescence is larger than the "On" fluorescence and thus the fluorescence signal, F_{sig} goes negative. For the case where the repump is on, there is even more fluorescence from the "Off" state, and so F_{sig} is more negative.

There is then an optimum signal in the intermediate power regime where there is maximal driving power without beginning to split the line. This regime is shown by (b) and (e). The effect of the repump is also largest at this power (nearly four times the signal). Then, at low THz power, shown also by (a) and (d) there is an approximately linear relationship between the detected signal and the input THz power. In this section, however, there is a large uncertainty associated with the power calibration. This mainly arises from the uncertainty

associated with the interpolation of Figure 3.7 at low THz powers.

For the waveguide-coupled measurements in Figure 3.7, across the 0-4 V range, 31 datapoints were recorded, but 50 datapoints were recorded in this experiment. The calibration therefore relies on a 2d interpolation algorithm to 'fill in the gaps'. Furthermore, ideally, the 200 μW setting should have been used in the waveguide-coupled measurements, to measure the power below this range - in this setting, over 30 seconds per measurement was required to capture 99% of the THz power response, so the 10 s wait times between measurements used were not sufficient to accurately capture the full response above the noise. The culmination of these issues is that, at the UCA voltages used in the low THz power region of Figure 6.9, the THz value has been interpolated to be zero, where in reality, some small THz power would have been measured, with the most sensitive powermeter setting. This is why there is still a significant amount of fluorescence signal still observed, at what has been recorded to be zero THz power. A repeated measurement of this data, following the method described in 7.1.1, where every datapoint has an associated set of powermeter measurements, and concomitant uncertainties, would be much better placed to define a new MDP. Nevertheless, the trend of the data suggests that, at low THz powers, having the repump on significantly increases the signal, and so with more accurate power calibration, a much improved sensitivity could be recorded. A back of the envelope calculation might suggest, that given the ≈ 7 times larger signal, with a similar noise floor, an approximate MDP of $30\,\mathrm{fWs}^{-\frac{1}{2}}$ per pixel could be measured. This estimate does not include the signal gains found by other parameter optimizations.

6.3 Conclusion

In this chapter we have introduced an additional laser to excite on a repumping transition, with the aim to increase the Rydberg population and achieve a larger signal to noise ratio in our fluorescence signal images. The effect on the fluorescence signal of repumping on both the D1 and D2 lines has been characterised by the response to detuning and laser power.

On both the D1 and the D2, it was found that the $F = 3 \rightarrow F' = 4$ transition increased the signal by the most. This transition on the D1 line led to an observed increase of 6.8 times the signal, whilst on the D2 line, a signal 4.3 times larger was observed. On the D2 line, an unexpected peak in fluorescence detuned $\approx$ -250 MHz from this was also found, but its origin was not determined. The increase in signal could be optimised by tuning the powers of the probe and repump lasers relative to each other - if the repump was much higher than the probe, then the transition would saturate and the fluorescence from the upper states would be extinguished, but by also increasing the probe power, an even larger signal could be obtained.

The fluorescence spectrum was also analysed, and it was found that virtually all decay lines showed higher number of counts measured. When measuring the $F_{\mathrm{sig}} = F_{\mathrm{On}} - F_{\mathrm{Off}}$ signal, the main signal decay lines (535 nm and 520 nm) saw a sizable increase in count when the repump was on resonance. Interestingly, the 633 nm and 636 nm decay lines exhibited unique behaviour in that, when the repump was on resonance, the THz "On" fluorescence became larger than the THz "Off" fluorescence, compared to without a repump, where the THz "Off" signal was larger than the THz "On". Finally, promising preliminary results were obtained, when attempting to measure the effect of the repump

laser on the sensitivity of the system, that it could indeed lead to a lower MDP. The increased signal associated with the repump could in future enable even higher imaging framerates.

CHAPTER **7**

Outlook & Conclusion

7.1 Outlook

There were several areas of the investigation in this thesis warrant further study as they came up with interesting unexpected results that could not be characterised fully. In this outlook section, we will present a few of these results, in the interest of opening them up to further investigation.

Firstly, unexpected results that arose from the use of THz polarisers as attenuators will be discussed in section 7.1.1. The work done to calibrate the THz power response to the polariser angle using the PM5 power meter will be shown. It was discovered, however, that when the THz beam was focused onto the cell, the spatial distribution of the field was dependent on the angle of the linear polariser. A possible explanation for this will be described, and preliminary attempts at modelling discussed. Then, in section 7.1.2, we explore effects observed when attempting to vary the vapour temperature. This arose during attempts to continuously characterise the dependence of fluorescence emission on cell temperature. It was found that there was a large spike in fluorescence associated with an increase in temperature, that then reduced back down to a

much smaller level as the temperature settled. The height of this peak was not necessarily correlated with the temperature itself. Finally, in section 7.1.3, possible further investigations and next steps for future work will be highlighted.

7.1.1 THz Polarisers

For the experiment discussed in section 6.2.3, a method for attenuating the THz power in a reliable and controllable way was required, that could be used in combination with the UCA input voltage. One potential method was the use of two wire grid polarisers, set in series in the THz beam path. By keeping one fixed and allowing the other to rotate, the transmitted power could be controllably reduced according to Malus' law [62],

$$I = I_0 \cos^2 \theta, \tag{7.1}$$

where θ is the angle of the second polariser axis with respect to the first polariser axis, I_0 is the initial intensity and I is the final intensity. In order to make use of these polarisers as attenuation devices, they first had to be characterised.

To characterise the THz linear polarisers, source 'B' (see sec.3.3) was brought away from the imaging system, and aligned and focused onto the PM5 power meter. Without the use of a waveguide, the coupling efficiency to the power meter was limited to $\sim 20\%$. In order to scale the measured powers to the actual output, the maximum free space coupling power value was scaled to the equivalent waveguide coupled power value from previous measurements, and all other measurements were scaled by the same amount.

The power response as a single linear polariser was rotated in the THz beam path is shown in figure 7.1a. For every measurement, a background, "THz Off"
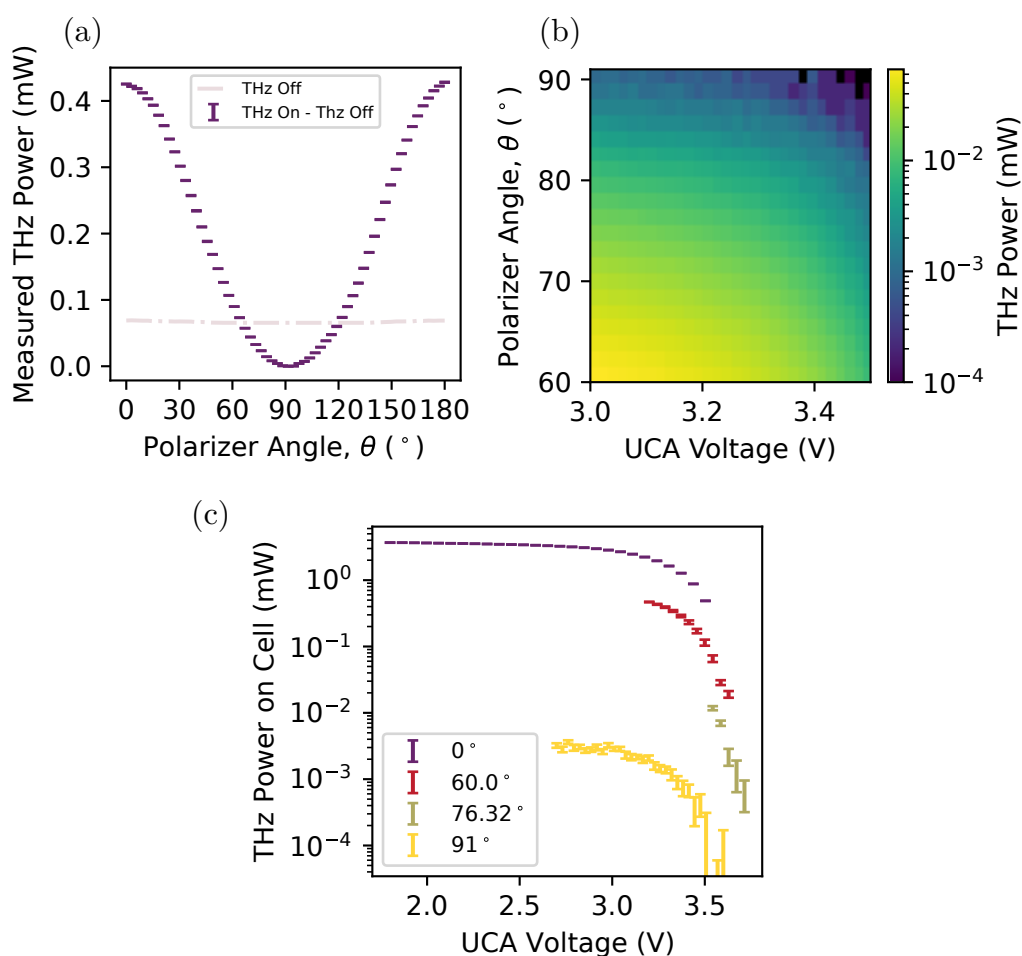
Figure 7.1: (a) THz power measured by PM5 power meter, as a single linear po-lariser was rotated with the UCA voltage fixed to 3.2 V. The datapoints are the average of 8 repeat measurements, while the errorbars represent the stand-ard error on the mean. The grey dashed line shows the average background measurements across those 8 runs. (b) A colourmap showing the measured, background subtracted THz power as a function of polariser angle and UCA voltage on a logarithmic scale. (c) Datapoints chosen to span the largest dy-namic range possible. 4 different polariser angles were chosen and a spread of UCA voltages. The errorbars represent the standard error on the mean with 20 repeat measurements. The powers measured ran from 3.68 mW to 0.14 μW.

measurement was taken, as the thermal nature of the power meter meant it measured a substantial thermal background, so all power measurements are made relative to this background. The polariser followed the expected beha-viour, in that when the polariser transmission axis was aligned with the polar-istion vector of the THz beam ($\theta = 0°$), a maximum power was recorded, and

at 90°, there was a minimum. Figure 7.1b shows a set of measurements, taken with the low power setting of the powermeter, around the minimum (60 to 91°) of the this curve, and across a spread of UCA voltages in which the response was roughly linear. In the region in the upper right (high voltage attenuation, polariser rotated around 90°), the measured value became indistinguishable from the noise. This data was useful for choosing appropriate UCA voltages and polariser angles to repeat that would map out the dynamic range of the source, but would take too long to do many repeat measurements on. The datapoints chosen instead are shown in Figure 7.1c. These values were calibrated across 20 repeat measurements, which were chosen to be the values used in the imaging system.

When the same experiment was replicated in the imaging system, where the detection device used was the atomic vapour sheet, rather than the powermeter, an unexpected result was observed. The beam was focused onto the vapour cell in the same way, and a single linear polariser was rotated in the beam path. Initially, without a polariser in the beam path, a focused spot was observed in the light sheet, as expected. When the polariser was rotated, however, the spatial distribution of the field incident on the cell changed, as can be seen in Figure 7.2. The most dramatic change can be seen around 90°. Initially, the spot does not change much with angle, but gradually stretches along the right diagonal. Around $\approx 80°$ the spot splits into three discrete lobes, until at 90°, the pattern forms four discrete symmetrical lobes. Between 90° and 180°, the pattern reverses, on the opposite diagonal, until it returns to a spot at 180° (not shown).

This changing spatial distribution meant that a minimum detectable power measurement, using a single polariser as an attenuation device was not pos-
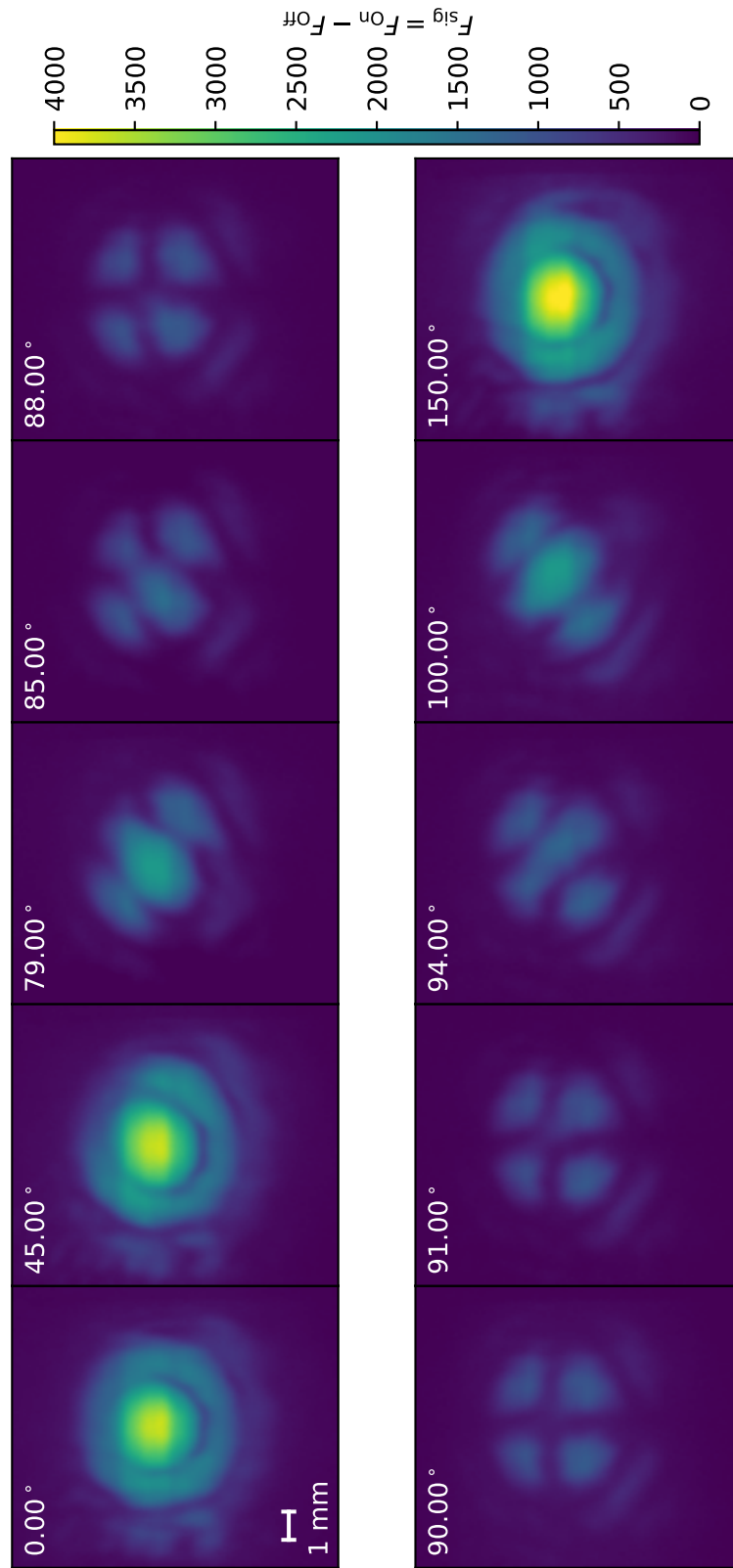
Figure 7.2: Fluorescence signal images of the vapour cell, as a linear polariser is rotated in the THz beam path. The scale marking on the first image is based on the width of the cell being 10 mm. As the polariser is rotated to 90°, the spatial distribution changes significantly.
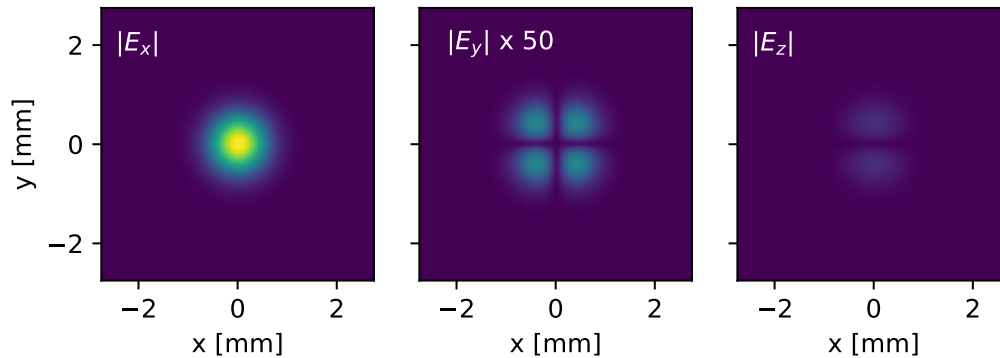
Figure 7.3: Simulated spatial distributions for the absolute values of the three components of an electric field with arbitrary magnitude, tightly focused through a lens. The field is plotted at the position of the focus. The $|E_y|$ component, being too weak to see on the same scale easily, is multiplied by 50. Simulation parameters: wavelength, $\lambda = 0.545$ mm, lens focal length to beam waist ratio, $\frac{f}{w} = 0.3$, initial field amplitude, $E_0 = 1$.

sible, but is an interesting phenomenon in its own right. It was empirically observed that with two polarisers in the beam path, the first polariser the beam encounters would always set this intensity distribution pattern, whilst the second one would alter the overall intensity of the pattern as expected. This occurred regardless of where the polarisers were placed along the beam, and whether they were placed in the diverging, collimated or converging portions of the beam. One hypothesis for why this occurs, is that when light is tightly focused, its vector nature must be taken into account in propagation. Tight focusing of light can generate distinct intensity distributions in the focal region, according to the vector diffraction model described in [114; 115]. In our system, the wavelength is 0.545 mm, and the spot size is $\sim$2 mm, so the assumption that the beam is tightly focused is valid.

In order to test this hypothesis, we attempt to model a tightly focused light field with these parameters. Following the method described, we can use Eqns. 12.34-12.41 in [59] to calculate the electric field distribution in the focal plane, with a Guassin input beam. The results are shown in Figure 7.3.

Here, the x and y components appear similar to the patterns observed in Figure 7.2, at 0° and 90°. We hypothesise, therefore, that in rotating the polariser, this was attenuating the E_x component of the light field, until, at 90°, the only component that remained was the much weaker E_y component. We attempt to model this by calculating the field intensity components, proportional to the electric field amplitude squared. In order to simulate the attenuation due to the rotation of the polariser, we take the intensity to be,

$$I(j) = |jE_x + E_y|^2, \tag{7.2}$$

where j is an attenuation coefficient. The negative sign is chosen to match the experimental data, for polariser angle, $0 \leq \theta \leq 90$. The opposite sign generates results for $90 \leq \theta \leq 180$. The simulated results are shown in Figure 7.4. The intensity distribution patterns match the behaviour of the experimental observations well, which supports the hypothesis that these patterns arise from the vector diffraction of tightly focused light.

To our knowledge, this is the first observation of this effect in a linearly polarised, Guassian THz beam. The implications for this are currently unknown, but the effect in the infra-red regime has found use in applications such as optical trapping [116; 117] and information encoding. Further work could potentially involve investigating this effect in combination with the addition of THz phase plates [118], to prepare THz orbital angular momentum (OAM) beams as inputs. Different polarisation inputs also generate different diffraction patterns, so this could also be investigated. The field pattern at a distance close to the focus could also be modelled, in order to compare with experiment, as the position of the lens is varied.
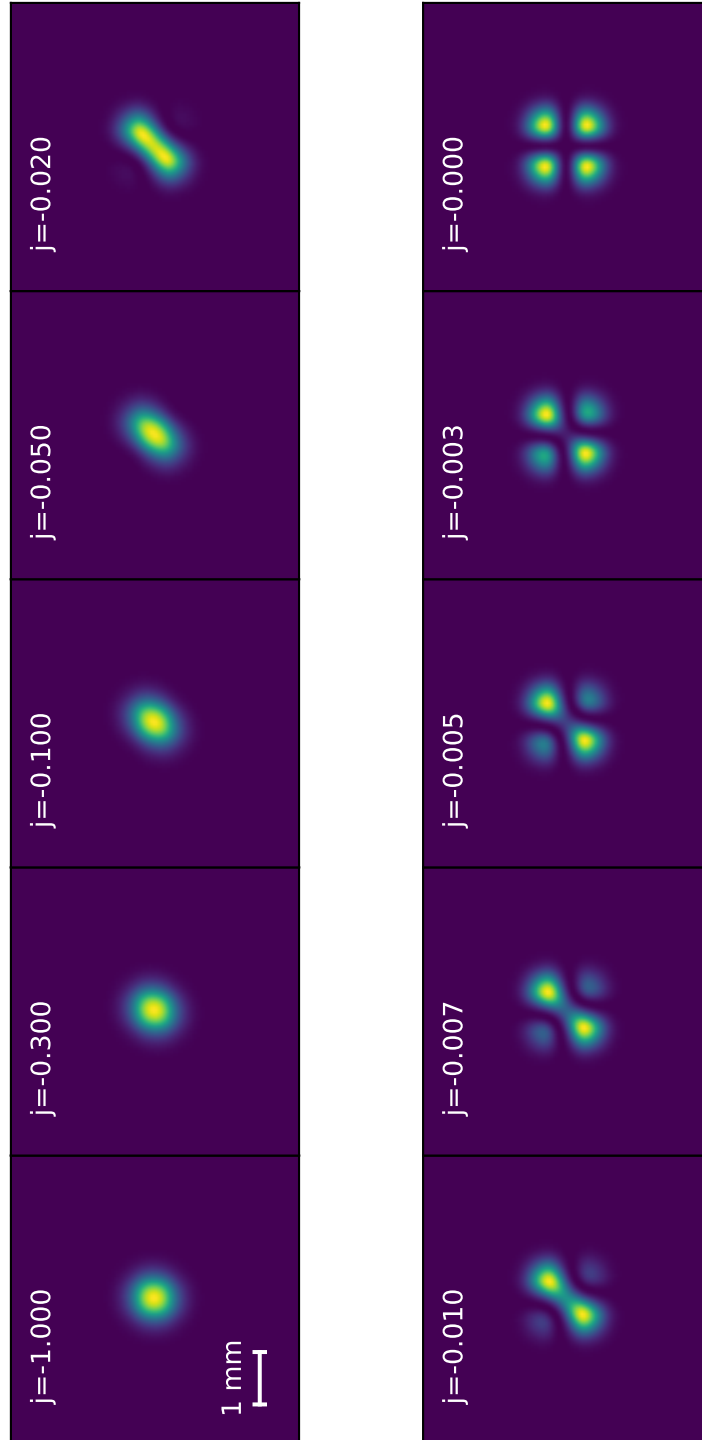
Figure 7.4: Simulated intensity distributions as a function of an attenuation coefficient, j. The variation of j is taken to be equivalent to the rotation of the THz polariser. These simulations are not shown on the same intensity scale, as the scale spans orders of magnitude between $j = 1$ and $j = 0$.

7.1.2 Temperature Investigation

One key experimental parameter that has not been discussed much in this thesis was the effect of the vapour temperature/pressure on the fluorescence signal. This is partly because attempts to characterise the fluorescence response to the temperature discovered unexpected results whose origin was unclear. When investigating this, the Repetier digital PID board (introduced in section 3.5) was developed and implemented as a means to reliably control and maintain the temperature of the cell. This allowed for the temperature to be monitored and changed in real time, at the same time as fluorescence values, lock signals etc. Therefore, an idea to easily map out the temperature dependence of the fluorescence, was to activate the cell heaters from a cold start, and monitor the fluorescence up to the set temperature, in order to plot the fluorescence as a function of temperature. We would expect that the increase in temperature and concomitant increase in number density to increase the fluorescence signal, up to the point when the vapour would become optically thick to the probe beam. Instead, it was found that the fluorescence peaked whilst the temperature was increasing, before returning to a lower level in the long term.

Figure 7.5 shows an illustrative example of this phenomenon, when the temperature was set to 70°. In this data, taken from experiment 'A', the THz source was not active, and so this fluorescence is purely in the "THz Off" configuration of the experiment. The PID loop was initially set to a setpoint of 70°C, and after approximately half an hour the heater was turned off and the cell allowed to naturally cool. The top pane shows the fluorescence value, averaged over three different regions of interest in the beam. The purple trace is the normal region of interest over the entire beam, where the red and gold are over regions
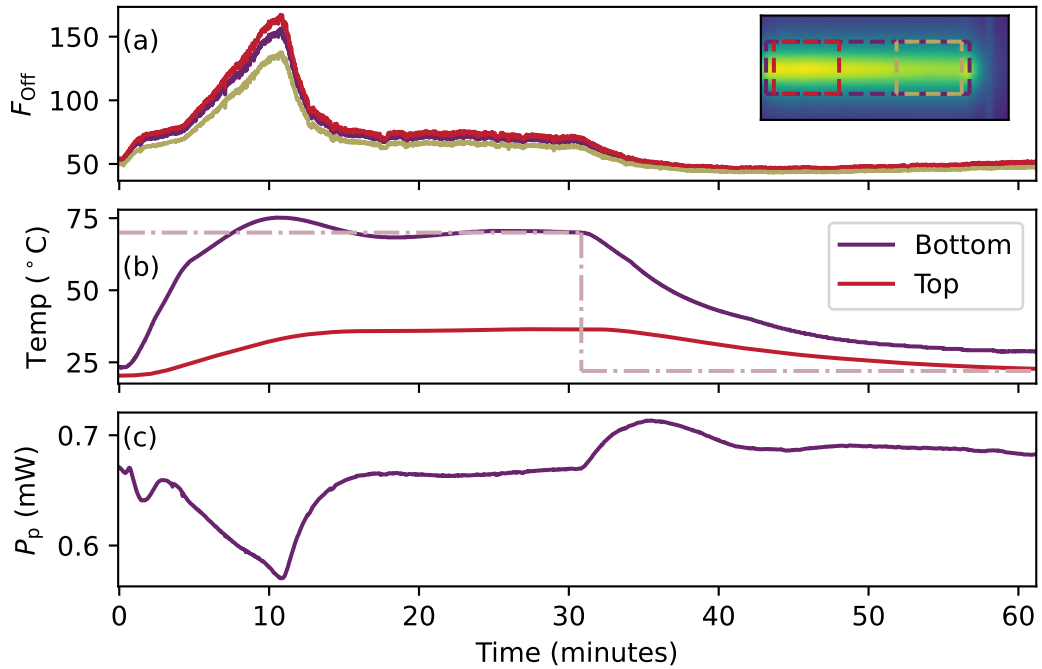
Figure 7.5: (Top Pane) The F_{Off} fluorescence, measured over time, as the temperature was changed. The purple trace shows the average over the entire region of interest (the whole beam), where the red and gold show averages over the left and right hand side of the cell respectively. The probe beam enters via the left hand side of the cell, as shown in the inset. (Middle Pane) The temperature, measured by thermocouples, at the bottom (purple) and top (red) of the cell. The dashed line indicated the setpoint of the temperature PID. (Bottom Pane) The probe power detected on a powermeter after transmission through the cell

on the left and right hand side of the beam respectively, where the left hand side of the cell is the direction from which the probe beam enters. The inset here shows the 3 different regions of interest marked on an example image. The second pane shows the temperature of the cell, where the purple trace is recorded from the thermocouple connected to the Repetier, at the base of the cell holder, and the red is from a thermocouple placed at the very top of the cell. The distance between these thermocouples was approximately the height of the cell, ≈ 60 mm. The dashed line indicates the setpoint of the heater - approximately halfway through, the heaters were turned off indicated by the

dashed line going to zero. The third pane shows the transmitted probe power as meaured using an optical powermeter after transmission through the cell on a pickoff after the cell.

As can been seen in the top pane, as the temperature increases, there is a large spike in fluorescence, where the value is more than 3 times larger than the initial value. This spike in fluorescence then quickly reduces again. It was found that in repeat measurements, whereby the cell is allowed to cool, and then heated up again, this spike repeatedly occurs. However, the size and temperature at which the peak occurs varies, and does not seem to be directly correlated with either the set temperature, or the gradient of the temperature change. There is also an increase and subsequent decrease in the absorption of the probe beam, associated with the change in fluorescence. When the heater is turned off and the cell begins to cool, there is a decrease in probe absorption, that then settles back to a 'stationary' level.

This experiment was repeated for a variety of different set temperatures, between 30° C and 80° C, and the effect persisted for all of them, but a particular pattern to this behaviour could not be deciphered. The effect of the set temperature was observed in the 'steady state' tail, where the settled fluorescence value then depended on the vapour temperature. One hypothesis for the origin of this effect is that, as the cell was heated, the number density increased with a concomitant increase in fluorescence. Then, due to temperature gradient in the cell, atoms were likely to adsorb or condense onto the sides of the cell, which would simultaneously decrease probe transmission, and reduce the amount of fluorescence. This does not seem an entirely satisfactory explanation though, as there was no caesium condensate visible on the sides of the cell. Nevertheless, as can be seen by measuring simultaneously at the top and the base of

the cell holder, there is a large difference in temperature at these points, which suggests that more care must be taken with how the temperature is necessarily measured.

7.1.3 Further Investigations

The immediate next few steps in order to conclude the investigation of this thesis could involve a number of different avenues. These could include measurements that demonstrate the improved capabilities of the imaging system after the optimization of experimental parameters, the locking of the Rydberg lasers, and the introduction of a signal-boosting repump laser. For example, a renewed fluorecence signal against power measurement after calibrating a double linear polariser setup as an attenuation method could be performed. The double polariser setup should lead to smaller errorbars on the THz power estimations, and the signal increase due to, e.g the repump laser, should lead to a larger signal to noise, and an improved sensitivity measurement. The increased signal provided by the repump could also enable imaging of dynamics on an even faster timescale than currently possible, with the implementation of high speed video cameras. Further fundamental investigations could be done, for example, into the role that collisions play into the system - decay from the $|13D_{3/2}\rangle$ level, a dipole forbidden transition from the $|13D_{5/2}\rangle$ level, makes up a significant part of our signal. This level is almost certainly reached via J-mixing collisions [71], which with a better understanding of the mechanisms at play, could be used to our advantage to increase our signal. Knowledge of these collisional mechanisms in a thermal Rydberg vapour would also help when implementing similar level schemes in other atomic species, or when addressing different Rydberg levels for different imaging schemes.
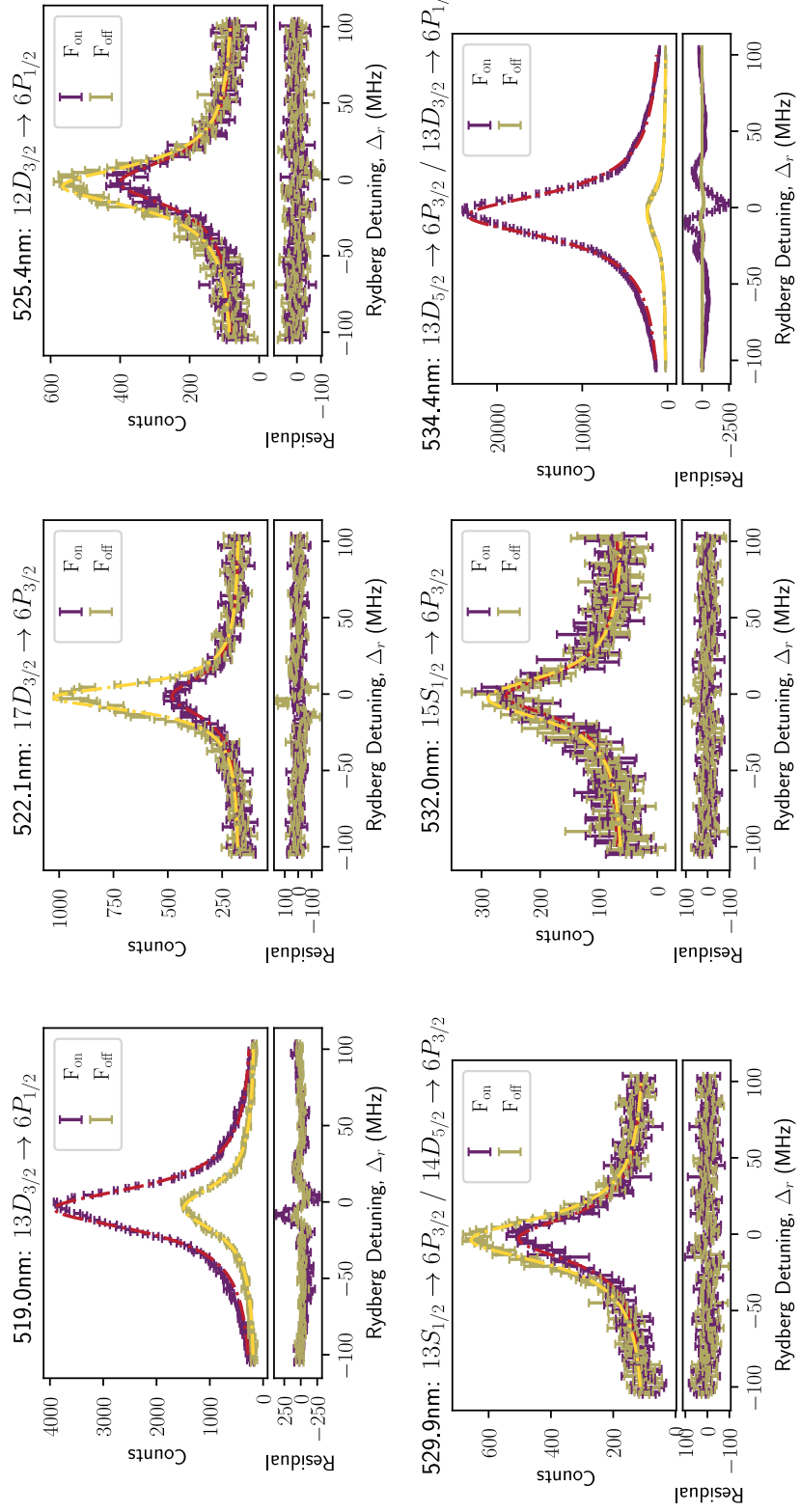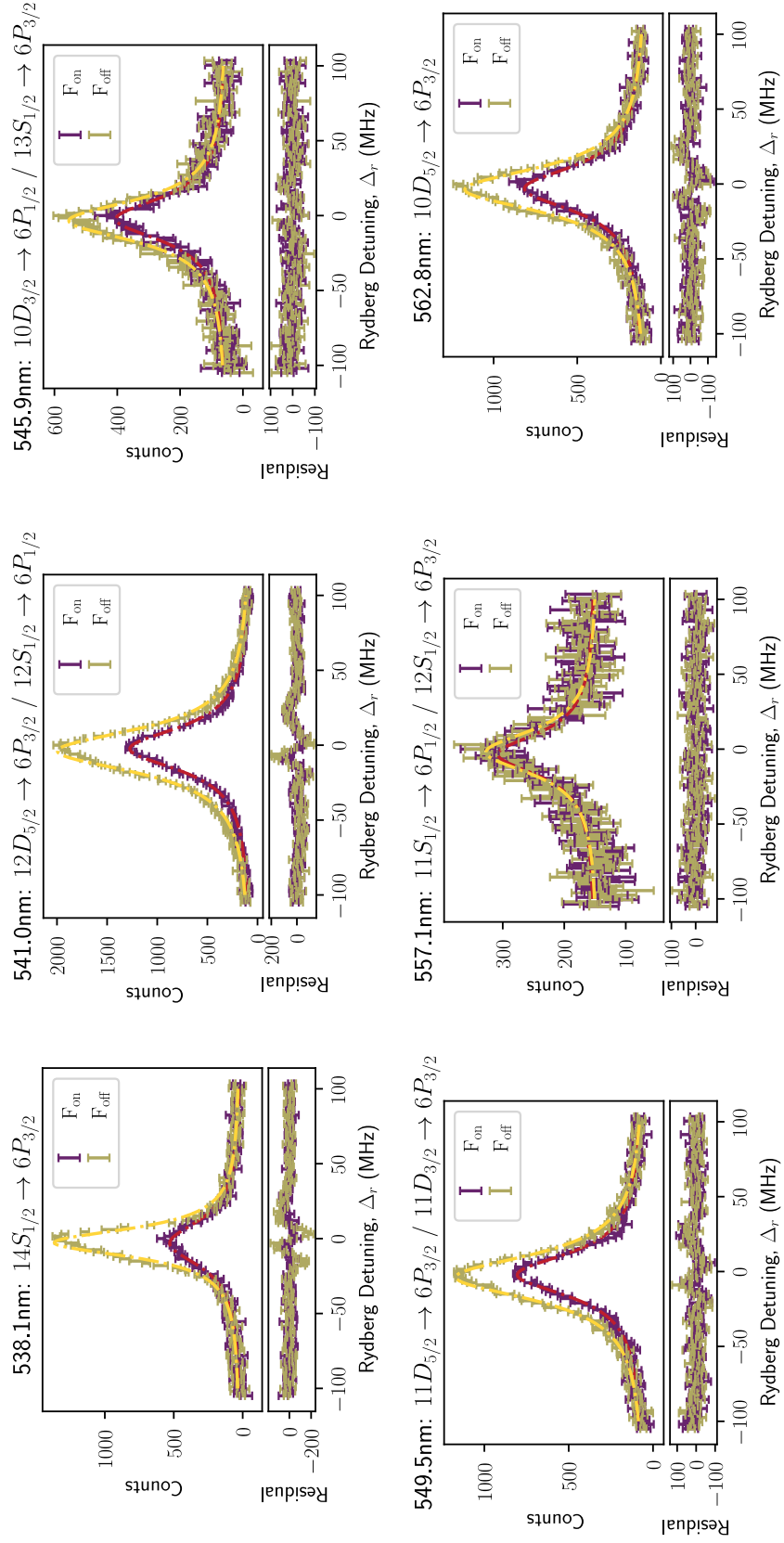
7.2 Concluding Remarks

In this thesis, developments were made towards the characterisation and optimization of a Rydberg atom based terahertz imaging system. In Chapter 4, we successfully implemented two different methods for locking the Rydberg laser, which enabled fluorescence signal stability to within 3%. The scanning transfer cavity lock allowed for digital control of the Rydberg frequency, which can be viewed as a step towards improving the in-the-field capabilites of this system as a THz imager. In Chapter 5, we characterised the dependence of the fluorescence signal on laser power, laser polarisation and the Rydberg laser and THz detuning. Of these common experimental parameters, optimisation of the polarisation configurations was found to give the biggest increase in signal, of around 38%, by implementing a pumping scheme of alternating circular polarisations. Maintaining a moderate probe and coupling laser power, whilst maximising the Rydberg power was also found to maximise the fluorescence signal. Meanwhile, it was confirmed that maintaining resonance with the Rydberg and THz transitions provided the biggest signal, despite the possibility of a more optimal two photon transtion. In Chapter 6, we found that implementing a repump laser on either of the $|6S_{1/2}, F = 3\rangle \rightarrow \dots$ transitions led to a massive increase in signal, which was measured up to 6.8 times the original signal. The repump laser was characterised in terms of its detuning with respect to both transitions, and its power relative to the probe. The D1 line was found to increase the signal the most, and a peak of unknown origin appears in the D2 line spectrum, detuned $\approx$250 MHz from the $F = 3 \rightarrow F' = 4$ transition. In Chapter 7, we introduced some topics that warrant further investigation, including an observation of a vector diffraction pattern: the THz beam, despite having a macroscopic wavelength could be described as tightly focused,
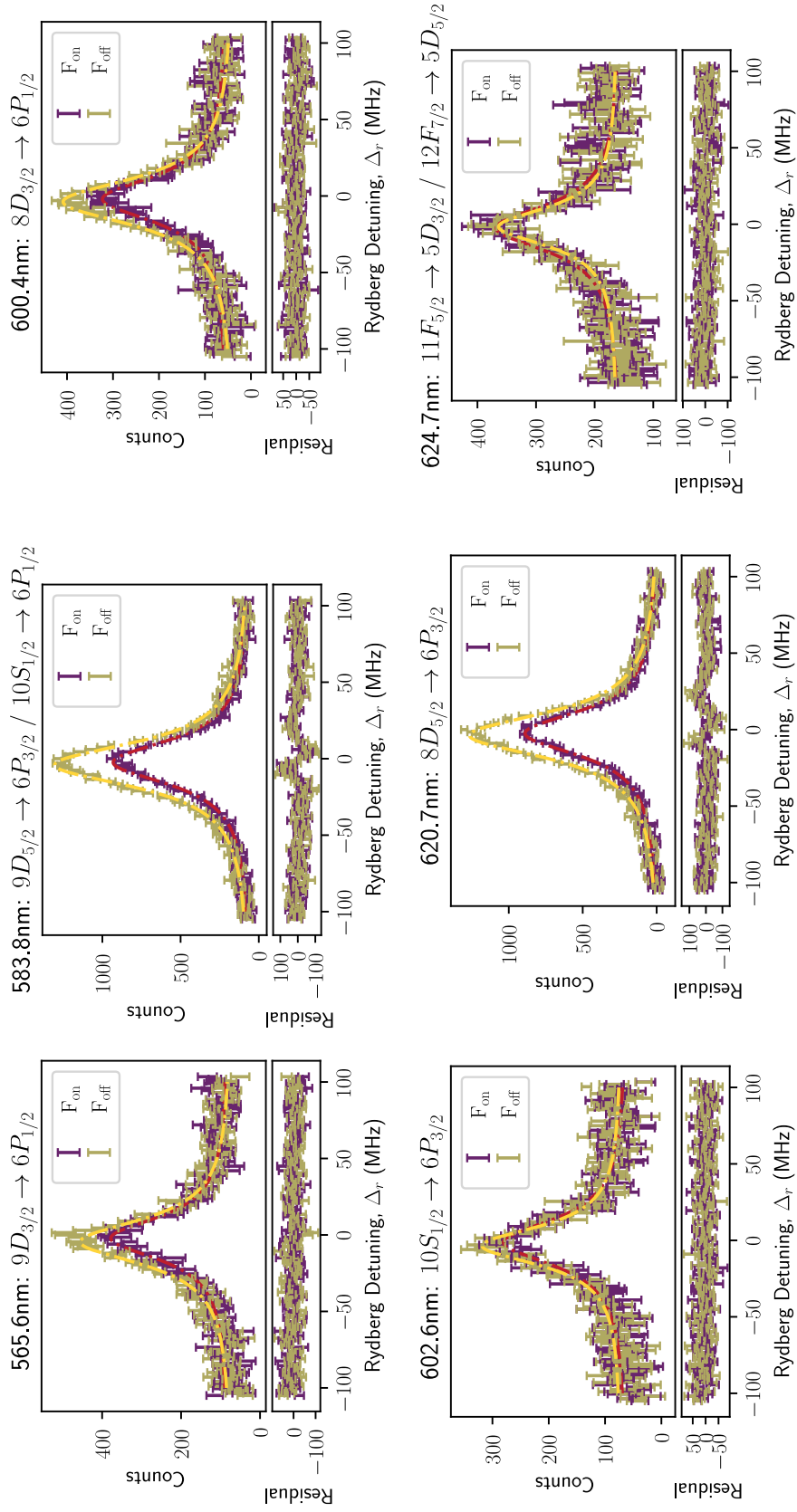
leading to vector nature of the light to create a diffraction pattern. An inconclusive investigation into the effect of the cell temperature / vapour pressure on the fluorescence signal also found an initial huge increase in fluorescence, that quickly returned to a steady state value, dependent on the temperature. Overall, the optimisations introduced in this thesis could lead to promising new utility in the imaging system, allowing for increased frame rates and sensitivity, and the efforts towards characterisation should help in the progress towards commercialisation and application of the system in the field.
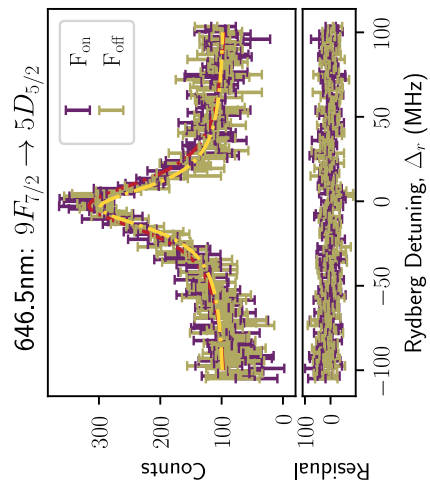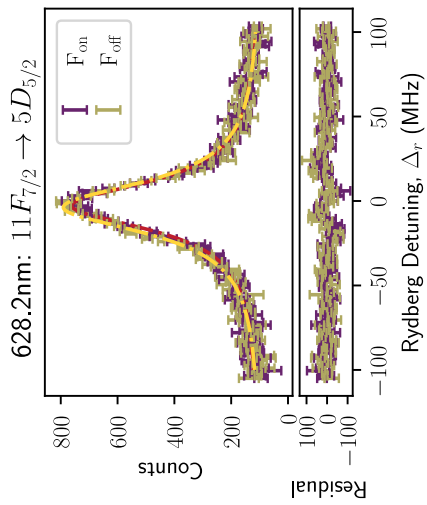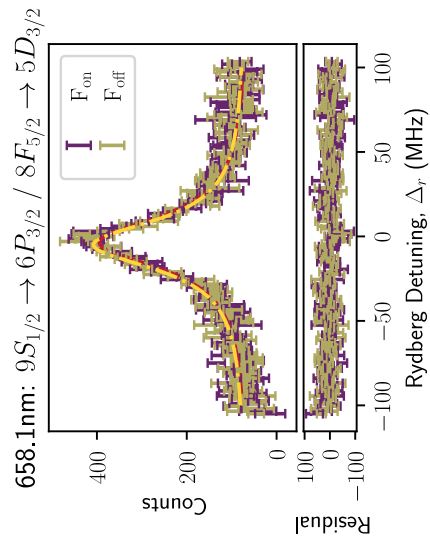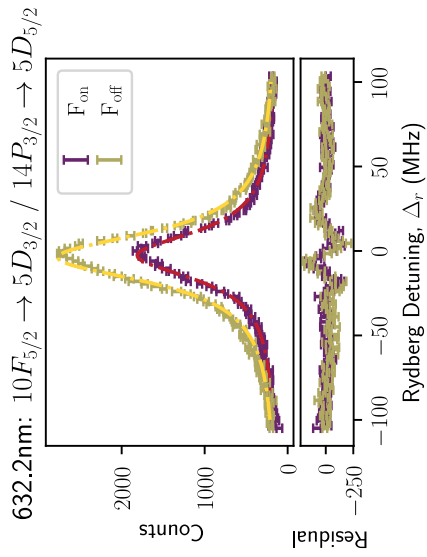
Decay Lines

In this section, graphs will be presented for reference, of the fluorescence counts against Rydberg detuning, for every identified decay line from a spectrometer trace taken as the Rydberg laser was scanned. These were obtained following the method described in section 5.3. The specific decay channels were identified with use of a Monte-Carlo model to predict the various allowed decay paths that are allowed. This included some imposed collisional transfer from the $13D_{5/2}$ to the $13D_{3/2}$ state, which is implemented by initially placing some population into this state. Otherwise, the only allowed decay pathways are dipole allowed. For cases where more than one transition is labelled, then each transition was not resolvable within the resolution of the spectrometer. Each lineshape is fitted with a Lorentzian, for the cases for both F_{on} and F_{off}. The average FWHM for both was about 17 MHz. From top left to bottom right, they are plotted in ascending wavelength order.

545.9nm: $10D_{3/2} \rightarrow 6P_{1/2}$ / $13S_{1/2} \rightarrow 6P_{3/2}$

541.0nm: $12D_{5/2} \rightarrow 6P_{3/2}$ / $12S_{1/2} \rightarrow 6P_{1/2}$

538.1nm: $14S_{1/2} \rightarrow 6P_{3/2}$

562.8nm: $10D_{5/2} \rightarrow 6P_{3/2}$

557.1nm: $11S_{1/2} \rightarrow 6P_{1/2}$ / $12S_{1/2} \rightarrow 6P_{3/2}$

549.5nm: $11D_{5/2} \rightarrow 6P_{3/2}$ / $11D_{3/2} \rightarrow 6P_{3/2}$

635.9nm: $10F_{7/2} \rightarrow 5D_{5/2}$ / $9S_{1/2} \rightarrow 6P_{1/2}$

632.2nm: $10F_{5/2} \rightarrow 5D_{3/2}$ / $14P_{3/2} \rightarrow 5D_{5/2}$

628.2nm: $11F_{7/2} \rightarrow 5D_{5/2}$

671.3nm: $11P_{1/2} \rightarrow 5D_{3/2}$

658.1nm: $9S_{1/2} \rightarrow 6P_{3/2}$ / $8F_{5/2} \rightarrow 5D_{3/2}$

646.5nm: $9F_{7/2} \rightarrow 5D_{5/2}$
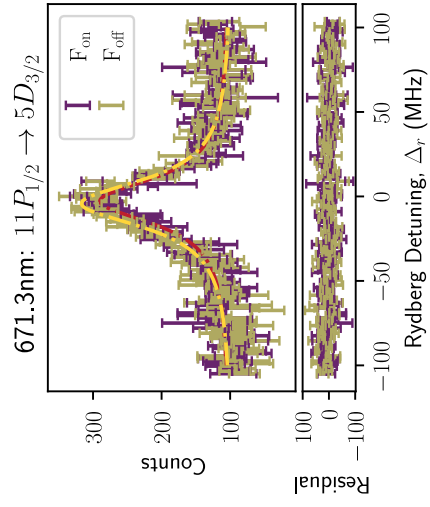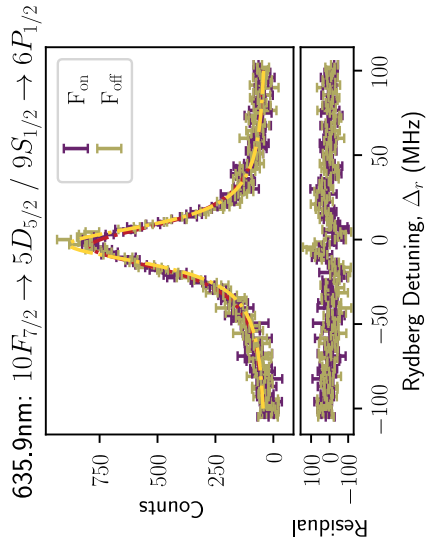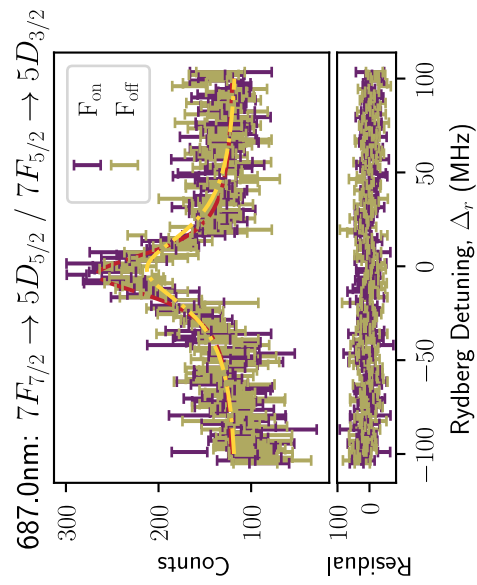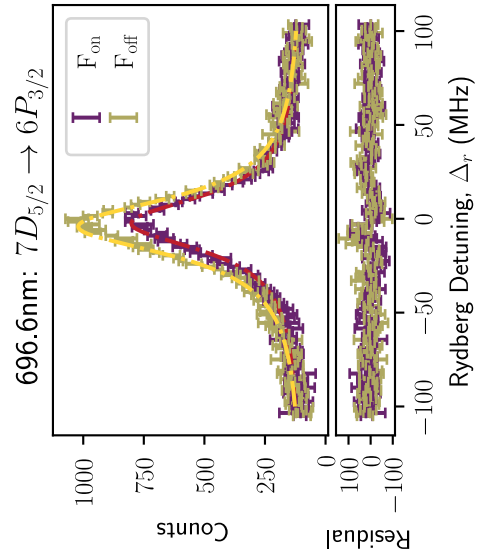
Bibliography

[1]   D. P. DiVincenzo, "Scientists and citizens: getting to quantum technolo-
        gies," Ethics and Information Technology **19**, 247 (2017).

[2]   T. M. Roberson, "On the social shaping of quantum technologies: An
        analysis of emerging expectations through grant proposals from 2002–
        2020," Minerva **59**, 379 (2021).

[3]   S. Knappe, V. Shah, P. D. D. Schwindt, L. Hollberg, J. Kitching, L.-A. Liew,
        and J. Moreland, "A microfabricated atomic clock," Applied Physics Let-
        ters **85**, 1460 (2004).

[4]   A. D. Ludlow, M. M. Boyd, J. Ye, E. Peik, and P. O. Schmidt, "Optical
        atomic clocks," Rev. Mod. Phys. **87**, 637 (2015).

[5]   J. Kitching, S. Knappe, and E. A. Donley, "Atomic sensors – a review,"
        IEEE Sensors Journal **11**, 1749 (2011).

[6]   T. W. Kornack, R. K. Ghosh, and M. V. Romalis, "Nuclear spin gyroscope
        based on an atomic comagnetometer," Phys. Rev. Lett. **95**, 230801 (2005).

[7]   J. Fang and J. Qin, "Advances in atomic gyroscopes: A view from inertial navigation applications," Sensors **12**, 6331 (2012).

[8]   D. Budker and M. Romalis, "Optical magnetometry," Nature Physics **3**, 227 (2007).

[9]   P. D. D. Schwindt, S. Knappe, V. Shah, L. Hollberg, J. Kitching, L.-A. Liew, and J. Moreland, "Chip-scale atomic magnetometer," Applied Physics Letters **85**, 6409 (2004).

[10]   C. Janvier, V. Ménoret, B. Desruelle, S. Merlet, A. Landragin, and F. Pereira dos Santos, "Compact differential gravimeter at the quantum projection-noise limit," Phys. Rev. A **105**, 022801 (2022).

[11]   F. A. Narducci, A. T. Black, and J. H. Burke, "Advances towards fieldable atom interferometers," Advances in Physics:X **7** (2022), 10.1080/23746149.2021.1946426.

[12]   A. R. Perry, M. D. Bulatowicz, M. Larsen, T. G. Walker, and R. Wyllie, "All-optical intrinsic atomic gradiometer with sub-20 ft/cm/√hz sensitivity in a 22 µt earth-scale magnetic field," Opt. Express **28**, 36696 (2020).

[13]   K. McDonnell, L. F. Keary, and J. D. Pritchard, "Demonstration of a quantum gate using electromagnetically induced transparency," Phys. Rev. Lett. **129**, 200501 (2022).

[14]   M. Saffman, "Quantum computing with neutral atoms," National Science Review **6**, 24 (2018), https://academic.oup.com/nsr/article-pdf/6/1/24/38915067/nwy088.pdf .

[15] L. A. Downes, A. R. MacKellar, D. J. Whiting, C. Bourgenot, C. S. Adams, and K. J. Weatherill, "Full-field terahertz imaging at kilohertz frame rates using atomic vapor," Phys. Rev. X **10**, 011027 (2020).

[16] C. G. Wade, N. Šibalić, N. R. de Melo, J. M. Kondo, C. S. Adams, and K. J. Weatherill, "Real-time near-field terahertz imaging with atomic optical fluorescence," Nature Photonics **11**, 40 (2017).

[17] B. E. Jones, J. W. Thomas, A. Selyem, S. Jones, D. Bremner, L. A. Downes, P. A. Marsden, P. Brown, and K. J. Weatherill, "A compact stabilized three-laser optical pump system for an imaging system based on THz-to-visible conversion via atomic vapour," in *Quantum Sensing and Nano Electronics and Photonics XVIII*, Vol. PC12009, edited by M. Razeghi, G. A. Khodaparast, and M. S. Vitiello, International Society for Optics and Photonics (SPIE, 2022) p. PC120090J.

[18] Y. Zhang, K. Li, and H. Zhao, "Intense terahertz radiation: generation and application," Front Optoelectron **14**, 4 (2020).

[19] R. A. Lewis, "A review of terahertz sources," Journal of Physics D: Applied Physics **47**, 374001 (2014).

[20] Y. Lee, "Terahertz spectroscopy of condensed matter," in *Principles of Terahertz Science and Technology* (Springer US, 2009).

[21] J. Kroll, J. Darmo, and K. Unterrainer, "Terahertz spectroscopy of vibrational modes of molecular crystal of sucrose," in *Infrared and Millimeter Waves, 2004* (2004).

[22] C. Kulesa, "Terahertz spectroscopy for astronomy: From comets to cosmology," IEEE Transactions on Terahertz Science and Technology **1**, 232 (2011).

[23] K. S, Y. M, A. Rawson, and S. C. K, "Recent advances in terahertz time-domain spectroscopy and imaging techniques for automation in agriculture and food sector," Food Analytical Methods **15**, 498 (2022).

[24] E. Pickwell and V. P. Wallace, "Biomedical applications of terahertz technology," Journal of Physics D: Applied Physics **39** (2006).

[25] K. I. Zaytsev, I. N. Dolganova, N. V. Chernomyrdin, G. M. Katyba, A. A. Gavdush, O. P. Cherkasova, G. A. Komandin, M. A. Shchedrina, A. N. Khodan, D. S. Ponomarev, I. V. Reshetov, V. E. Karasik, M. Skorobogatiy, V. N. Kurlov, and V. V. Tuchin, "The progress and perspectives of terahertz technology for diagnosis of neoplasms: a review," Journal of Optics **22**, 013001 (2019).

[26] Y. Peng, C. Shi, Y. Zhu, M. Gu, and S. Zhuang, "Terahertz spectroscopy in biomedical field: a review on signal-to-noise ratio improvement," PhotoniX **1**, 12 (2020).

[27] M. H. Rahaman, A. Bandyopadhyay, S. Pal, and K. P. Ray, "Reviewing the scope of thz communication and a technology roadmap for implementation," IETE Technical Review **38**, 465 (2021).

[28] Y. Ghasempour, R. Shrestha, A. Charous, E. Knightly, and D. M. Mittleman, "Single-shot link discovery for terahertz wireless networks," Nature Communications **11** (2020).

[29] J. F. Federici, B. Schulkin, F. Huang, D. Gary, R. Barat, F. Oliveira, and D. Zimdars, "THz imaging and sensing for security applications—explosives, weapons and drugs," Semiconductor Science and Technology **20** (2005).

[30] T. Amini, F. Jahangiri, Z. Ameri, and M. A. Hemmatian, "A review of feasible applications of THz waves in medical diagnostics and treatments," J Lasers Med Sci **12**, e92 (2021).

[31] S. Zhong, "Progress in terahertz nondestructive testing: A review," Frontiers of Mechanical Engineering **14**, 273 (2019).

[32] J. L. Boland, K. Peng, S. Baig, D. Damry, P. Parkinson, L. Fu, H. Hoe Tan, C. Jagadish, L. M. Herz, H. Joyce, and M. Johnston, "The route to nanoscale terahertz technology: Nanowire-based terahertz detectors and terahertz modulators," in *2018 43rd International Conference on Infrared, Millimeter, and Terahertz Waves (IRMMW-THz)* (2018).

[33] K. Peng, P. Parkinson, Q. Gao, J. L. Boland, Z. Li, F. Wang, Y. C. Wenas, C. L. Davies, L. Fu, M. B. Johnston, H. H. Tan, and C. Jagadish, "Single nanowire photoconductive terahertz detectors," Nano Letters **15** (2015).

[34] Y. He, Y. Wang, D. Xu, J. Li, C. Yan, L. Tang, X. Zhu, H. Liu, B. Teng, and J. Yao, "High-energy and ultra-wideband tunable monochromatic terahertz source and frequency domain system based on DAST crystal," in *Terahertz, RF, Millimeter, and Submillimeter-Wave Technology and Applications XII*, Vol. 10917 (2019).

[35] N. G. Bello, S. Smirnov, A. Gorodetsky, and E. U. Rafailov, "Towards realisation of an efficient continuous wave terahertz source using quantum dot devices," in *Terahertz Emitters, Receivers, and Applications X*, Vol. 11124 (2019).

[36] P. S. Nugraha, G. Krizsán, C. Lombosi, L. Pálfalvi, G. Tóth, G. Almási, J. A. Fülöp, and J. Hebling, "Demonstration of a tilted-pulse-front pumped plane-parallel slab terahertz source," Opt. Lett. **44** (2019).

[37] B. Scherger, M. Scheller, C. Jansen, M. Koch, and K. Wiesauer, "Terahertz lenses made by compression molding of micropowders," Appl. Opt. **50** (2011).

[38] E. Bründermann, H. Hübers, M. Fitz, and G. Kimmitt, *Terahertz Techniques* (Springer, 2012).

[39] Y. Wang, Z. Sun, D. Xu, L. Wu, J. Chang, L. Tang, Z. Jiang, B. Jiang, G. Wang, T. Chen, H. Feng, and J. Yao, "A hybrid method based region of interest segmentation for continuous wave terahertz imaging," Journal of Physics D: Applied Physics **53** (2019).

[40] T. F. Gallagher, *Rydberg Atoms*, Cambridge Monographs on Atomic, Molecular and Chemical Physics (Cambridge University Press, 1994).

[41] C. S. Adams, J. D. Pritchard, and J. P. Shaffer, "Rydberg atom quantum technologies," Journal of Physics B: Atomic, Molecular and Optical Physics **53**, 012002 (2019).

[42] G. Pelegrí, A. J. Daley, and J. D. Pritchard, "High-fidelity multiqubit rydberg gates via two-photon adiabatic rapid passage," Quantum Science and Technology **7**, 045020 (2022).

[43] C. L. Holloway, J. A. Gordon, S. Jefferts, A. Schwarzkopf, D. A. Anderson, S. A. Miller, N. Thaicharoen, and G. Raithel, "Broadband rydberg atom-based electric-field probe for si-traceable, self-calibrated measurements," IEEE Transactions on Antennas and Propagation **62**, 6169 (2014).

[44] J. A. Sedlacek, A. Schwettmann, H. Kübler, R. Löw, T. Pfau, and J. P. Shaffer, "Microwave electrometry with rydberg atoms in a vapour cell using bright atomic resonances," Nature Physics **8**, 819 (2012).

[45]   D. A. Anderson, R. E. Sapiro, and G. Raithel, "A self-calibrated si-traceable rydberg atom-based radio frequency electric field probe and measurement instrument," IEEE Transactions on Antennas and Propagation **69**, 5931 (2021).

[46]   C. L. Holloway, J. A. Gordon, A. Schwarzkopf, D. A. Anderson, S. A. Miller, N. Thaicharoen, and G. Raithel, "Sub-wavelength imaging and field mapping via electromagnetically induced transparency and Autler-Townes splitting in Rydberg atoms," Applied Physics Letters **104** (2014), 10.1063/1.4883635.

[47]   M. Drabbels and L. D. Noordam, "Infrared imaging camera based on a Rydberg atom photodetector," Applied Physics Letters **74**, 1797 (1999).

[48]   N. Šibalić, J. Pritchard, C. Adams, and K. Weatherill, "Arc: An open-source library for calculating properties of alkali rydberg atoms," Computer Physics Communications **220**, 319 (2017).

[49]   A. R. Edmonds, *Angular Momentum in Quantum Mechanics* (Princeton University Press, Princeton, 1957).

[50]   M. E. Rose, *Elementary Theory of Angular Momentum* (Wiley, 1957).

[51]   B. C. Hall, *Lie Groups, Lie Algebras, and Representations: An Elementary Introduction*, Graduate Texts in Mathematics, Vol. 222 (Springer, New York, 2010) p. 351 S.

[52]   B. C. Hall, *Quantum Theory for Mathematicians*, Graduate Texts in Mathematics No. 267 (Springer New York).

[53]   J. J. Sakurai, *Modern Quantum Mechanics: 2nd Edition* (Addison-Wesley, Reading, MA, 1994).

[54]   A. Messiah, *Quantum Mechanics Volume II* (Elsevier Science B.V., 1961).

[55]   R. D. Cowan, *The Theory of Atomic Structure and Spectra,* Los Alamos Series in Basic and Applied (University of California Press, Ltd., Berkeley, 1981).

[56]   C. Foot, *Atomic Physics* (Oxford University Press, USA, 2005).

[57]   M. Allegrini, E. Arimondo, and L. A. Orozco, "Survey of Hyperfine Structure Measurements in Alkali Atoms," Journal of Physical and Chemical Reference Data **51** (2022), 10.1063/5.0098061.

[58]   E. Hecht, *Optics,* 4th ed. (Addison-Wesley, 1998).

[59]   C. S. Adams and I. G. Hughes, *Optics f2f: From Fourier to Fresnel* (Oxford University Press, 2019).

[60]   W. Nagourney, *Quantum Electronics for Atomic Physics and Telecommunication* (Oxford University Press, 2014).

[61]   G. G. Stokes, "On the composition and resolution of streams of polarized light from different sources," Proceedings of the Cambridge Philosophical Society : Mathematical and physical sciences (1852).

[62]   E. Collett, *Field Guide to Polarization,* Field Guides (SPIE Press, 2005).

[63]   G. Baym, *Lectures on Quantum Mechanics* (Avalon Publishing, 1990).

[64]   H. J. Metcalf and P. van der Straten, *Laser Cooling and Trapping* (Springer-Verlag, New York, 1999).

[65]   R. W. Fox, C. W. Oates, and L. W. Hollberg, "1. stabilizing diode lasers to high-finesse cavities," in *Cavity-Enhanced Spectroscopies,* Experimental

Methods in the Physical Sciences, Vol. 40, edited by R. D. van Zee and J. P. Looney (Academic Press, 2003) pp. 1–46.

[66] O. Axner, J. Gustafsson, N. Omenetto, and J. D. Winefordner, "Line strengths, a-factors and absorption cross-sections for fine structure lines in multiplets and hyperfine structure components in lines in atomic spectrometry—a user's guide," Spectrochimica Acta Part B: Atomic Spectroscopy **59**, 1 (2004).

[67] C. Cohen-Tannoudji, G. Grynberg, and J. Dupont-Roc, *Atom-Photon Interactions: Basic Processes and Applications* (Wiley, New York, 1992).

[68] N. B. Delone and V. P. Krainov, "Ac stark shift of atomic energy levels," Physics-Uspekhi **42**, 669 (1999).

[69] P. Siddons, C. S. Adams, C. Ge, and I. G. Hughes, "Absolute absorption on rubidium d lines: comparison between theory and experiment," Journal of Physics B: Atomic, Molecular and Optical Physics **41**, 155004 (2008).

[70] R. Loudon, *The Quantum Theory of Light*, 2nd ed. (Clarendon Press, Oxford, 1983).

[71] L. A. Downes, *A High-speed THz Imaging System based on THz-to-optical Conversion in Atomic Vapour*, Ph.D. thesis, Durham University (2020).

[72] K. Blum, *Density matrix theory and applications; 3rd ed.*, Springer series on atomic, optical, and plasma physics (Springer, Berlin, 2012).

[73] J. Gea-Banacloche, Y.-q. Li, S.-z. Jin, and M. Xiao, "Electromagnetically induced transparency in ladder-type inhomogeneously broadened media: Theory and experiment," Phys. Rev. A **51**, 576 (1995).

[74]   A. Kramida, Yu. Ralchenko, J. Reader,   and and NIST ASD Team, NIST Atomic Spectra Database (ver. 5.7.1), [Online]. Available: https://physics.nist.gov/asd [2020, May 28]. National Institute of Standards and Technology, Gaithersburg, MD. (2019).

[75]   J. D. Pritchard, D. Maxwell, A. Gauguet, K. J. Weatherill, M. P. A. Jones, and C. S. Adams, "Cooperative atom-light interaction in a blockaded rydberg ensemble," Phys. Rev. Lett. **105**, 193603 (2010).

[76]   L. A. Downes, L. Torralbo-Campo, and K. J. Weatherill, "A practical guide to terahertz imaging using thermal atomic vapour," New Journal of Physics **25**, 035002 (2023).

[77]   C. P. Pearman, C. S. Adams, S. G. Cox, P. F. Griffin, D. A. Smith, and I. G. Hughes, "Polarization spectroscopy of a closed atomic transition: applications to laser frequency locking," Journal of Physics B: Atomic, Molecular and Optical Physics **35**, 5141 (2002).

[78]   M. L. Harris, C. S. Adams, S. L. Cornish, I. C. McLeod, E. Tarleton, and I. G. Hughes, "Polarization spectroscopy in rubidium and cesium," Phys. Rev. A **73**, 062509 (2006).

[79]   C. Carr, C. S. Adams, and K. J. Weatherill, "Polarization spectroscopy of an excited state transition," Optics Letters **37**, 118 (2012).

[80]   S. Subhankar, A. Restelli, Y. Wang, S. L. Rolston, and J. V. Porto, "Microcontroller based scanning transfer cavity lock for long-term laser frequency stabilization," Review of Scientific Instruments **90**, 043115 (2019).

[81] R. W. P. Drever, J. L. Hall, F. V. Kowalski, J. Hough, G. M. Ford, A. J. Munley, and H. Ward, "Laser phase and frequency stabilization using an optical resonator," Applied Physics **31** (1983).

[82] J. I. Thorpe, K. Numata, and J. Livas, "Laser frequency stabilization and control through offset sideband locking to optical cavities," Optics Express **16** (2008).

[83] *Feedhorn Summary*, Virginia Diodes Inc. (2020).

[84] C. R. Harris, K. J. Millman, S. J. van der Walt, R. Gommers, P. Virtanen, D. Cournapeau, E. Wieser, J. Taylor, S. Berg, N. J. Smith, R. Kern, M. Picus, S. Hoyer, M. H. van Kerkwijk, M. Brett, A. Haldane, J. Fernández del Río, M. Wiebe, P. Peterson, P. Gérard-Marchant, K. Sheppard, T. Reddy, W. Weckesser, H. Abbasi, C. Gohlke, and T. E. Oliphant, "Array programming with NumPy," Nature **585**, 357–362 (2020).

[85] R. . Schwarz, "`rsinstrument`," .

[86] N. Instruments, "`ni-daqmx`," .

[87] H. E. Grecco, M. C. Dartiailh, G. Thalhammer-Thurner, T. Bronger, and F. Bauer, "Pyvisa," (2022).

[88] qpit, "`thorlabs-apt`," .

[89] P. Tapping, "`thorlabs-apt-device`," .

[90] R. P. Abel, A. K. Mohapatra, M. G. Bason, J. D. Pritchard, K. J. Weatherill, U. Raitzsch, and C. S. Adams, "Laser frequency stabilization to excited state transitions using electromagnetically induced transparency in a cascade system," Applied Physics Letters **94** (2009), 10.1063/1.3086305.

[91]   K. J. Astrom and R. M. Murray, *Feedback Systems: An Introduction for Sci-entists and Engineers* (Princeton University Press, USA, 2008).

[92]   G. C. Goodwin, S. F. Graebe, and M. E. Salgado, *Control System Design*, 1st ed. (Prentice Hall PTR, USA, 2000).

[93]   P. W. Milonni and J. H. Eberly, *Laser Physics* (Wiley, 2010).

[94]   A. E. Siegman, *Lasers* (University Science Books, 1986).

[95]   E. D. Black, "An introduction to Pound–Drever–Hall laser frequency sta-bilization," American Journal of Physics **69**, 79 (2001).

[96]   D. Boddy, *First observations of Rydberg blockade in a frozen gas of divalent atoms*, Ph.D. thesis, Durham University (2014).

[97]   C. N. Jackson, *Rydberg spectroscopy and dressing in an ultracold stron-tium gas*, Ph.D. thesis, Durham University (2018).

[98]   S. Pugla, *Ultrastable High Finesse Cavities for Laser Frequency Stabiliza-tion*, Ph.D. thesis, Imperial College London (2007).

[99]   E. M. Lally, *A Narrow-Linewidth Laser at 1550 nm Using the Pound-Drever-Hall Stabilization Technique*, Master's thesis, Virginia Polytech-nic Institute and State University (2006).

[100]   J. C. Livas, J. I. Thorpe, K. Numata, S. Mitryk, G. Mueller, and V. Wand, "Frequency-tunable pre-stabilized lasers for lisa via sideband-locking," Classical and Quantum Gravity **26** (2008).

[101]   C. R. Higgins, D. Pizzey, R. S. Mathew, and I. G. Hughes, "Atomic line versus lens cavity filters: a comparison of their merits," OSA Continuum **3** (2020).

[102] J. Helmcke, S. A. Lee, and J. L. Hall, "Dye laser spectrometer for ultrahigh spectral resolution: design and performance," Appl. Opt. **21**, 1686 (1982).

[103] J. H. T. Burke, O. Garcia, K. J. Hughes, B. Livedalen, and C. A. Sackett, "Compact implementation of a scanning transfer cavity lock," Review of Scientific Instruments **76** (2005), 10.1063/1.2135278, 116105.

[104] W. Z. Zhao, J. E. Simsarian, L. A. Orozco, and G. D. Sprouse, "A computer-based digital feedback control of frequency drift of multiple lasers," Review of Scientific Instruments **69**, 3737 (1998).

[105] N. Seymour-Smith, P. Blythe, M. Keller, and W. Lange, "Fast scanning cavity offset lock for laser frequency drift stabilization," Review of Scientific Instruments **81** (2010), 10.1063/1.3455830.

[106] J. Yiu, *The Definitive Guide to ARM Cortex-M3 and Cortex-M4 Processors, Third Edition*, 3rd ed. (Newnes, USA, 2013).

[107] R. W. Schafer, "What is a savitzky-golay filter? [lecture notes]," IEEE Signal Processing Magazine **28**, 111 (2011).

[108] S. Guan, J. Cheng, and S. Chang, "Recent progress of terahertz spatial light modulators: Materials, principles and applications," Micromachines (Basel) **13** (2022).

[109] Y. Wang, F. Qi, and J. Wang, "Thz super-resolution imaging based on complex fast deconvolution with incomplete boundaries," in *2022 34th Chinese Control and Decision Conference (CCDC)* (2022) pp. 2282–2285.

[110] P. S. Hauge, "Survey Of Methods For The Complete Determination Of A State Of Polarization," in *Polarized Light: Instruments, Devices, Applica-*

tions, Vol. 0088, edited by R. M. A. Azzam and W. L. Hyde, International Society for Optics and Photonics (SPIE, 1976) pp. 3 – 10.

[111] T. Kihara, "Measurement method of stokes parameters using a quarter-wave plate with phase difference errors," Appl. Opt. **50**, 2582 (2011).

[112] D. Steck, "Caesium D Line Data," (2019), available at https://steck.us/alkalidata.

[113] A. Rogalski, *Infrared and Terahertz Detectors: Third Edition* (CRC Press, 2019).

[114] E. Wolf, "Electromagnetic diffraction in optical systems. i. an integral representation of the image field," Proceedings of the Royal Society of London. Series A, Mathematical and Physical Sciences **253**, 349 (1959).

[115] B. Richards and E. Wolf, "Electromagnetic diffraction in optical systems. ii. structure of the image field in an aplanatic system," Proceedings of the Royal Society of London. Series A, Mathematical and Physical Sciences **253**, 358 (1959).

[116] L. Sun, Y. Zhang, H. Chen, C. Zhang, Y. Fu, S. Zhu, Y. Yang, C. Min, and X. Yuan, "Generalized vector diffraction model for tight focusing of light with arbitrary polarization state," Optik **201**, 163528 (2020).

[117] P. H. Jones, O. M. Maragò, and G. Volpe, *Optical Tweezers: Principles and Applications* (Cambridge University Press, 2015).

[118] L. A. Downes, D. J. Whiting, C. S. Adams, and K. J. Weatherill, "Rapid readout of terahertz orbital angular momentum beams using atom-based imaging," Opt. Lett. **47**, 6001 (2022).

Colophon

This thesis is based on a template developed by Matthew Townson and Andrew Reeves. It was typeset with $\LaTeX\,2_\varepsilon$. It was created using the *memoir* package, maintained by Lars Madsen, with the *madsen* chapter style. The font used is Latin Modern, derived from fonts designed by Donald E. Kunith.